Multiple Scattering for Diffraction Enhanced X-ray Imaging

DISSERTATION
zur Erlangung des Grades eines Doktors
der Naturwissenschaften

vorgelegt von
Dipl.-Phys. Gabriele Heike Heitner
geb. am 21.06.1965 in Marburg

Eingereicht beim Fachbereich Physik
der Universität Siegen
Siegen 2005

Gutachter der Dissertation:	Prof. Dr. A.H. Walenta	Universität Siegen (D)
	Prof. R. Longo	Università degli Studi di Trieste (I)
Eingereicht am:	28.02.2005	
Datum der Disputation:	29.04.2005	
Prüfer:	Prof. Dr. A.H. Walenta	Universität Siegen (D)
	Prof. R. Longo	Università degli Studi di Trieste (I)
	Prof. Dr. H. Walliser	Universität Siegen (D)
	Dott. F. Arfelli	Università degli Studi di Trieste (I)

Internetpublikation der Universitätsbibliothek Siegen: urn:nbn:de:hbz:467-1062

Abstract

Materials which multiply scatter X-rays and consisting of weakly absorbing microstructures, such as lung tissue, deliver significant signals and remarkable contrast using the diffraction enhanced imaging (DEI) technique. The DEI technique is investigated with respect to multiple scattering properties and its applicability to soft tissue in order to improve medical diagnostics using phase contrast imaging as a new generation of radiography. Methods and calculation algorithms for extracting multiple scattering information by applying the DEI technique were recently developed considering ultra-small angle X-ray scattering. Algorithms and techniques developed in this work allow (i) extending the DEI technique to small-angle scattering of spherical and cylindrical micro-scattering particles, and (ii) computationally efficient analytical calculation of the scattering power by using the properties of a single scattering microparticle. This method was verified during several experiments at the large-scale facilities ELETTRA and ESRF using (i) synthetic specimens, and (ii) applying the calculations to a cow lung tissue specimen assuming alveolar air. While specimen preparation and deflation of the specimen led to uncertainties, the method was verified in this case by comparing the predicted scattering power of mouse lung tissue with Monte-Carlo simulations of the DEI group of Monash University, Melbourne (AUS).

The influence of specimen substructure on multiple scattering is investigated and can be qualitatively reconstructed using the model of scattering elaborated in this work. Calculated scattering angle distributions predict strong influence of substructures on the scattering power.

The instrumental effects of the analyser crystal, acting as an angular band-pass filter, on the multiple scattering power are analysed and simulated by calculation. Similar cut-offs by the analyser crystal are expected for soft tissue as for the synthetic specimens: The calculated scattering power of the cow lung tissue specimen as well as an exemplary calculation of the scattering power of a human lung for a frontal thorax exposure demonstrate a similar scattering power as the synthetic specimens.

Zusammenfassung

Materialien wie etwa Lungengewebe, die aus schwach absorbierenden, vielfachstreuenden Mikrostrukturen bestehen, zeigen unter Verwendung der „Diffraction Enhanced Imaging“ (DEI) Technik signifikante Signale und bemerkenswerten Bildkontrast. Die DEI Technik wird im Hinblick auf Eigenschaften der Vielfachstreuung und ihre Anwendungsmöglichkeit zur medizinischen Diagnostik als neue Generation phasenkontrastsensitiver Radiografie untersucht. Methoden und Algorithmen zur Bestimmung der Vielfachstreustärke unter Verwendung der DEI Technik sind aktuell nur für besonders kleine Streuwinkel verfügbar. Diese Arbeit zeigt Methoden und Berechnungen (i) zur Erweiterung des Streuwinkelbereiches unter Verwendung von kugel- und zylinderförmigen Streupartikeln, und (ii) die rechentechnisch effektive Bestimmung der Vielfachstreustärke unter Zurückführung auf die Streustärke des einzelnen Partikels. Die vorgestellte Berechnungsmethode wird anhand von Experimenten an den Großforschungseinrichtungen ELETTRA und ESRF unter Benutzung von (i) synthetischen Proben und (ii) der Anwendung der Berechnungen auf eine Probe einer Kuhlunge experimentell verifiziert. Während die Präparation und das Zusammenfallen der Lungenprobe zu Unsicherheiten führt, zeigt die vergleichsweise Berechnung zur Streuwirkung einer Mauslunge, die durch die DEI Gruppe der Monash Universität in Melbourne (AUS) mithilfe der Monte-Carlo Methode simuliert wurde, gute Übereinstimmung.

Der Einfluss von Substrukturen auf die Vielfachstreuwirkung wird untersucht und ist unter Benutzung des in dieser Arbeit vorgestellten Streumodells qualitativ rekonstruierbar. Simulierte Streuwinkelverteilungen prognostizieren einen starken Einfluss von Substrukturen auf die Streustärke.

Der instrumentelle Einfluss des Analysatorkristalls, der als Winkelfilter wirkt, wird im Falle von Vielfachstreuung analysiert und kann rechentechnisch nachgebildet werden. Ähnliche signalverzerrende Eigenschaften, die im Experiment mit den synthetischen Proben beobachtet wurden, werden für Lungengewebe erwartet. Die Probe der Kuhlunge und eine Hochrechnung für die Streustärke der menschlichen Lunge bei einer frontalen Thoraxaufnahme zeigen vergleichbare Streustärken mit den im Experiment verwendeten synthetischen Proben.

Riassunto

Materiali che causano la diffusione multipla di raggi X e che consistono di microstrutture poco assorbenti, come ad esempio il tessuto polmonare, producono segnali significativi e contrasti notevoli utilizzando la tecnica del “Diffraction Enhanced Imaging” (DEI). La tecnica DEI è investigata con particolare riguardo alle proprietà di diffusione multipla ed alle sue applicazioni all’imaging di tessuti molli col fine di migliorare la dignostica medica utilizzando il contrasto di fase come imaging radiografico di nuova generazione. Metodi ed algoritmi di calcolo per estrarre informazioni di diffusione multipla applicando la tecnica DEI sono stati recentemente sviluppati considerando la diffusione di raggi X a piccolissimo angolo. Le tecniche e gli algoritmi sviluppati in questo lavoro di tesi permettono (i) di estendere la tecnica DEI alla diffusione a piccolo angolo da micro particelle sferiche e cilindriche e (ii) di calcolare analiticamente e con un uso efficiente del calcolo numerico la potenza di diffusione utilizzando le proprietà di diffusione da una singola micro-particella. Questo metodo è stato verificato durante diversi esperimenti presso i grandi laboratori internazionali ELETTRA ed ESRF utilizzando (i) campioni sintetici e (ii) applicando i calcoli a campioni di tessuto polmonare di mucca assumendo aria negli alveoli. Poichè la preparazione del campione ed il suo deterioramento hanno portato ad alcune incertezze, il metodo in questo caso è stato verificato confrontando la potenza di scattering prevista nel caso di tessuto polmonare di topo con simulazioni Montecarlo del gruppo DEI dell’Università di Monash, Melbourne (AUS).

L’influenza della sottostruttura del campione sulla diffusione multipla è stata investigata e può essere ricostruita qualitativamente utilizzando il modello di diffusione elaborato in questo lavoro di tesi. Le distribuzioni calcolate per l’angolo di diffusione predicono una forte influenza delle sottostrutture sulla potenza di diffusione.

Si sono analizzati e ricostruiti mediante simulazioni gli effetti strumentali d cristallo analizzatore, che funge da filtro angolare passa-banda, sulla potenza di diffusione multipla. Effetti di taglio simili da parte del cristallo analizzatore sono attesi per i tessuti molli e per i campioni sintetici. La potenza di diffusione calcolata per i campioni di tessuto polmonare di mucca come pure un calcolo dimostrativo della potenza di diffusione di un polmone umano per una esposizione toracica frontale dimostrano una potenza di diffusione simile a quella dei campioni sintetici.

Contents

ACKNOWLEDGEMENT

Introduction

Radiography is established as one of the key techniques in medical diagnostics. Since the discovery of X-rays in 1895 by W. C. Röntgen [Röntgen, 1896] the X-ray absorption of matter is mostly used in radiography. Thus, low or weakly absorbing objects are quasi not detectable. This fact changed with identifying phase sensitive imaging and contrast techniques where additionally to amplitude the phase modulation is considered. Early phase sensitive X-ray imaging techniques took its lead from visible light [Zernike, 1935], [Gabor, 1948] and [Schmahl et al., 1987] were accentuated by the development of third generation synchrotron radiation (SR) light sources and appropriate detectors. The ideas developed in the synchrotron community have been demonstrated to play a major role for high-brilliance laboratory sources, which permits phase sensitive imaging techniques to be a field of growing scientific activity ever since.

Recent investigations on phase contrast methods deliver prospects to revolutionise radiography. Phase contrast methods offer mainly two benefits with special importance for medical applications: (i) the Dose for imaging can be reduced tremendously, because the contrast is essentially determined by elastic photon scattering. (ii) Structures with low absorption properties are detectable due to their phase modulation properties, which are dominant for multi-keV and hard X-rays used for medical applications. Phase modulation scales with the photon energy E, approximately with E^{-1} far away from the absorption edges compared to E^{-3} for absorption contrast [Als-Nielsen et al., 2001].

Phase contrast imaging is an improved technique to determine objects with weakly absorbing properties using SR in biomedical imaging [Davis et al., 1995], [Ingal et al., 1995]. All these techniques used for phase contrast imaging, frequently specified with different synonyms, are based on principles sensitive to (i) phase shift as interferometry, (ii) phase gradient due to refraction as diffraction enhanced imaging (DEI), and (iii) Fresnel diffraction depending on the second derivation of the materials density distribution as in-line holography or phase propagation imaging (PPI) [Baruchel et al., 2000].

The special appeal of the DEI technique, as presented and applied in this work, governs from large object fields and mesoscopic resolution, suiting the necessary conditions for medical applications. The DEI technique seems to offer an excellent technique for medical applications [Arfelli et al., 1998], [Pisano et al., 2000], [Mollenhauer et al., 2002], [Muehleman et al., 2004].

Photons passing the specimen are deflected by the so-called refraction angle $\Delta\theta$ determined by the phase gradient of the specimen. An analyser crystal behind the specimen acts as angular filter. The DEI technique was proposed by Förster [Förster et al., 1980] calling it "Schlieren method". Using SR, the technique was developed under different names. Sometimes it is also called in general "Refraction imaging" [Baruchel et al., 2000] or "Analyser based techniques". Chapman extended the technique to an algorithm which allows extracting absorption and refraction information for weak objects with absent additional scattering, and called it "diffraction enhanced X-ray imaging" [Chapman et al., 1997].

Multiple scattering materials such as soft lung tissue deliver significant signals and remarkable contrast using the DEI technique [Arfelli et al., 2002], [Lewis et al., 2002]. The investigation of multiple scattering properties and their applicability to lung tissue is presented in this work in order to improve techniques for lung studies and diagnostics. Groups of scientists examine worldwide lung imaging and properties of multiple scattering [Bravin, 2004], [Wilkins, 2004], [Suortti, 2004]. Recent approaches of extracting multiple scattering information are described by Paganin [Paganin et al., 2004], Nesterets [Nesterets et al., 2004], Oltuli [Oltulu et al., 2003], Wernick [Wernick et al., 2003], Pagot [Pagot et al., 2003] and Rigon [Rigon et al., 2003]. All these approaches describe scattering assuming ultra small angle scattering or low influences of scattering, respectively.

This work is strongly related to earlier experimental and theoretical work [Arfelli et al., 2002], [Rigon et al., 2003], and aims at exploring the ability to handle not necessarily ultra small angle scattering. An approach to *modelling multiple scattering due to refraction* is identified, which is evaluated and proven on mesoscopic and microscopic scales during several experiments at the large-scale facilities ELETTRA and ESRF [ELETTRA], [ESRF].

The appeal and originality of the method presented here is that it directly retrieves the multiple scattering information with computationally efficient algorithms, and uses standard DEI techniques and instrumentation already available at two medical beam lines of major European large-scale facilities.

The calculation of multiple scattering power is applicable to weakly absorbing specimens with randomly distributed micro scattering particles, whereas periodical substructures lead to a strong influence on multiple scattering power.

In most cases, multiple scattering effects angular intensity distributions of the scattered X-rays far away the range of ultra small angle scattering with respect to the analyser crystal properties. Thus, the analyser crystal influence on multiple scattering signals is demonstrated.

These considerations are necessary for successfully study of soft tissue for medical applications and diagnostics.

Chapter 1 introduces some fundamental properties and a description of the DEI technique helpful for the understanding of this work.

Chapter 2 focuses on the *model for multiple scattering due to refraction* and the calculation modalities of the multiple scattering power. The angular distribution of scattering angles for a single scattering event is identified for two simple particle geometries resembling higher-organised biomedical structures. The *single scattering power* is determined by using the scattering angle distribution. This leads to the calculation of the *multiple scattering power* of randomly distributed micro-scattering particles, which is verified by Monte-Carlo simulations. The calculations are applied to soft tissue and the multiple scattering powers for lung tissues and alveoli is predicted.

Chapter 3 continues with introducing typical experimental set-ups for DEI experiments at the two large-scale facilities ELETTRA and ESRF, before describing specimens (synthetic specimen with well-defined structure and substructure as well as lung tissues) and the experiments itself in chapter 4.

Chapter 5 concentrates on the analysis of multiple scattering experiments described in chapter 4. (i) The calculation of multiple scattering power by using the scattering power of the single particle is quantitatively verified by experiment and applied to soft tissue. (ii) The instrumental influence of the analyser crystal to the image formation in case of multiple scattering is described. (iii) The impact of sub-structures in multiple scattering specimens is qualitatively verified.

Ambition of this work is (i) to identify properties of multiple scattering described by an analytical formula, which allows computationally efficient, direct calculation of the scattering power, (ii) to identify and prove the feasibility to apply the DEI technique to soft tissue as a new generation radiography method.

References

[Als-Nielsen et al., 2001] Als-Nielsen, J. and D. MacMorrow (2001). *Elements of modern X-ray physics*. Ed John Wiley & Sons Ltd., West Sussex, England.

[Arfelli et al., 1998] Arfelli, F., M. Assante, V. Bonvicini, A. Bravin, G. Cantatore, E. Castelli, L. Dalla Palma, M. Di Michiel, R. Longo, A. Olivo, S. Pani, D. Pontoni, P. Poropat, M. Prest, A. Rashevsky, G. Tromba, A. Vacchi, E. Vallazza and F. Zanconati (1998). *Low-dose phase contrast x-ray medical imaging*. Physics in Medicine and Biology **43**(10): 2845-2852.

[Arfelli et al., 2002] Arfelli, F., R. H. Menk, H. J. Besch, L. Rigon and H. Plothow-Besch (2002). *Contrast Improvement with Diffraction Enhanced Imaging for scattering materials.* Proc. 2002 IEEE Int. Symp. Biomedical Imaging. p. 133.

[Baruchel et al., 2000] Baruchel, J., P. Cloetens, J. Hartwig, W. Ludwig, L. Mancini, P. Pernot and M. Schlenker (2000). *Phase imaging using highly coherent X-rays: radiography, tomography, diffraction topography.* Journal of Synchrotron Radiation **7**: 196-201.

[Bravin, 2004] Bravin, A. (2004). *Phase contrast imaging in medicine and biology at the ESRF.* MASR, Trieste.

[Chapman et al., 1997] Chapman, D., W. Thomlinson, R. E. Johnston, D. Washburn, E. Pisano, N. Gmur, Z. Zhong, R. Menk, F. Arfelli and D. Sayers (1997). *Diffraction enhanced x-ray imaging.* Physics in Medicine and Biology **42**(11): 2015-2025.

[Davis et al., 1995] Davis, T. J., D. Gao, T. E. Gureyev, A. W. Stevenson and S. W. Wilkins (1995). *Phase-Contrast Imaging of Weakly Absorbing Materials Using Hard X-Rays.* Nature **373**(6515): 595-598.

[ELETTRA] ELETTRA http://www.elettra.trieste.it (Electronic source).

[ESRF] ESRF http://www.esrf.fr (Electronic source).

[Förster et al., 1980] Förster, E., K. Goetz and P. Zaumseil (1980). *Double Crystal Diffractometry for the Characterization of Targets for Laser Fusion Experiments.* Kristall und Technik **15**(8): 937-945.

[Gabor, 1948] Gabor, D. (1948). Nature(161): 777.

[Ingal et al., 1995] Ingal, V. N. and E. A. Beliaevskaya (1995). *X-Ray Plane-Wave Topography Observation of the Phase-Contrast from a Noncrystalline Object.* Journal of Physics D-Applied Physics **28**(11): 2314-2317.

[Lewis et al., 2002] Lewis, R. A., K. D. Rogers, C. J. Hall, A. P. Hufton, S. Evans, R. Menk, G. Tromba, F. Arfelli, L. Rigon, A. Olivo, A. Evans, S. E. Pinder, E. Jacobs, I. O. Ellis and D. R. Dance (2002). *Diffraction enhanced imaging: improved contrast, lower dose X-ray imaging.* Proceedings of SPIE 4682. 286-297.

[Mollenhauer et al., 2002] Mollenhauer, J., M. E. Aurich, Z. Zhong, C. Muehleman, C. C. Cole, M. Hasnah, O. Oltulu, K. E. Kuettner, A. Margulis and L. D. Chapman (2002). *Diffraction-enhanced X-ray imaging of articular cartilage.* Osteoarthritis and Cartilage **10**(3): 163-171.

[Muehleman et al., 2004] Muehleman, C., S. Majumdar, A. S. Issever, F. Arfelli, R. H. Menk, L. Rigon, G. Heitner, B. Reime, J. Metge, A. Wagner, K. E. Kuettner and J. Mollenhauer (2004). *X-ray detection of structural orientation in human articular cartilage.* Osteoarthritis and Cartilage **12**(2): 97-105.

[Nesterets et al., 2004] Nesterets, Y. I., T. E. Gureyev, D. Paganin, K. M. Pavlov and S. W. Wilkins (2004). *Quantitative diffraction-enhanced x-ray imaging of weak objects.* Journal of Physics D-Applied Physics **37**(8): 1262-1274.

[Oltulu et al., 2003] Oltulu, O., Z. Zhong, M. Hasnah, M. N. Wernick and D. Chapman (2003). *Extraction of extinction, refraction and absorption properties in diffraction enhanced imaging.* Journal of Physics D-Applied Physics **36**(17): 2152-2156.

[Paganin et al., 2004] Paganin, D., T. E. Gureyev, K. M. Pavlov, R. A. Lewis and M. Kitchen (2004). *Phase retrieval using coherent imaging systems with linear transfer functions.* Optics Communications **234**(1-6): 87-105.

[Pagot et al., 2003] Pagot, E., P. Cloetens, S. Fiedler, A. Bravin, P. Coan, J. Baruchel, J. Hartwig and W. Thomlinson (2003). *A method to extract quantitative information in analyzer-based x-ray phase contrast imaging.* Applied Physics Letters **82**(20): 3421-3423.

[Pisano et al., 2000] Pisano, E. D., R. E. Johnston, D. Chapman, J. Geradts, M. V. Iacocca, C. A. Livasy, D. B. Washburn, D. E. Sayers, Z. Zhong, M. Z. Kiss and W. C. Thomlinson (2000). *Human breast cancer specimens: Diffraction-enhance imaging with histologic correlation - Improved conspicuity of lesion detail compared with digital radiography.* Radiology **214**(3): 895-901.

[Rigon et al., 2003] Rigon, L., H. J. Besch, F. Arfelli, R. H. Menk, G. Heitner and H. Plothow-Besch (2003). *A new DEI algorithm capable of investigating sub-pixel structures.* Journal of Physics D-Applied Physics **36**(10A): A107-A112.

[Röntgen, 1896] Röntgen, W. C. (1896). *On a new kind of rays.* Nature(53): 274-276.

[Schmahl et al., 1987] Schmahl, G. and D. Rudolph (1987). *Proposal for a Phase Contrast X-ray microscope. X-ray microscopy: Instrumentation and Biological Applications.* P. C. Cheng and G. J. Jan, Springer-Verlag, Berlin: 231-238.

[Suortti, 2004] Suortti, P. (2004). *Lung structure and function studied by the KES method with stable Xenon gas as the contrast agent.* MASR, Trieste.

[Wernick et al., 2003] Wernick, M. N., O. Wirjadi, D. Chapman, Z. Zhong, N. P. Galatsanos, Y. Y. Yang, J. G. Brankov, O. Oltulu, M. A. Anastasio and C. Muehleman (2003). *Multiple-image radiography.* Physics in Medicine and Biology **48**(23): 3875-3895.

[Wilkins, 2004] Wilkins, S. W. (2004). *Emerging Opportunities for Biomedical Phase-Contrast Imaging using SR.* MASR, Trieste.

[Zernike, 1935] Zernike, F. (1935). Z. Tech. Phys.(16): 454.

1 Fundamentals of diffraction enhanced imaging

Depending on the refractive index, two types of X-ray imaging can be distinguished: (i) In absorption or bright-field imaging, the contrast arises from differences of the absorption coefficient. Hence the absorption contrast is sensitive to thickness differences and composition of the specimen. This technique has played up to now the major role in clinical imaging. Absorption contrast techniques suffer when the specimen consists of low Z-elements, or for high photon energies. (ii) X-rays traversing the specimen experience differences in the optical thickness of the specimen due to the real part of refractive index. Similar to a prism for visible light, the specimen creates a phase gradient and the X-rays are deviated or refracted. Imaging techniques based on this modality are called phase-sensitive imaging or phase contrast techniques. Several different techniques have been explored, which can be classified in (i) the interferometric technique, (ii) the analyser-based technique and (iii) the propagation technique [Authier, 2001], [Baruchel et al., 2000]. This work focuses on the analyser-based technique: the diffraction enhanced imaging (DEI) technique.

Section 1.1 introduces basic properties helpful for the understanding of the following chapters. Section 1.2 introduces the basics of the diffraction enhanced imaging technique. Section 1.3 gives a brief introduction to the state-of-the-art of multiple scattering and current DEI algorithms.

1.1 Absorption versus phase contrast

The behaviour of X-rays as they traverse matter is typically described by the refractive index $n = 1 - \delta + i\beta$, where the real part δ is the phase shift portion and the imaginary part β the absorption portion.

With an average density of atoms n_a, the electron radius r_e and the wavelength λ, δ and β can be expressed with the wave propagation theory as [Attwood, 1999]:

$$\delta = \frac{n_a r_e \lambda^2}{2\pi} f_1^0(\lambda)$$

$$\beta = \frac{n_a r_e \lambda^2}{2\pi} f_2^0(\lambda)$$

Equations 1-1

With the complex atomic scattering or form factor $f^0 = f_1^0(\lambda) + i f_2^0(\lambda)$. The real and imaginary parts are experimentally and/or computationally determined and are for example tabulated by [Henke, Gullikson and Davis, 1993] for photon energies extending from 10 eV to 30 keV. Numerically, *n* is only slightly smaller than unity and δ ranges from 10^{-7} to 10^{-6} whereas β ranges from 10^{-12} to 10^{-9}.

In the photo-electric regime and far away from absorption edges, the macroscopic-to-atomic relation of these properties can be expressed with the absorption coefficient μ and the relative phase shift $\Delta\Phi$ [LBL, 2002]:

$$\mu = \frac{2 r_e \lambda}{m_a} f_2^0(\lambda)$$

$$\Delta\Phi = \frac{2\pi\delta}{\lambda} \Delta r$$

Equations 1-2,

where m_a is the atomic mass and Δr the thickness or propagation distance.

Considering that $f_2^0(\lambda)$ typically scales with the photon energy E^{-3} to E^{-4} [Als-Nielsen et al., 2001], the energy dependence of δ and β can be approximated for energies far away from absorption edges and in the photoelectric regime as (see Equations 1-1):

$$\delta \propto \frac{1}{E^2}$$

$$\beta \propto \frac{1}{E^4}$$

Equations 1-3

Hence, the energy dependence of the relative phase shift $\Delta\Phi$ and the absorption coefficient μ can be expressed with Equations 1-2 as:

$$\Delta\Phi \propto \frac{1}{E}$$

$$\mu \propto \frac{1}{E^3}$$

Equations 1-4

Equations 1-4 show that phase terms become advantageous for high photon energies and crucial for high photon energies and hard X-rays typically used for medical imaging due to the higher penetration depth and lower dose applied.

1.2 Diffraction enhanced imaging (DEI)

The diffraction enhanced imaging technique (DEI) is an analyser-based technique pioneered by Förster et al. [Förster et al., 1980] in the 1980's. Applying the technique to SR, the method is currently known under different names, for instance "analyser based technique". The name "diffraction enhanced imaging" used in this work was introduced in relation to an image-processing algorithm permitting the separation of the phase-sensitive or refraction contrast from the absorption contrast of the specimen [Chapman et al., 1997].

In this technique, X-rays traversing the specimen are analysed by a crystal (the so-called analyser crystal). The specimen is placed between the monochromator or "collimator" crystal(s) and the analyser crystal. The angular acceptance of the optical system is determined by the convolution of the reflectivity curves or "rocking curves" of monochromator and analyser.

X-rays refracted from the specimen are deflected from their original direction by an amount depending on phase shift Φ of an electromagnetic wave passing through a specimen with electron density ρ_e, the X-rays trace in the z direction is denoted:

$$\Phi = -r_e \lambda \int \rho_e(x,y,z)dz$$

Equation 1-5

where r_e is the classical electron radius and λ the wavelength. The angular deviation $\Delta\Theta$ is proportional to [Born et al., 1999]:

$$\Delta\Theta(x,y) \approx -\frac{\lambda}{2\pi}\nabla_{x,y}\Phi(x,y,z) \qquad \textbf{Equation 1-6}$$

The analyser crystal diffracts deviated X-rays with an intensity modulated by the reflectivity properties of the crystal, characterised by the "rocking curve" (RC) of the analyser crystal. Because of its angular filter properties, the analyser crystal is the key optical element for the DEI technique. The decisive factor determining image sensitivity and contrast is the position $\Delta\Theta$ on the analyser's rocking curve, and tunes the analyser system relative to the monochromator crystal system (see Figure 1-1): The analyser diffracts the not refracted X-rays with full intensity when the analyser angle corresponds to the maximum of the rocking curve (position 3). The situation changes when the analyser is set to position 1 on the slope of the rocking curve. Small variations in the direction of X-rays due to phase gradients from the specimen might coincide with incidence angles on the analyser corresponding to position 1 or 3. This results in a variation of diffraction intensity due to different analyser reflectivities that can be recorded by the detection system. Thus, phase or "refraction" contrast is obtained. Further detuning the analyser far off the Bragg angle, inverse contrast can be observed because unrefracted X-rays are rejected and only scattered X-rays contribute to the image formation [Zhong et al., 2000].

The DEI technique is also capable of displaying a contrast type termed "extinction contrast" where scattered X-rays are efficiently removed from the images due to the narrow rocking curve width of the analyser [Hasnah et al., 2002]. A typical angular bandwidth of the analyser's RC is in the range of 1 to 20 μrad (FWHM).

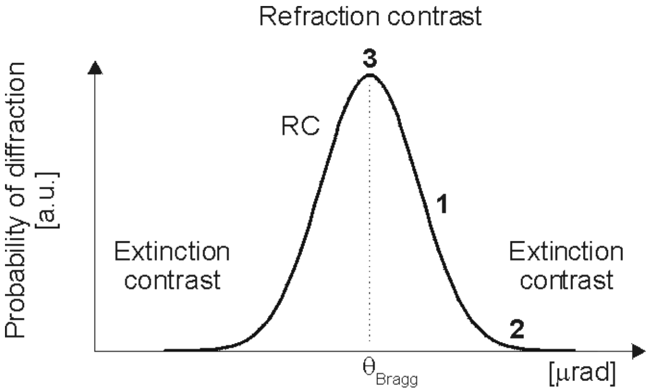

Figure 1-1 Origin of DEI phase contrast:

(i) Refraction contrast and (ii) Extinction contrast

The sensitivity of the method is restricted to deflections resulting from planes parallel to the diffraction plane of the analyser crystal. Deflections resulting from planes perpendicular the analyser's diffraction plane are not resolved by DEI phase contrast, because the analyser is not sensitive to this direction. If the analyser is installed in the *y* direction, Equation 1-6 simplifies to:

$$\Delta\Theta(x) \approx -\frac{\lambda}{2\pi}\frac{\partial}{\partial x}\Phi(x,y,z) \qquad \textbf{Equation 1-7}$$

For a more detailed state-of-the-art description of the DEI technique, see [Bravin, 2003] and [Lewis et al., 2002]. A comprehensive introduction to diffraction properties of crystals is given by [Authier, 2001].

Whereas this method is highly sensitive to small variations of the refractive index, it is less adapted than other techniques like interferometry to the low frequency range because smooth changes in optical density may introduce phase gradients too small to be detected. Nevertheless, multiple scattering enhances the effect. Thus the DEI technique seems interesting for multiple scattering studies or to determine the limitations of the DEI technique.

In his considerations about medical application of phase contrast methods and future prospects, [Lewis, 2004] describes the lung as an ideal candidate for phase contrast imaging and states that it seems that phase contrast methods may offer enhanced chest radiographs. Up to now, the investigations are in a very early stage.

The present work may motivate scattering studies in general using the DEI technique and to prove their applicability to lung studies and diagnostics.

1.3 Multiple scattering: State-of-the-art

The width of the RC is increased from the intrinsic value if scattering is present.

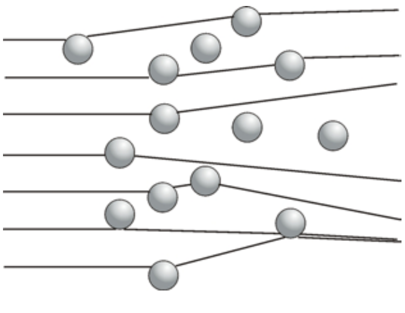

Figure 1-2 Scattering enlarges the intrinsic value of the RC

The Chapman algorithm [Chapman et al., 1997] including absorption and refraction, allows extraction of an absorption image and a refraction image from two DEI images acquired on both sides of the RC. But the Chapman algorithm does not include scattering information. The approach of Rigon [Rigon et al., 2003] considers a second order Taylor expansion of the Chapman algorithm including absorption information and ultra small angle scattering. The scattering information can directly be extracted from a post-calculated image using his algorithm. Pagot's approach [Pagot et al., 2003] combines refraction, absorption and ultra small angle scattering. By processing three to 28 images acquired at different analyser crystal positions are calculated a "maximum absorption", an "integrated absorption", a "refraction" and "ultra small angle scattering image". A similar approach is introduced by [Wernick et al., 2003] with the "Multiple Image Radiography". A further conceptually approach is presented by [Oltulu et al., 2003]. 24 images acquired at different positions of the RC deliver a "refraction", an "absorption", an "extinction" and a "scatter width image". [Paganin et al., 2004] introduce a retrieval algorithm, which allows quantitative phase-amplitude reconstruction using four acquired DEI images. Another retrieval algorithm is presented by [Nesterets et al., 2004], which reconstructs quantitatively phase and amplitude using a weak object approximation.

Regarding the current algorithm approaches using the DEI technique it tends from ultra small angle scattering considerations to scattering consideration in general. Significant are also retrieval approaches.

References

[Als-Nielsen et al., 2001] Als-Nielsen, J. and D. MacMorrow (2001). *Elements of modern X-ray physics.* Ed John Wiley & Sons Ltd., West Sussex, England.

[Attwood, 1999] Attwood, D. T. (1999). *Soft X-Rays And Extreme Ultraviolet Radiation.* Cambridge University Press.

[Authier, 2001] Authier, A. (2001). *Dynamical theory of x-ray diffraction.* Oxford University Press.

[Baruchel et al., 2000] Baruchel, J., P. Cloetens, J. Hartwig, W. Ludwig, L. Mancini, P. Pernot and M. Schlenker (2000). *Phase imaging using highly coherent X-rays: radiography, tomography, diffraction topography.* Journal of Synchrotron Radiation **7**: 196-201.

[Born et al., 1999] Born, M. and E. Wolf (1999). *Principles of optics: Electrodynamic theory of propagation, interference and diffraction of light.* Cambridge University Press.

[Bravin, 2003] Bravin, A. (2003). *Exploiting the x-ray refraction contrast with an analyser: the state of the art.* Journal of Physics D-Applied Physics **36**(10A): A24-A29.

[Chapman et al., 1997] Chapman, D., W. Thomlinson, R. E. Johnston, D. Washburn, E. Pisano, N. Gmur, Z. Zhong, R. Menk, F. Arfelli and D. Sayers (1997). *Diffraction enhanced x-ray imaging.* Physics in Medicine and Biology **42**(11): 2015-2025.

[Förster et al., 1980] Förster, E., K. Goetz and P. Zaumseil (1980). *Double Crystal Diffractometry for the Characterization of Targets for Laser Fusion Experiments.* Kristall und Technik **15**(8): 937-945.

[Hasnah et al., 2002] Hasnah, M., O. Oltulu, Z. Zhong and D. Chapman (2002). *Application of absorption and refraction matching techniques for diffraction enhanced imaging.* Review of Scientific Instruments **73**(3): 1657-1659.

[Henke, Gullikson and Davis, 1993] Henke, B. L., E. M. Gullikson and J. C. Davis (1993). *X-Rays Interactions: Photoabsorption, Scattering, Transmission and Reflection at E=50-30.000 eV, Z=1-92.* Atomic and Nuclear Data Tables **54**: 181-342.

[LBL, 2002] LBL (2002). *LBL X-Ray Booklet.* http://xdb.lbl.gov/Section2/Sec_2-1.html (Electronic source).

[Lewis, 2004] Lewis, R. A. (2004). *Medical phase contrast x-ray imaging: current status and future prospects.* Physics in Medicine and Biology **49**(16): 3573-3583.

[Lewis et al., 2002] Lewis, R. A., K. D. Rogers, C. J. Hall, A. P. Hufton, S. Evans, R. Menk, G. Tromba, F. Arfelli, L. Rigon, A. Olivo, A. Evans, S. E. Pinder, E. Jacobs, I. O. Ellis and D.

R. Dance (2002). *Diffraction enhanced imaging: improved contrast, lower dose X-ray imaging.* Proceedings of SPIE 4682. 286-297.

[Nesterets et al., 2004] Nesterets, Y. I., T. E. Gureyev, D. Paganin, K. M. Pavlov and S. W. Wilkins (2004). *Quantitative diffraction-enhanced x-ray imaging of weak objects.* Journal of Physics D-Applied Physics **37**(8): 1262-1274.

[Oltulu et al., 2003] Oltulu, O., Z. Zhong, M. Hasnah, M. N. Wernick and D. Chapman (2003). *Extraction of extinction, refraction and absorption properties in diffraction enhanced imaging.* Journal of Physics D-Applied Physics **36**(17): 2152-2156.

[Paganin et al., 2004] Paganin, D., T. E. Gureyev, K. M. Pavlov, R. A. Lewis and M. Kitchen (2004). *Phase retrieval using coherent imaging systems with linear transfer functions.* Optics Communications **234**(1-6): 87-105.

[Pagot et al., 2003] Pagot, E., P. Cloetens, S. Fiedler, A. Bravin, P. Coan, J. Baruchel, J. Hartwig and W. Thomlinson (2003). *A method to extract quantitative information in analyzer-based x-ray phase contrast imaging.* Applied Physics Letters **82**(20): 3421-3423.

[Rigon et al., 2003] Rigon, L., H. J. Besch, F. Arfelli, R. H. Menk, G. Heitner and H. Plothow-Besch (2003). *A new DEI algorithm capable of investigating sub-pixel structures.* Journal of Physics D-Applied Physics **36**(10A): A107-A112.

[Wernick et al., 2003] Wernick, M. N., O. Wirjadi, D. Chapman, Z. Zhong, N. P. Galatsanos, Y. Y. Yang, J. G. Brankov, O. Oltulu, M. A. Anastasio and C. Muehleman (2003). *Multiple-image radiography.* Physics in Medicine and Biology **48**(23): 3875-3895.

[Zhong et al., 2000] Zhong, Z., W. Thomlinson, D. Chapman and D. Sayers (2000). *Implementation of diffraction-enhanced imaging experiments: at the NSLS and APS.* Nuclear Instruments & Methods in Physics Research Section a-Accelerators Spectrometers Detectors and Associated Equipment **450**(2-3): 556-567.

2 Model for multiple scattering and calculation of multiple scattering power

To overcome two problems that up to now (i) no DEI algorithm is available to treat strong multiple scattering, and (ii) the multiple scattering power of lung tissue may be so strong that it might limit the use of the DEI technique, a novel approach is made to quantify and treat the scattering power independently of extracting scattering information from DEI images. This work considers multiple scattering due to refraction on microscopic and mesoscopic scales covering the scale of lung tissue, assuming two particles geometries: (i) spherical and (ii) cylindrical micro scattering particles. These two particle geometries provide excellent modelling for biological tissue and are frequently used for modelling in medical applications. The sphere is frequently used as a representative geometry for the alveolus in lung tissue [Hills, 1999], [Kreck et al., 2001], whereas the cylinder geometry was successfully used by [Fernandez et al., 2002] to simulate collagen fibrils. Section 2.1 introduces the *model of scattering due to refraction* adapted to the DEI technique. Section 2.2 applies the model of scattering due to refraction to the single scattering cylindrical and spherical particle. Statistical considerations lead to a *function* identifying the scattering angle distributions $\Delta\theta$ for the two particle geometries. The single scattering power $\sigma_{\mathrm{Particle}}$ for the cylindrical as well as the spherical microparticle is derived from the scattering angle distributions $\Delta\theta$. A Monte-Carlo ray tracing is introduced in section 2.3. Thus, an instrument is available for extending single scattering considerations to multiple scattering studies. Section 2.4 presents principles of multiple scattering. Monte-Carlo multi-scattering simulations performed on the *model of scattering due to refraction* lead to the calculation of the multiple scattering power by using the Central Limit Theorem and the scattering power $\sigma_{\mathrm{Particle}}$ of the single microparticle. Good agreement for randomly distributed and weakly absorbing single microparticles is demonstrated. Section 2.5 presents the application of the *model of multiple scattering due to refraction* to lung tissue, which leads to predictions for the scattering power of lung tissue and alveoli. Limits of the *model of multiple scattering due to refraction* and assumptions made for the elaboration of the model in section 2.1 and 2.4 are discussed in section 2.6.

2.1 Model of multiple scattering due to refraction

The DEI technique is sensitive in only one direction of the phase gradient depending on the analyser's diffraction plane (see Equation 1-7). This property of the DEI technique simplifies the task to a quasi two-dimensional problem. Further simplification considers (i) the refraction process for a single scattering microparticle considering (ii) a single refraction process for the particle. The last approach leads to the conclusion that the scattering is independent of the microparticle shape assuming a particle of constant refractive index *n*. These considerations simplify the task to the calculation of the kernel problem: the refraction at a trapezium. Further assumptions identify the *model of multiple scattering due to refraction*. The *model of scattering due to refraction* is applied to a single spherical and cylindrical micro-scattering particle, and is followed by the generalisation to the three-dimensional case.

Modelling of refraction on mesoscopic and microscopic scales

Multiple scattering means multiple interactions of X-rays with the specimen. Figure 2-1 illustrates such a multiple scattering process. Each X-ray traversing the specimen interacts with several microparticles along its path. One interaction is assumed per particle. Each interaction causes a deflection of the X-ray by a single scattering event. The total effect is that the X-ray is deflected by the scattering angle Δθ with respect to its incident direction.

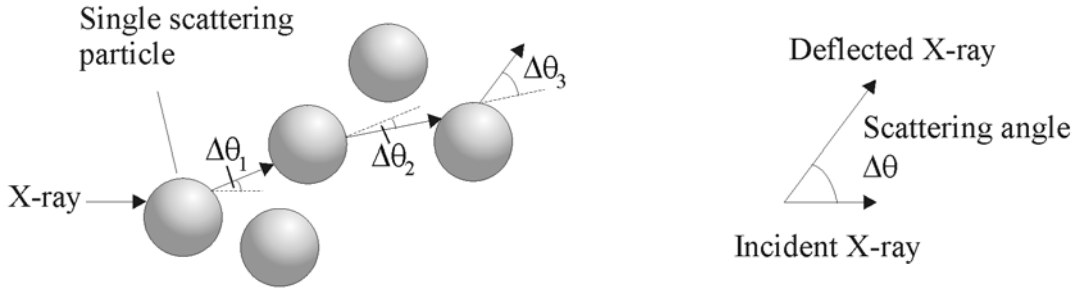

Figure 2-1 Schematic design of a multiple scattering interaction: The X-ray interacts with several microparticles on its path through the material. In each interaction, it is deflected by a scattering angle $\Delta\theta_i$. Afterwards it is deflected by Δθ with respect to its origin direction.

Each single scattering process is described due to refraction. In order to simplify the task, the interface geometry of refractive processes at a circle is considered as follows: According to Snell's law, the X-ray is deflected at the interaction points P_1 and P_2 [Hecht, 2001] and reflection at the interface is neglected. Along the line p between P_1 and P_2 absorption is relevant. After the interactions the X-ray amplitude is reduced and it is deflected by the so-called "scattering angle" $\Delta\theta$. Figure 2-2 illustrates the interface geometry for a single interaction.

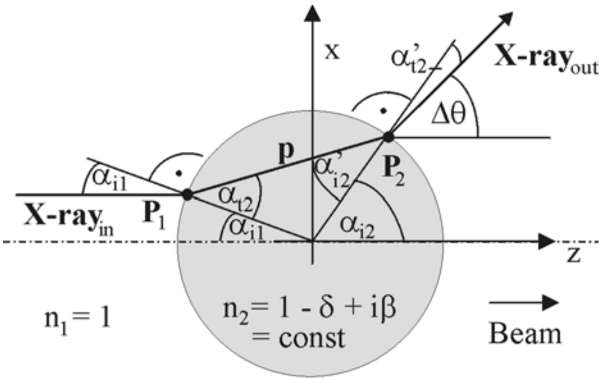

Figure 2-2 Interface geometry for a scattering event at a circle, incident and refraction angles at the interaction points. The incident X-ray hits the circle at point P_1, where it is deflected determined by an angle determined by δ and the incident angle α_{i1}. By Snell's law it passes the circle with α_{t2} with respect to the surface unit vector at the interaction point P_1 and its amplitude is reduced, due to β. Arriving at the surfaces interaction point P_2, the X-ray is deflected again by the angle α_{t2}, due to δ.
The total deflection of the X-ray is by the so-called scattering angle $\Delta\theta$ with respect to its incoming direction.

For a particle of homogeneous material with constant refractive index n_2, the X-ray interaction with the particle can be described by a rotation R at the interfaces (interaction points P_1 and P_2) and a transmission T trough the material as demonstrated in Equation 2-1. The rotations at the interaction points P_1 and P_2 are described by the real part of the refractive index δ, while the transmission is given by the absorption, the imaginary part of refractive index β.

$$I = R_{P2}(\delta) \cdot T(\beta) \cdot R_{P1}(\delta)$$ **Equation 2-1**

In the following considerations, absorption is neglected with $T(\beta) = 1$. The influence of absorption is discussed in sub-section 2.6.1.

For a single scattering event, the whole shape of the scattering particle can be simplified by circle gradients to points P_1 and P_2. Thus, the same scattering effects can be observed by trapezium-type particles with identical gradients as illustrated in Figure 2-3.

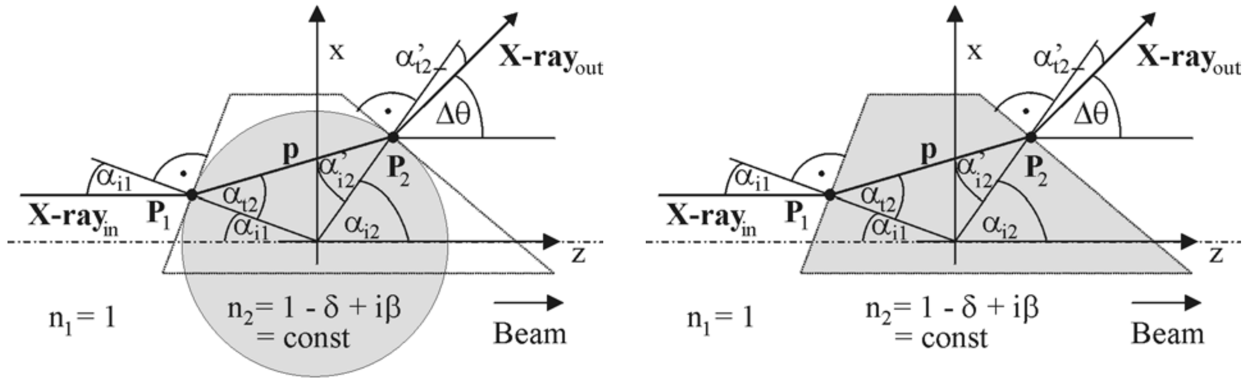

Figure 2-3 Interface geometry for a single scattering event, the circle is substituted by a trapezium representing the same refraction properties.

Left: Interface geometry of a trapezium with the same refraction properties as a circle for a single scattering event.

Right: For a single scattering event the circle is substituted by a trapezium with the same scattering properties.

The scattering angle Δθ is determined by integrating the X-ray trace *p* through the sample over electron density changes perpendicular to its trace as presented by Equation 2-2 (see also Equation 1-6), where *n* is the refractive index of the sample [Born et al., 1999].

$$\Delta\theta = \int_{P1}^{P2} \frac{\partial n}{\partial p_{\perp}} dp$$ **Equation 2-2**

A single scattering event at the trapezium (Figure 2-3 (right)) is considered with the assumption of a homogeneous medium within the circle of constant refractive index n_2. The scattering angle Δθ is given by Equation 2-3, where α_{i1} and α_{i2} are the incident angles at the interface and δ is given by the real part of the refractive index n_2.

$$\Delta\theta = \int_{P1}^{P2} \frac{\partial(1-\delta)}{\partial x} dz$$

$$\Delta\theta = -\delta \frac{\partial z(x)}{\partial x} \Big|_{P1}^{P2}$$

With $z = \sqrt{r^2 - x^2}$ and r as the circle radius as follows:

$$\Delta\theta = -\delta \frac{r \sin(\alpha)}{\sqrt{r^2 - r^2 \sin(\alpha)}} \Big|_{P1}^{P2}$$

$$\Delta\theta = -\delta \tan(\alpha) \Big|_{P1}^{P2}$$

$$\Delta\theta_i = \delta \tan(\alpha_{i1}) - \delta \tan(\pi - \alpha_{i2})$$

$$\Delta\theta_i = \delta \tan(\alpha_{i1}) + \delta \tan(\alpha_{i2}) \qquad \textbf{Equation 2-3}$$

The second incident angle α_{i2} is approximately equal to α_{i1} because of geometrical symmetry and the low δ of the real part of the refractive index *n*. The difference is less than 1% for more than 99% of scattering events for the materials and photon energies considered in this work. This demonstrates calculations presented in sub-section 2.6.2. Thus the scattering angle $\Delta\theta_i$ from Equation 2-3 simplifies to:

$$\Delta\theta_i \approx 2 \cdot \delta \tan(\alpha_i) \qquad \textbf{Equation 2-4}$$

Extension of the two-dimensional to the three-dimensional case requires determining geodetic lines for each incident angle α_{ij} in Equation 2-4. Considering first the sphere using spherical coordinates, the azimuthal angle is constant and the incident angle α_{ij} is the same resulting in circles as illustrated in Figure 2-4 (left).

Considering a cylindrical scattering particle in cylindrical coordinates, the constant azimuthal angle coincides with the incident angles $\alpha_{ij.}$ Also here for every constant azimuthal angle the same incident angle α_{ij} can be shown to occur. As illustrated in Figure 2-4 (right) each incident angle α_{ij} is correlated with a scattering angle $\Delta\theta_i$ (see Equation 2-4).

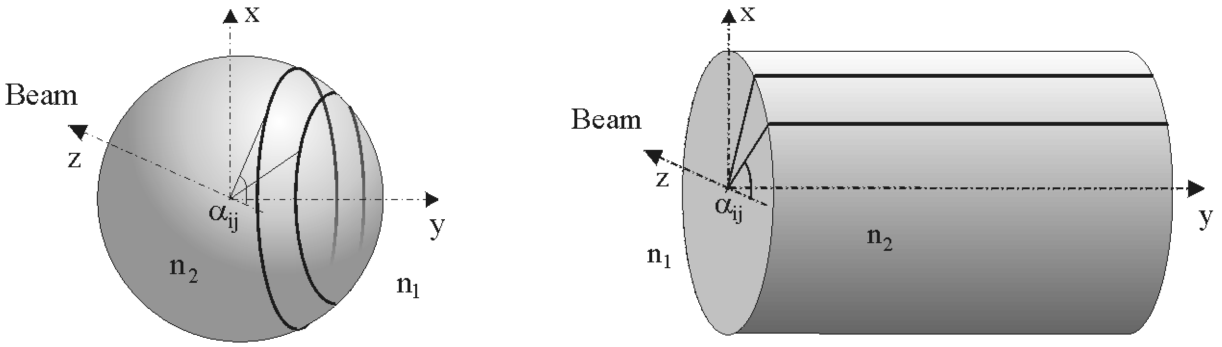

Figure 2-4 Geodetic lines marking the same incident angles α_{ij} at a constant azimuthal angle. For the single scattering sphere are found circles (left) and for the single scattering cylinder are determined lines (right).

Left: Single scattering sphere: Same incident angle α_{ij} are determined along circles (bold).
Right: Single scattering cylinder: Same incident angle α_{ij} along lines (bold) is found.

Each incident angle α_{ij} is correlated with a scattering angle $\Delta\theta_i$ (see Equation 2-4). Considering a single scattering sphere and cylinder as presented in Figure 2-4, the conditions for constant incident angles α_{ij} can be determined and the refraction conditions for the spherical and cylindrical scattering particle in the three-dimensional case can be defined.

Summarising briefly the assumptions made for the evaluation of the model:

(1) Each single scattering interaction is independent.
(2) Regarding single scattering particles on microscopic and mesoscopic scales, the interactions with X-rays are mainly caused by refraction.
(3) The refractive index for the single scattering particle is constant.
(4) Absorption effects of the scattering particle are neglected.
(5) Reflection at the interface is neglected.
(6) Restriction to spherical and cylindrical geometry for the single scattering particle.
(7) The two incident angles on the particle surface are approximately equal. (Good approximation for symmetric single scattering particles of a negligible real part δ of the refractive index *n*.)

As a result of the assumptions presented here, a relatively simple *model for scattering due to refraction* results, (see Equation 2-4), which is advantageous in terms of:

(1) Dependence of scattering angle $\Delta\theta_i$ on the incident angle α_{ij} on the first interface, and the real part δ of the refractive index *n*.
(2) Generalisation of the model for scattering due to refraction to the three-dimensional case by finding geodetic lines allows simplified handling and independence from particle geometry.
(3) Sphere and cylinder geometries resemble more complex biomedical structures.

Hence, essential is the probability distribution of incident angles α_{ij}, depending on the single scattering particle geometry. In sub-section 2.2, statistical considerations of the incident angles α_{ij} lead to the calculation of the scattering angle distribution of the single spherical and the single cylindrical scattering microparticle, and the single scattering power of both particle geometries. The generation of incident angles α_{ij} using the Monte-Carlo method and a ray tracing for single scattering as well as for multiple scattering of randomly distributed or micro scattering particles with a periodical substructure is introduced in sub-section 2.3.

2.2 Calculation of the scattering angle probability distribution for a single scattering event

The probability density of incident angles is strongly related to the probability density distribution of scattering angles $\Delta\theta$ (Equation 2-4). Thus statistical considerations are elaborated more precisely in this section. *Functions* identifying the probability distribution of scattering angles of the single scattering spherical and cylindrical particles are derived by statistical considerations (sub-section 2.2.1). These probability distributions lead in sub-section 2.2.2 to the single scattering power of the two particle geometries.

2.2.1 Feasibility study and evaluation of the scattering angle distribution by statistical considerations

Figure 2-5 presents the interface geometry of incident azimuthal angles α_i for a cylinder with homogeneous illumination and equal beam density of the volume.

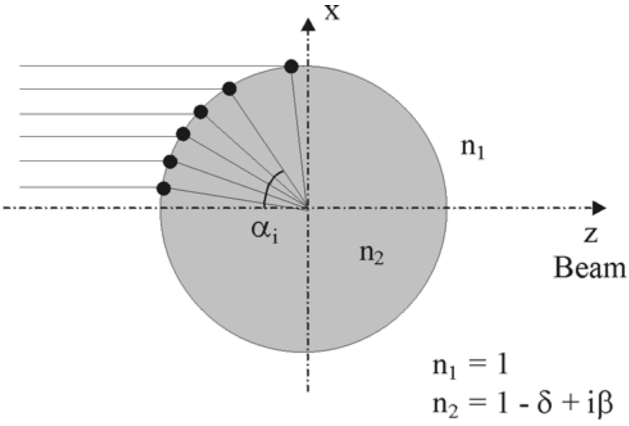

Figure 2-5 Interface geometry of incident azimuthal angles α_i of a cylindrical scattering particle with homogeneous illumination and equal beam density. Small incident angles α_i are more probable than larger ones.

Statistically it can be derived by using variate transformation [Brandt, 1999], that the probability distribution follows a cosine-function for incident azimuthal angles α_i of the cylinder. Thus it follows for the probability $p_{cylinder}$:

$$p_{cylinder}(\alpha_i) \propto \cos(\alpha_i) \qquad \textbf{Equation 2-5}$$

The probability distribution of scattering angles $\Delta\theta$ can be derived by substitution with the probability distribution of incident angles α_i as presented in Equation 2-6 [Brandt, 1999].

$$p(\Delta\theta) = p(\alpha_i(\Delta\theta)) \cdot \frac{d\alpha(\Delta\theta)}{d(\Delta\theta)} \qquad \textbf{Equation 2-6}$$

The first term from Equation 2-6 is determined by (i) Equation 2-4 and (ii) the probability of incident azimuthal angles α_i, in this case by the cylinder given by Equation 2-5. And the second term is given by derivation of the *model of scattering* from Equation 2-4 presented in Equation 2-7. Thus, the probability distribution of scattering angles $\Delta\theta$ for the cylindrical scattering particle is determined by Equation 2-8 (illustration see Figure 2-6, left).

$$\frac{d\alpha(\Delta\theta)}{d(\Delta\theta)} = \frac{1}{2\delta \cdot (1 + (\frac{\Delta\theta}{2\delta})^2)}$$ **Equation 2-7**

$$p_{cylinder}(\Delta\theta) \propto \frac{\cos(\arctan(\frac{\Delta\theta}{2\delta}))}{2\delta \cdot (1 + (\frac{\Delta\theta}{2\delta})^2)}$$ **Equation 2-8**

Considering now the spherical micro-scattering particle, the same statistical considerations using two-dimensional coordinate transformation [Brandt, 1999], deliver the probability of incident azimuthal angles α_i presented in Equation 2-9.

$$p_{sphere}(\alpha_i) \propto \sin(2 \cdot \alpha_i)$$ **Equation 2-9**

Applying Equation 2-6 and taking into account (i) Equation 2-4, (ii) the probability of incident angles α_i for the spherical particle (Equation 2-9) and (iii) Equation 2-7, the probability distribution for scattering angles $\Delta\theta$ of the single scattering spherical particle is determined as presented in Equation 2-10.

$$p_{sphere}(\Delta\theta) \propto \frac{\sin(2 \cdot \arctan(\frac{\Delta\theta}{2\delta}))}{2\delta \cdot (1 + (\frac{\Delta\theta}{2\delta})^2)}$$ **Equation 2-10**

The distribution functions $P(\Delta\theta)$ are shown in Figure 2-6 and it should be noted that by definition the angular deviation $\Delta\theta$ extends in the cylindrical case only in a plane perpendicular to the axis of the cylinder while for the spherical case it exhibits a rotational symmetry around the direction of the incoming ray since the scattering angle $\Delta\varphi$ remains undefined.

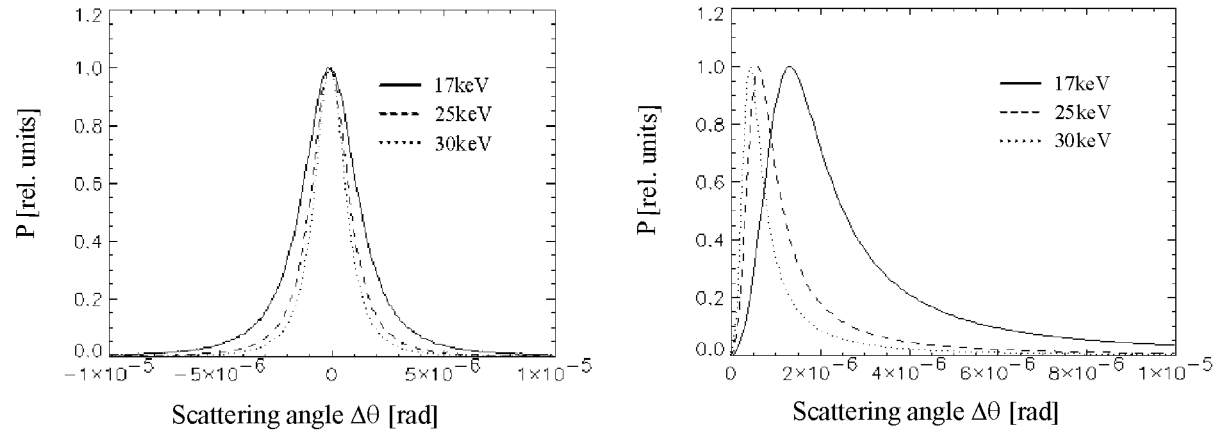

Figure 2-6 Scattering angle distributions Δθ for the single scattering microparticles presented for various photon energies.

Left: Scattering angle distributions for the cylindrical microparticle of PMMA given by Equation 2-8 at 17 keV, 25 keV and 30 keV photon energy.

Right: Scattering angle distributions for the spherical microparticle of PMMA from Equation 2-10 at 17 keV, 25 keV and 30 keV photon energy.

2.2.2 Scattering power for two different particle geometries

Angular distribution widths of general signals are enlarged due to signal spreading caused by multiple scattering, for example the monoenergetic X-rays reflected by an analyser crystal (see Figure 5-1), or a well defined refraction signal (sub-section 5.2.3).

The scattering power σ_{particle} is defined by the angular range of scattering events within 68.3% of a monoenergetic light source emitting parallel light, which is spread by scattering. Thus, σ_{particle} is defined as Gaussian width σ (see Figure 2-7).

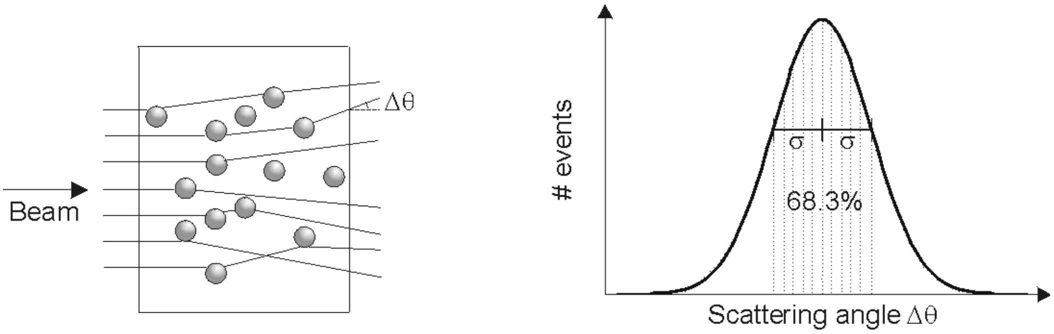

Figure 2-7 Influence of multiple scattering on a parallel incident signal

Left: Incident X-rays are deflected because of multiple scattering, the signal is spread.

Right: Definition of scattering power σ_{particle}: Spread signal due to the influence of multiple scattering, inside the angular range of 2σ are contained 68.3% of all events.

For the scattering power σ_{particle} is expected a linear dependence on the real part δ of the refractive index n: Far away form the absorption edges relates δ to the to the inverse square of photon energy $1/E^2$ (Equations 1-3). Thus, a similar relation is expected for the composition of independent microparticles. In addition is expected the single scattering power σ_{particle} to be dependent on the microparticle geometry, identified by a factor $f_{particlegeometry}$. As presented in this sub-section, the calculation of the single scattering power of the spherical and cylindrical microparticle identified by Equation 2-13 and Equation 2-16 is in agreement with these expectations.

Calculating the scattering power for a single scattering spherical and cylindrical microparticle requires determining σ_{particle} of the distributions for scattering angles $\Delta\theta$ given by the scattering angle distributions $\Delta\theta$ Equation 2-8 and Equation 2-10. Neither the distribution of scattering angles $\Delta\theta$ of the single scattering cylindrical particle nor the distribution of scattering angles $\Delta\theta$ for the spherical particle has a Gaussian shape. However it can be demonstrated that the distribution of scattering angles $\Delta\theta$ becomes a Gaussian-type shape for multiple scattering, if each single scattering process is independent (coherent scattering) (see sub-section 2.4), [Jackson, 1982]. Hence, the multiple scattering power is calculated performing the Central Limit Theorem of statistics using the scattering power of a single microparticle. Thus the calculated single scattering powers σ_{particle} play a major role in this work and are used several times for calculating multiple scattering powers of synthetic specimens as well as lung tissues (see section 2.5 and section 5.1).

The critical angle delimiting 68.3% of all scattering angles $\Delta\theta$ is calculated from the scattering angle distributions $\Delta\theta$ for the single scattering cylindrical and spherical particle given by Equation 2-8 and Equation 2-10. Instead of solving the integral of the scattering angle distribution $\Delta\theta$ (Equation 2-8 and Equation 2-10) the problem can be transformed to calculating the critical angle delimiting 68.3% of incident azimuthal angles α_i, because Equation 2-4 is a steadily increasing function.

Again, the probability distribution for incident azimuthal angles α_i of the cylindrical particle given by Equation 2-5 is used for the cylindrical microparticle. By building the integral in the range of $[0, \alpha_p]$, the total probability P for incident events within that range follows. Equation 2-11 presents the critical angle α_p for which a probability P is found.

$$\alpha_P = \arcsin(P)$$ **Equation 2-11**

Using Equation 2-4, the critical scattering angle $\Delta\theta_p$ within 68.3% of all scattering events are deflected is derived (Equation 2-12).

$$\Delta\theta_{P=0.683} = 2 \cdot \delta \tan(\arcsin(0.683))$$
$$\Delta\theta_{P=0.683} = 2 \cdot \delta \cdot 0.94$$ **Equation 2-12**

Thus, the scattering power σ_{particle} for the cylindrical microparticle, delimiting 68.3% of all scattering events, can be found as presented in Equation 2-13.

$$\sigma_{cylinder} = 1.87 \cdot \delta$$ **Equation 2-13**

Considering now the spherical scattering microparticle with an incident angle α_p: The probability distribution of incident angles α_i to a spherical microparticle given by Equation 2-9 delivers the total probability P for incident azimuthal angles α_i in the range of $[0, \alpha_p]$ described by Equation 2-14.

$$\alpha_P = \frac{1}{2} \cdot \arccos(1 - 2 \cdot P)$$ **Equation 2-14**

The critical angle $\Delta\theta_p$ within 68.3% of all scattering events are deflected can be calculated with Equation 2-4 and it follows Equation 2-15.

$$\Delta\theta_{P=0.683} = 2 \cdot \delta \tan(\frac{1}{2} \cdot \arctan(1 - 2 \cdot 0.683))$$

$$\Delta\theta_{P=0.683} = 2 \cdot \delta \cdot 1.47$$ **Equation 2-15**

Hence, the correlated scattering power $\sigma_{particle}$ for the single spherical microparticle can be expressed as:

$$\sigma_{sphere} = 2.93 \cdot \delta$$ **Equation 2-16**

Calculations of different scattering powers for a single micro-sphere made of PMMA at various energies are presented in Table 2-1.

Table 2-1 Calculated scattering power σ_{sphere} for a single micro-sphere made of PMMA at various energies, refractive index δ from http://www-cxro.lbl.gov

Energy [keV]	σ_{sphere} [µrad]
17	2.71
25	1.26
30	0.87

This section introduced the calculation of the scattering power $\sigma_{particle}$ of a single spherical and cylindrical microparticle by applying the incident angle distributions of Equation 2-9 and Equation 2-5, and the *model of scattering due to refraction* described by Equation 2-4. Defining the scattering power $\sigma_{particle}$ as range within 68.3% of all scattering events are found delivered approximately $\sigma_{cylinder} \approx 2 \cdot \delta$ and $\sigma_{sphere} \approx 3 \cdot \delta$.

2.3 Evaluation of model simulations of single and multiple scattering by using the Monte-Carlo method

The evaluation of the model described in section 2.1 is performed by conventional Monte-Carlo simulation and programming Monte-Carlo procedures using the programming tool IDL [RSI] V5.2 and V5.6. IDL is a C++ based programming language and allows in addition immediate visualisation of results.

The Monte-Carlo simulation meets the following requirements:

(1) Three-dimensional simulation of multiple scattering.
(2) Consideration of scattering on the basis of micro-scattering particles by the *model of scattering due to refraction* of section 2.1.
(3) Particle geometries: spherical and cylindrical micro-scattering particles.
(4) Size of micro-scattering particle: any.
(5) Packing density: variable.
(6) Multi-layer (multiple scattering) specimen simulation.
(7) Various specimen structures: random distribution of micro-scattering particles, or micro-scattering particles arranged in a periodical structure.
(8) Simulations for various energies: 17 keV, 25 keV, 30 keV, 40 keV, and 60 keV.
(9) Simulation for any Si (111) analyser crystal reflectivity.
(10) Scattering material: PMMA (polymethylmethacrylate).
(11) Recording of the scattering angle distribution $\Delta\theta$ after the specimen interactions, simulated image and protocol file, requiring all relevant data of the simulation.

Monte-Carlo simulations are performed for simulating multiple scattering processes. A distribution of scattering microparticles is generated according to the demanded substructure of the specimen (description see below). 3D ray tracing is used. It is iteratively performed on the generated microparticle distribution, which represents the specimen: An X-ray photon intersects the specimen at a random position, which is simulated using the IDL random generator. If the X-ray photon hits a microparticle, the deviation is calculated, using Snell's law, and the probability of absorption is calculated. Computionally, the calculation is realised by operating a three-dimiensional rotation modelling the refraction and a transmission realising the absorption according to Equation 2-1. Selecting spherical coordinates simplyfies the task. The computional method of matrix parametrisation effects a fast iterative computer processing. Every X-ray photon is traced, independently if it hits a microparticle or not. The process is iterated as the X-ray proceeds through the specimen, with the previous angular deflections accounted for. If the X-ray photon is not absorbed, it exits the specimen with the resultant scattering angle Δθ and the scattering angle is registered in a histogram and the image plane position of the X-ray photon is recorded. The simulation is iterated *m* times to provide good statistics. A protocol file contains all relevant data of the simulation. The schematic program structure of the Monte-Carlo ray tracing is presented in Figure 2-8.

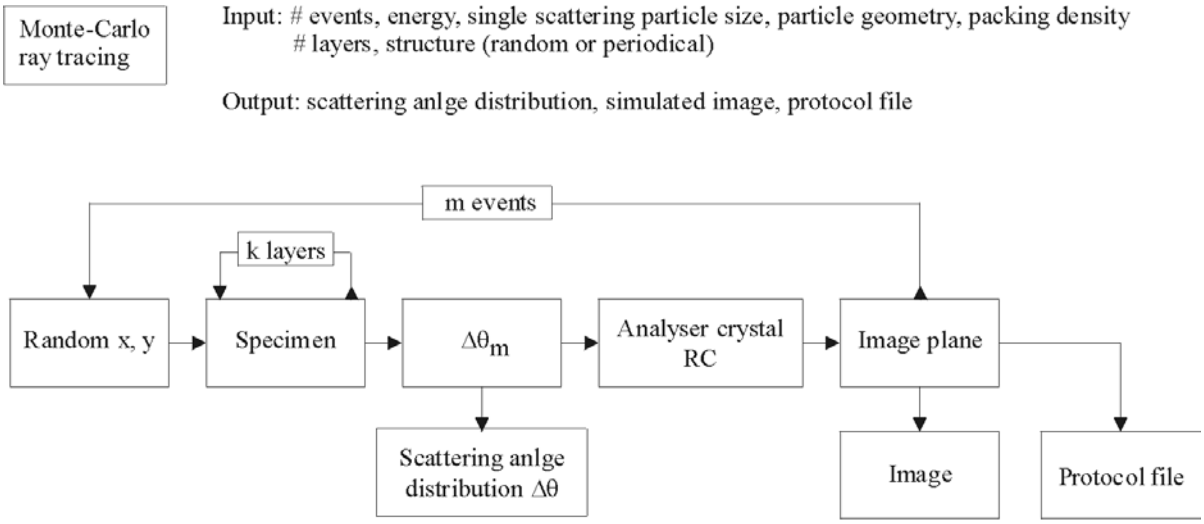

Figure 2-8 Scheme of the 3D ray tracing for Monte-Carlo simulation on multiple scattering processes. The specimen structure implementation is described below.

For the computational simulation of specimens composed of single cylindrical microparticles or spherical microparticles are the two particle geometries embedded in a unit-cell as presented in Figure 2-9.

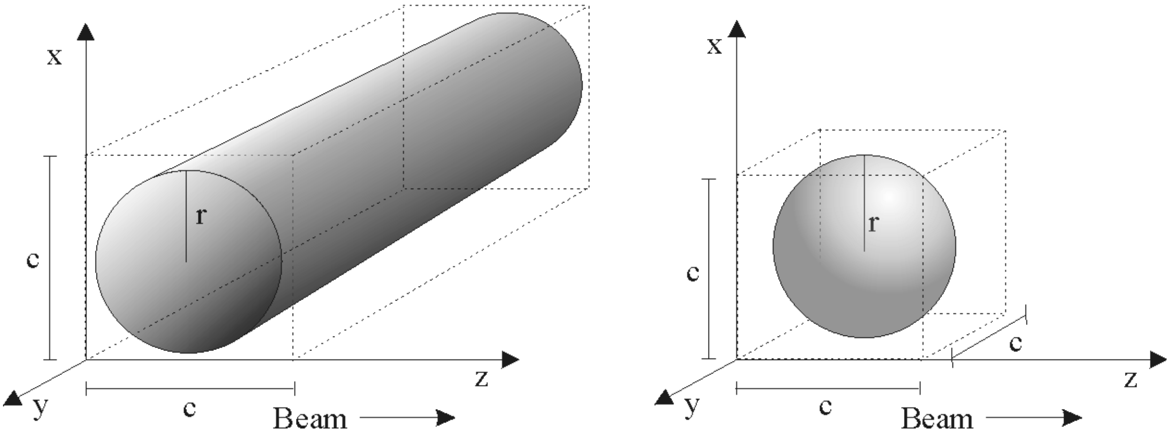

Figure 2-9 Illustration of embedding a single scattering particle in a unit-cell. Left: The single scattering cylinder in the unit-cell, beam in the z-direction. Right: The single scattering sphere in the unit-cell, beam in the z-direction.

The unit-cell serves for including the packing density to the Monte-Carlo simulation: The particle radius r and the size of the unit-cell c are input parameters. Thus, the ratio of c to r fixes the packing density of the simulated specimen. For instance, a unit-cell size of $c = 2 \cdot r$ leads to a packing density of 78.5% (cylinder) and 52.3% (sphere). The unit-cells containing the microparticles arrange a single net layer as illustrated in Figure 2-10.

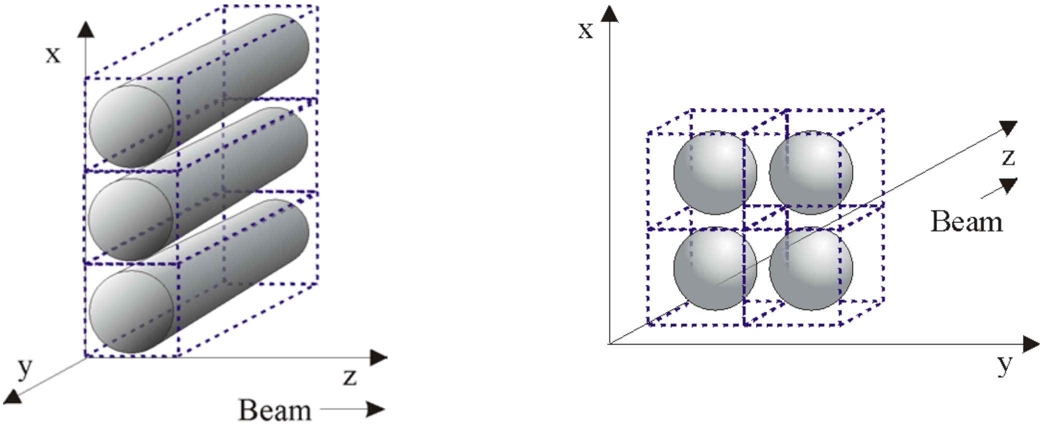

Figure 2-10 Illustration of single net layers composed of unit-cells of the microparticles for the cylindrical particle (left) and the spherical particle (right).

Since the analyser crystal is sensitive to the projected angle with respect to the Bragg-plane, the corresponding projected angle $\Delta\theta_{proj}$ is calculated. For the cylindrical case the angle $\Delta\theta$ and its distribution is unchanged while for the spherical case the projection is calculated assuming a flat distribution of the azimuth angle $\Delta\varphi$ [Walenta] as shown in Figure 2-11 right.

It is noticed that the comparison to a Gaussian with the same rms-deviation shows significant differences since the scatter distribution exhibits very large scatter angle (grazing incidence).

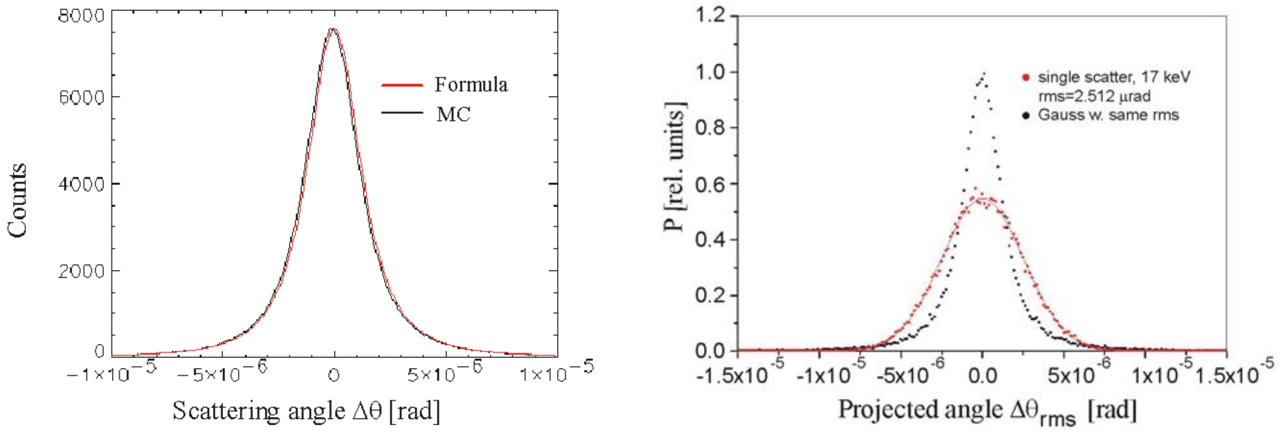

Figure 2-11 Scattering angle distributions Δθ with respect to the analyser crystal plane for the cylindrical (left) and spherical (right) microparticle calculated by Monte-Carlo ray tracing performed on a single net layer (black line). Exemplary are demonstrated the calculations on a PMMA microparticle @17 keV photon energy.

Monte-Carlo simulations were performed assuming 10^7 events and neglecting absorption. For comparison, the distributions of scattering angles Δθ given by Equation 2-8 and Equation 2-10 are normalised to the maximum of Monte-Carlo simulations.

Simulating structures: Microparticles structured in a periodical order are used for the simulations of the lithography specimens (see Figure 4-6, Figure 4-7 and Section 5.3). These specimens contain arranged cylindrical holes. The influence of substructures is studied by rotating the specimens, which causes a fix shift of the microparticles in each layer. Figure 2-12 illustrates the computational simulation of the lithography specimen.

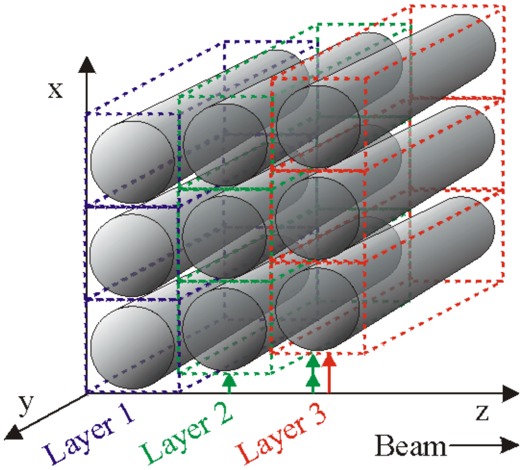

Figure 2-12 Computational simulation of a specimen with a periodical structure. Each net layer (blue, green, red) containing the single scattering particles is shifted by a fix parameter (green arrow). The green and the red arrow mark the shift respective to the first net layer. As many as necessary layers are simulated by this method, where the shift is an input parameter of the Monte-Carlo procedure.

Simulating random distributions: Randomly distributed microparticles are used for simulating multiple scattering properties of the sphere specimens (see Figure 4-1 and Section 2.4). The simulation of random distributions is much more delicate than the simulation of a periodical structure, because with a certain number of microparticles has to be simulate a sufficient randomness. Figure 2-13 and Figure 2-14 describe how to gain computationally a sufficient randomness of microparticles.

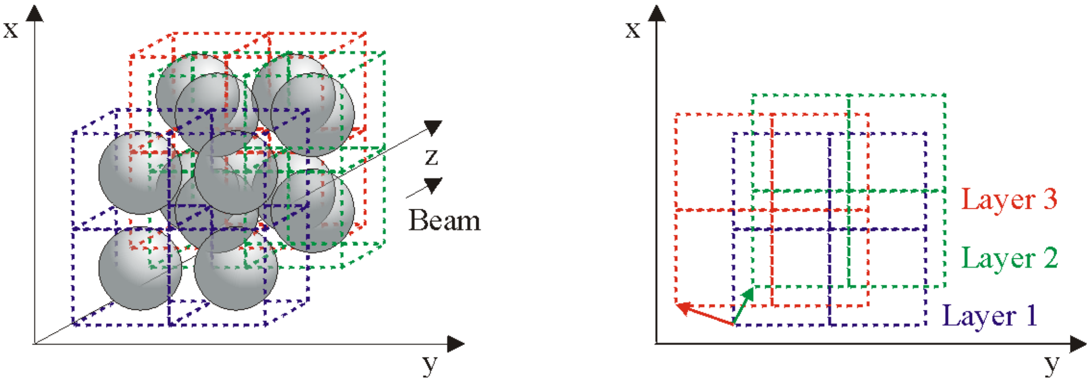

Figure 2-13 Illustration of the net layer configuration for arranging a random microparticle configuration. Left: Arrangement of the net layer configurations, presented for three net layers (blue, green, red). Right: The arrangement of the net layer configurations illustrated in projection (blue, green, red). Each net layer is shifted by a random shift (green arrow and red arrow). The shifts are generated using the random generator of IDL. As many as necessary layers are constructed by this method, where the number of layers is an input parameter of the Monte-Carlo procedure.

Many net layer configurations are necessary to provide a sufficient randomness of the simulated specimen. Thus various net layer configurations are generated. From each net layer configuration is cut a slice, which serves as a representative slice of the simulated specimen (Figure 2-14).

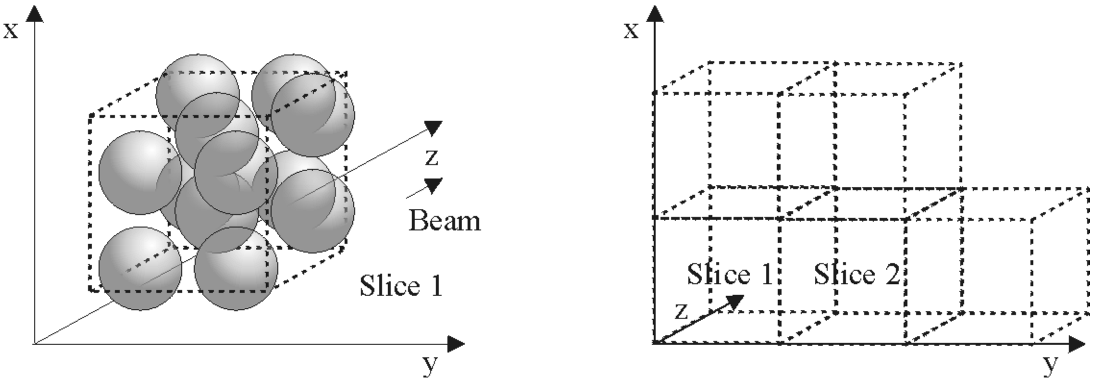

Figure 2-14 Simulation of a specimen by arranging many net layer configurations.

Left: From the net layer configuration in Figure 2-13 (left) is cut the inner part and serves as a representative slice of the simulated specimen.

Right: The specimen is composed of many net layer slices. The number of net layer slices as well as the slice size is input parameters of the Monte-Carlo processing.

The Monte-Carlo ray tracing is performed slice by slice: An X-ray photon intersects the slice, simulated by the IDL random generator, and passes the specimen slice like described in the Monte-Carlo ray tracing (see above and Figure 2-8). Each slice is performed *m* times to provide good statistics.

2.4 Multiple scattering for weakly absorbing microparticles

Multiple scattering was pioneered by Molière, Snyder and Scott, Goudsmit and Saunderson, and Lewis in the late forties and early fifties of the last century, investigating multiple scattering of charged particles, and identify the principles of multiple scattering in general [Bethe, 1953].

Monte-Carlo multi-scattering simulations performed on the *model of scattering due to refraction* demonstrate the agreement with the principles of multiple scattering (sub-section 2.4.1). Specially the development of the Gaussian fraction of the multiple scattering angle distribution $\Delta\theta$, resulting from single small angle scattering, leads to the calculation of the multiple scattering power by using the Central Limit Theorem and the scattering power σ_{particle} of the single microparticle. Good Agreement for weakly absorbing single microparticles is demonstrated in sub-section 2.4.2.

2.4.1 Principles of multiple scattering

It is assumed that each interaction of the X-ray with the microparticle is an independent scattering. Hence the multiple scattering process is dominated by the coherent addition of the small angle scattering single amplitudes (coherent scattering). Just a few scatterings form a Gaussian shape from the portion of small scattering angles Δθ, whereas the tails of the distribution resulting from a minor part of single large angle scattering [Bethe, 1953]. The more scattering events, the more dominates the Gaussian fraction and covers the single large angle scattering portion [Jackson, 1982]. The statements are in agreement with measurements made for the PMMA sphere specimens: The recorded scattering angle distributions Δθ demonstrate clearly a Gaussian shape (see Figure 5-1). Monte-Carlo simulations are performed on randomly distributed micro spheres, assuming various numbers of net layers. Each scattering process starts with a vector in space defined by the polar angle θ and an azimuth φ. The scattering angles Δθ and Δφ are randomly generated and then the resulting new vector with angles θ′ and φ′ are calculated using the geometrical procedure as described in [Chan and Doi, 1988]. Finally the vector is projected on the scattering plane. Figure 2-15 shows a few examples for E = 17 keV for 1 scatter event, 4 and 16.

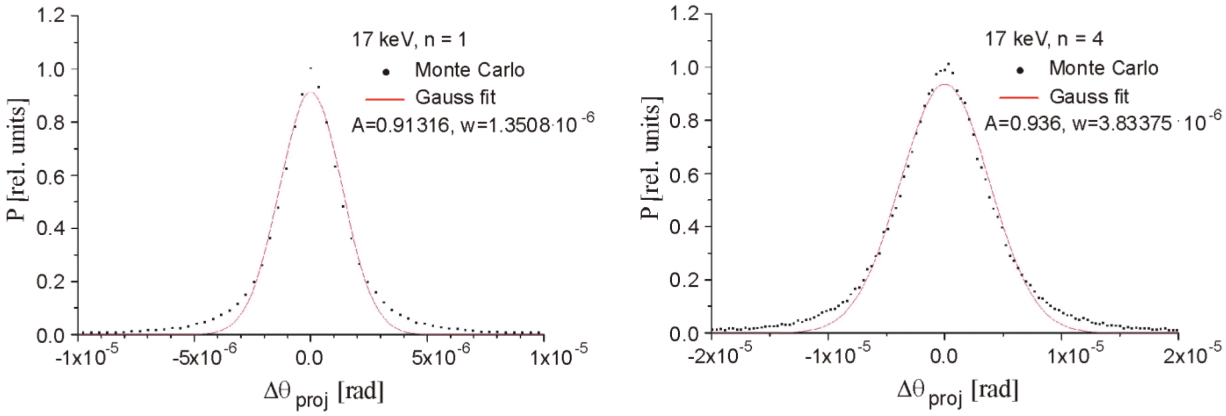

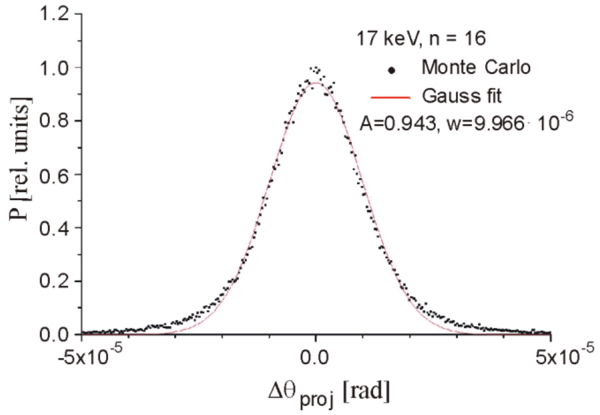

Figure 2-15 Monte-Carlo simulated scattering angle distributions Δθ (black) with Gaussian fit (red) for various numbers of net layers containing spherical microparticles. The Monte-Carlo simulations were performed on PMMA microspheres with a packing density of 52.3% @17 keV photon energy, absorption is neglected.

The Gaussian fits show clearly the improved approximation with a larger number of scatter processes. It is also clear that only the square of rms-values can give a linear dependence on the number scattering processes (see also Figure 2-18). Therefore these values are used in the following.

The large angle single scattering fit in Figure 2-15 is derived from the large angle scattering approximation given by Equation 2-10:

$$p_{sphere,\Delta\theta>>}(\Delta\theta) = \frac{2\cdot\delta}{(2\cdot\delta)^2 + \Delta\theta^2}$$

The Multiple scattering simulations presented in Figure 2-15 are in good agreement with common multiple scattering properties: (i) the Gaussian portion, resulting from small angle scatterings, becomes more dominant for increasing number of scattering layers and covers (ii) the large angle single scattering fraction. In summary, the multiple scattering angle distribution Δθ becomes a more Gaussian shape, the more scattering net layers are included. This demonstrates clearly a plot of χ^2 of the Gaussian fit to the simulated scattering angle distributions versus the number of net layers (Figure 2-16).

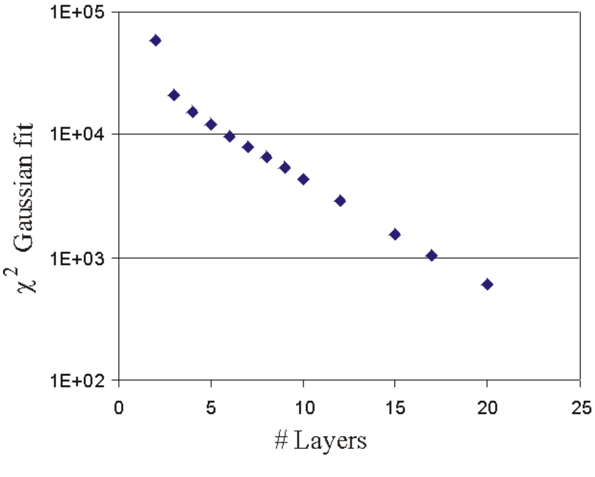

Figure 2-16 χ^2 of Gaussian fit to Monte-Carlo simulated scattering angle distributions versus the number of net layers.

The number of degrees of freedom for the Gaussian fit is 1023. With the quantile $Q(\chi^2_{P=0.99})=1131$ [MedWebMünster, 2004] follows the scattering angle distribution for 17 layers and more a Gaussian shape.

Thus, the scattering angle distribution Δθ of a multiple scattering process derived from *the model of scattering due to refraction* demonstrates the general principles of multiple scattering. If each single scattering is assumed to be independent, a Gaussian shape is developed for multiple scattering, dominating the scattering angle distribution Δθ.

2.4.2 Calculation of multiple scattering power for randomly distributed scattering particles using the Central Limit Theorem of statistics

A multiple scattering specimen is assumed to be composed of equally shaped microparticles of the same material. If each scattering is independent can be applied the Central Limit Theorem of statistics [Jackson, 1982].

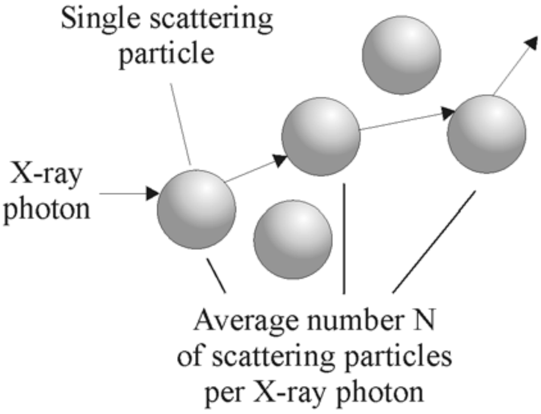

Figure 2-17 Multiple scattering process with *N* scattering particles per X-ray photon.

With σ_{particle} as the single scattering power of each particle and *N* as the average number of scattering particles, follows the multiple scattering power σ_{specimen}:

$$\sigma_{specimen} = \sqrt{N \cdot \sigma_{particle}^{2}} \qquad \textbf{Equation 2-17}$$

The experimental agreement for the PMMA sphere specimens is demonstrated in sub-section 5.1.2. In sub-section 2.2.2 was calculated the single scattering power σ_{particle} for the cylindrical (Equation 2-13) and the spherical scattering particle (Equation 2-16) and Table 2-1 presents some single scattering powers σ_{particle} for the PMMA micro sphere at various energies.

Next, the two-dimensional projection of incident angular multiple scattering distribution onto the analyser crystal plane is considered for the energies E=17 keV, 25 keV as well as 30 keV. The calculations are illustrated in Figure 2-18.

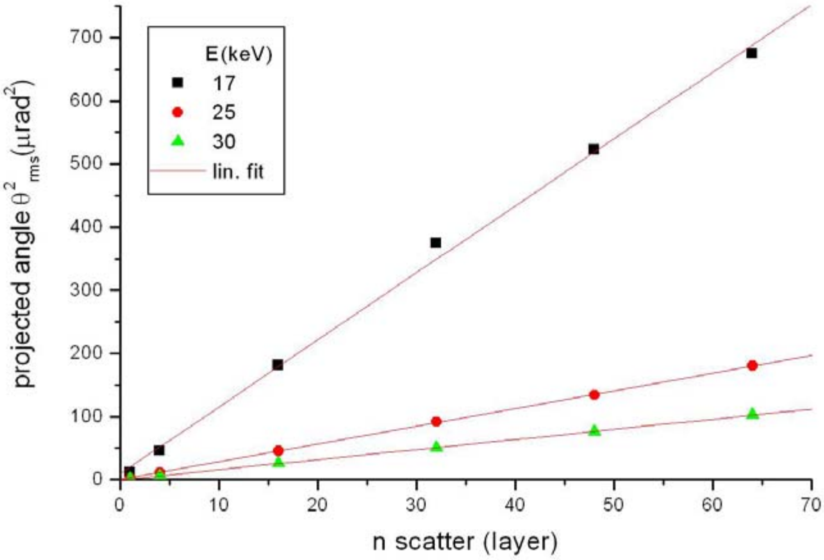

Figure 2-18 Square of projected incident multiple scattering power onto the analyser crystal plane. A random distribution with a packing density of 52.3% of the PMMA spheres is assumed, absorption is neglected.

In comparison to the projected incident multiple scattering power onto the analyser crystal plane (Figure 2-18) with the calculated multiple scattering power by Equation 2-16 and Equation 2-17 it is noticed that the slope has changed. Therefore it is sufficient for all later comparison with measured values to use correction factors. These scaling factors can be directly derived by comparison of the slopes as presented in Table 2-2.

Table 2-2 Scaling factors resulting from multiple scattering power and projection of multiple scattering angle $\Delta\theta$ for various energies.

Energy [keV]	Scattering values onto the analyser crystal plane	Scattering values by Equation 2-16	Ratio
17	541/50	370/50	1.46
25	139/50	80/50	1.73
30	77.9/50	37.6/50	2.07

Thus, multiple scattering power $\sigma_{specimen}$ of specimens containing weakly absorbing and randomly distributed scattering microparticles can be identified by:

$$\sigma_{specimen} = \sqrt{N} \cdot f_{particlegeometry} \cdot \delta$$ **Equation 2-18**

With:

N: Number of X-ray interactions with the microparticles

δ: Real part of the refractive index n

$$f_{particlegeometry} = \begin{cases} 1.87 : cylinder \\ 2.93 : sphere \end{cases}$$

The main argument for applying the Central Limit Theorem is the independence of each single scattering event. The independence is no longer fulfilled, if (i) the single scattering is an inelastic scattering and absorption might become a crucial influence, or (ii) the scattering particles are arranged in a periodical order.

In case of absorption, the fraction of small angle scattering is decreasing (see sub-section 2.6.1). Thus, the development of the Gaussian shape, resulting from small angle scatterings is suppressed. And the incoherent scattering portion of large angle scattering becomes more important ([Jackson, 1982] and Molière's Theory [Bethe, 1953]).

The synthetic specimens as well as lung tissues used in this work are weakly absorbing within the energy range used in this work. Beyond, low absorption is a preferred effect in medical applications of phase contrast methods (see Introduction). Using the single scattering power $\sigma_{particle}$ and the Central Limit Theorem delivers good agreement with the measurements (see sub-section 5.1.4).

A strong influence on multiple scattering power is observed, if the scattering microparticles are arranged in a periodical order. Monte-Carlo simulations performed on 20 net layers demonstrate the effect. This time, the simulation is performed on only one slice and in comparison to Figure 2-18 appears a variety of multiple scattering powers resulting from the particle configuration of various single slices (see Figure 2-19).

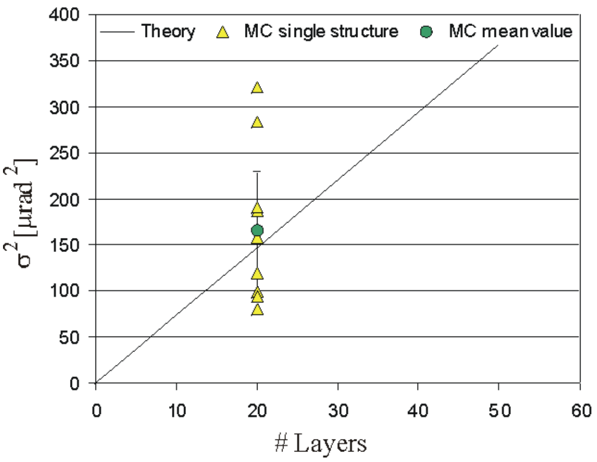

Figure 2-19 Variety of multiple scattering powers resulting from substructures. The figure demonstrates the square of multiple scattering power calculated by using Monte-Carlo multi-layer simulations (MC) (yellow triangles). For each simulation one slice was generated (see section 2.3) and was iterated 10^6 times. For comparison is plotted the multiple scattering power by the single scattering power Table 2-1 and the Central Limit Theorem (black line) and the mean value of the Monte-Carlo simulations (green circle). The Monte-Carlo simulations are performed on PMMA spheres and a packing density of 52.3% exemplary @17 keV photon energy, absorption is neglected.

Figure 2-19 demonstrates clearly the influence of substructures on multiple scattering power. More about the influence of substructures is presented in section 5.3.

2.5 Application to soft tissue: Calculations for multiple scattering power of lung tissue

In this section, the *model of scattering due to refraction* is applied to biological multi-scattering specimens, especially to lung tissue. Assuming that the alveoli inside the lung are responsible for multiple scattering of lung tissue, the scattering power for a single alveolus containing air is calculated in sub-section 2.5.1. The multiple scattering power of lung tissue and alveoli resulting from the calculated scattering power of a single alveolus are predicted (sub-section 2.5.2).

2.5.1 Application of lung tissue to the model

The alveoli at the end of the bronchi inside the lung of an animal are responsible for the multiple scattering properties of lung tissue. In Figure 2-20 is presented a medical illustration of alveoli.

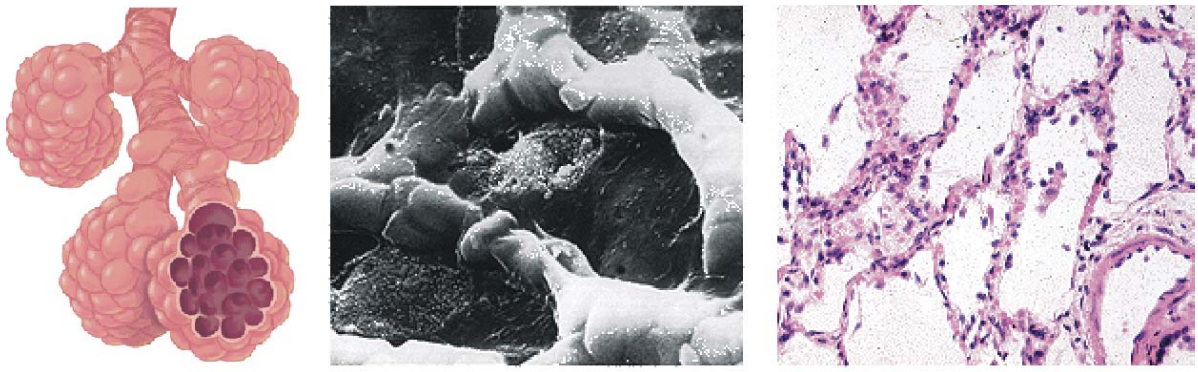

Alveoli

Scanning Electron Micrograph
Normal Alveoli

Histology Section
Normal Alveoli

Figure 2-20 Illustration of alveoli from: Johns Hopkins School of Medicine's [Hopkins, 2004]
Left: Alveoli as final branching of the respiratory tree
Middle: Scanning electron micrograph of alveoli
Right: Histological cut of alveoli

A sphere is usually applied in medicine in order to represent an alveolus [Hills, 1999], [Kreck et al., 2001]. In addition, a constant refractive index for the tissue around the alveolus and the alveolar air is assumed. The model of the alveolus used in this work is presented in Figure 2-21.

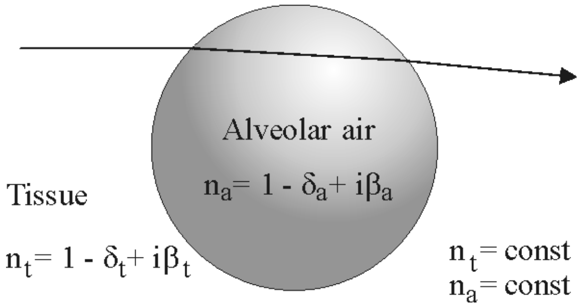

Figure 2-21 Sphere model of an alveolus: the sphere represents the alveolus. The tissue around the sphere and the alveolar are of constant refractive index.

Table 2-3 demonstrates the composition of some typical alveoli sizes of animals:

Table 2-3 Selection of some typical alveoli sizes of animals

	Alveoli size [µm]
Bat	35 [Duncker, 2004]
Rat	70.2 ± 6.6 [Mollenhauer, 2003]
Rabbit	78 [Mollenhauer, 2003], [Scarpelli, 2000]
Human	150-230 [Duncker et al., 2003]
Cow	250-500 [Duncker, 2004]

As can be seen in Table 2-3, typical alveoli sizes are on mesoscopic scales and the requirements for using the *model of multiple scattering due to refraction* are fulfilled.

Table 2-4 presents the components of alveolar air and their fractions.

Table 2-4 Composition of alveolar air [Faller et al., 1999], components and fractions of alveolar air.

Compound	Fraction [%]
N_2 and inert gases	73.8
O_2	14.0
CO_2	5.6
H_2O	6.6

The scattering power of a single spherical microparticle depends on the real part of its refractive index as demonstrated by Equation 2-16. Thus, the total real part of the refractive index δ_{total} of the "tissue-alveolar air"-refraction process [Figure 2-21] has to be determined. $\delta_{rel,i}$ describing the refraction of each gas component *i* can be identified as:

$$\delta_{rel,i} = \frac{\delta_{ai} - \delta_t}{1 - \delta_t}$$ **Equation 2-19**

Taking into account the fractions f_i of the compound (Table 2-4), δ_{total} is described by Equation 2-20.

$$\delta_{total} = \sum f_i \cdot \delta_{rel,i}$$ **Equation 2-20**

Refractive indices are tabulated by [Gullikson, 2004]. For the calculations is the real part of the refractive index of tissue around the alveoli approximated with $\delta_{t,25keV} = 3.53 \cdot 10^{-7}$. Thus, the total real part of the refractive index δ_{total} for an alveolus at 25 keV photon energy is given as:

$$\delta_{alveolus,25keV} = 3.53 \cdot 10^{-7}$$

Applying Equation 2-16, the single scattering power for a single alveolus is:

$$\sigma_{alveolus,25keV} = 1.035 \mu rad$$

2.5.2 Prediction of multiple scattering power of lung tissues and alveoli

Multiple scattering of lung tissue is considered as follows: Assuming that the alveoli are distributed randomly, the multiple scattering power of lung tissue at 25 keV photon energy can be calculated by applying the Central Limit Theorem (Equation 2-17) and the calculated $\sigma_{alveolus,\ 25keV}$. Figure 2-22 presents the calculated multiple scattering power of 12 mm lung tissue at 25 keV versus the alveoli diameter.

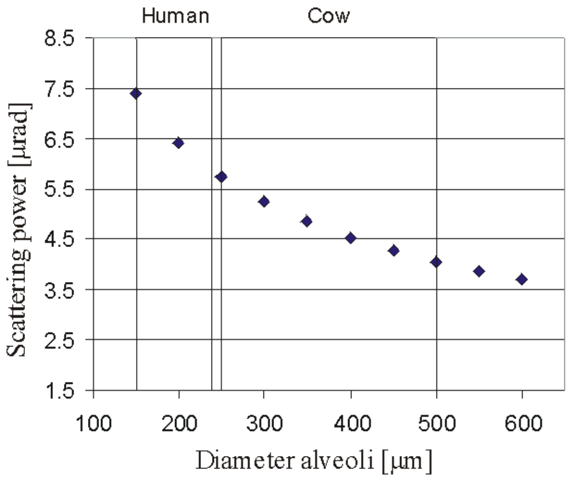

Figure 2-22 Calculated multiple scattering power of 12 mm thick lung tissue @25 keV photon energy versus alveoli diameter.

The packing density of alveoli is assumed to be 64% [Chan and Doi, 1988] **Chan, H. P. and K. Doi, (1988). Monte *Carlo Simulation in Radiological Science. Ed.* Morin, L. , CRC Press Inc.**

[Donev et al., 2004].

Regions of human and cow alveoli sizes are marked.

To summarise, in this sub-section the *model of multiple scattering due to refraction* is applied to lung tissue. The scattering power for a single scattering alveolus $\sigma_{\text{alveolus, 25keV}}$ is calculated. By using the scattering power of a single alveolus, the multiple scattering power of lung tissue is derived with the assumption that the alveoli are distributed randomly inside the lung tissue specimen. The multiple scattering power versus alveoli size is calculated assuming a packing of the alveoli. The calculations for lung tissue at 25 keV and assuming a thickness of 12 mm lung tissue in this section was done with the purpose of comparing the predictions with experimental data introduced in chapter 5, where analysis of the cow lung tissue specimen of the experiment is presented (sub-section 5.1.5).

2.6 Considering limits of the model for multiple scattering

Multiple scattering is considered due to refraction, which delivers a good approximation for forward scattering in the energy range used within this work [Kirz et al., 1995]. Some additional assumptions were made to evaluate the *model for multiple scattering due to refraction*, which are considered and legitimised in this section. Main assumptions made are (i) neglecting absorption and (ii) approximating the two incident angles onto the interface surface. Both assumptions contributed to simplify significantly the considerations of multiple scattering. Furthermore the influence of total external reflection is discussed.

2.6.1 Influence of absorption on multiple scattering

Absorption was neglected in the elaboration of the *model of scattering due to refraction* in section 2.1. Monte-Carlo simulations are performed assuming in addition absorption caused by various sphere sizes of a single scattering spherical particle. The results are illustrated in Figure 2-23.

Single scattering micro spheres of a diameter up to 100 μm show more or less the same scattering angle distribution $\Delta\theta$. Visible effects in the scattering angle distribution $\Delta\theta$ occur at 17 keV photon energy for PMMA spheres of about 1 mm (see Figure 2-23). The simulation of the 10 mm diameter sphere clearly demonstrates the influence of absorption: X-rays incident with small angles α_{i1} to the sphere interface are absorbed more than X-rays incident with a larger angle α_{i1}.

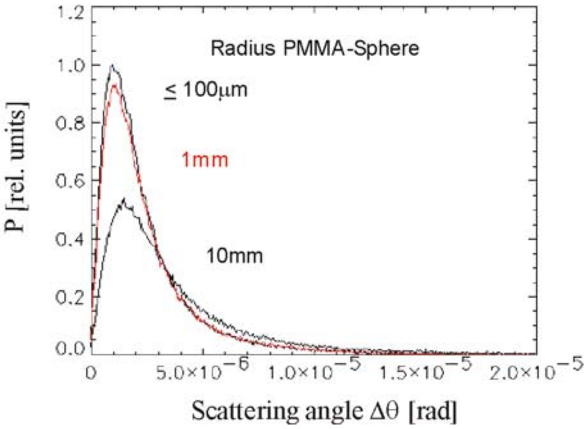

Figure 2-23 Influence of absorption on the projected scattering angle distribution Δθ with respect to the analyser crystal for various sizes of a PMMA sphere @17 keV photon energy calculated by Monte-Carlo simulations using the model of scattering due to refraction. For each simulation were performed 10^6 events.

The decrease of the small angle scattering portion is important for multiple scattering, because the development of the Gaussian fraction of the multiple scattering angle distribution Δθ results from superposition of small angle scatterings. Therefore, scattering is increasingly favoured over absorption so long as the superposition continues to be coherent [Kirz et al., 1995]. Hence, increasing absorption of the microparticles or increasing thickness of the specimen limits the calculation of multiple scattering power by using the scattering power of a single microparticle (Equation 2-18) [Jackson, 1982].

For the specimens and photon energies used in this work seems neglecting absorption a good approximation.

2.6.2 Justifying the approximation of the incident angles in the model for multiple scattering

For the elaboration of the *model of scattering due to refraction* it was assumed that the angles α_{i1} and α_{i2} at both interfaces (Figure 2-3) are approximately equal. The difference of scattering angle Δθ with and without the approximation is calculated and plotted in Figure 2-24. Over a large angular range covering approximately the whole hemisphere for both spherical and cylindrical geometry, it is demonstrated to be a good approximation. An accuracy of the approximated scattering angle of 0.2% is achieved for the spherical particle for about 99.5%, and for the cylindrical particle about 99.8% of all events intersecting the particle (see the red square in Figure 2-24).

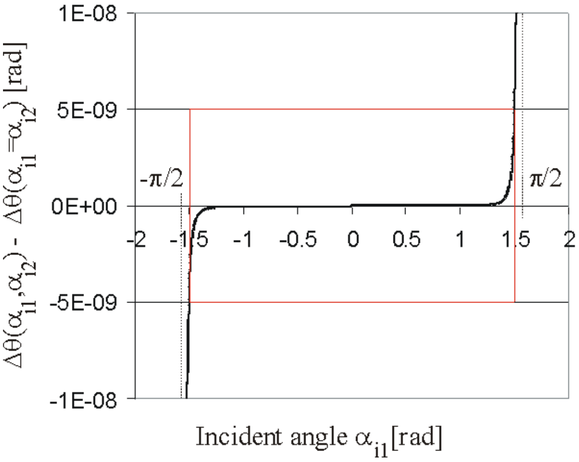

Figure 2-24 Calculated difference of scattering angles $\Delta\theta$ between scattering angle taking into account the calculated incident angle on the second interface α_{i2} and the scattering angle resulting from the approximation $\alpha_{i2}=\alpha_{i1}$ by the model of scattering due to refraction assuming PMMA @ 17 keV photon energy.

Thus the relative error of the determined scattering angle $\Delta\theta$ assuming the approximation is less than 0.2% for more than 99% of scattering events. Especially for small angle scattering, important for multiple scattering (see section 2.4), is the approximation very good.

2.6.3 The influence of total external reflection

Finally the singularity of Equation 2-4 describing the model of multiple scattering is discussed. The singularity occurs at incident angles $-\pi/2$ and $\pi/2$. In reality, the singularity is never reached: For the critical angle of incidence α_c and more, the incident X-ray does not penetrate into the material, but rather propagates along the interface. The critical angle of incidence α_c with δ is the real part of the refractive index *n* and neglecting absorption is identified by [Attwood, 1999]:

$$\alpha_c = \frac{\pi}{2} - \sqrt{2 \cdot \delta}$$

Equation 2-21

For a PMMA sphere at 17 keV photon energy this corresponds approximately to a maximum refraction angle $\Delta\theta$ of about 1.4 mrad and a fraction of backscattering of approximately 0.004%. Thus, the maximum refraction angle $\Delta\theta$ is limited for a single scattering. But this fact should be not important for this work, neither for the contribution to an additional extinction contrast in X-ray imaging nor for multiple scattering.

References

[Attwood, 1999] Attwood, D. T. (1999). *Soft X-Rays And Extreme Ultraviolet Radiation.* Cambridge University Press.

[Bethe, 1953] Bethe, H. A. (1953). *Molière's theory of multiple scattering.* Phys. Rev. **89**(6): 1256-1266.

[Born et al., 1999] Born, M. and E. Wolf (1999). *Principles of optics: Electrodynamic theory of propagation, interference and diffraction of light.* Cambridge University Press.

[Brandt, 1999] Brandt, S. (1999). *Datenanalyse.* Spektrum Akademischer Verlag GmbH Heidelberg, Berlin.

[Chan and Doi, 1988] Chan, H. P. and K. Doi, (1988). *Monte Carlo Simulation in Radiological Science*. Ed. Morin, L. , CRC Press Inc.

[Donev et al., 2004] Donev, A., I. Cisse, D. Sachs, E. A. Variano, F. H. Stillinger, R. Connelly, S. Torquato and P. M. Chaikin (2004). *Improving the Density of Jammed Disordered Packings Using Ellipsoids.* Science **303**: 990-993.

[Duncker, 2004] Duncker, H.-R. Prof. em. Dr. Dr. (2004). Anatomie u. Zellbiologie, Anatomie II, University of Gießen, Germany (Personal communication).

[Duncker et al., 2003] Duncker, H.-R. and W. Kummer (2003). *Atemsystem. Anatomie: Zellen- und Gewebelehre, Entwicklungslehre, Skelett- und Muskelsystem, Atemsystem, Verdauungssystem, Harn- und Genitalsystem.* Benninghoff and Drenckhahn. **1**: 533-583.

[Faller et al., 1999] Faller, A., M. Schünke and G. Schünke (1999). *Der Körper des Menschen - Einführung in Bau und Funktion.* Georg Thieme Verlag, Stuttgard.

[Fernandez et al., 2002] Fernandez, M., J. Keyrilainen, R. Serimaa, M. Torkkeli, M. L. Karjalainen-Lindsberg, M. Tenhunen, W. Thomlinson, V. Urban and P. Suortti (2002). *Small-angle x-ray scattering studies of human breast tissue samples.* Physics in Medicine and Biology **47**: 577-592.

[Gullikson, 2004] Gullikson, E. M. (2004). *CXRO's Home Page* http://www-cxro.lbl.gov (Electronic source).

[Hecht, 2001] Hecht, E. (2001). *Optik.* Oldenburg Wissenschaftsverlag GmbH.

[Hills, 1999] Hills, B. A. (1999). *An alternative view of the role(s) of surfactant and the alveolar model.* Journal of Applied Physiology **87**(5): 1567-1583.

[Hopkins, 2004] Hopkins, J. (2004). *Johns Hopkins School of Medicine's: Interactive Respiratory Physiology.* http://oac.med.jhmi.edu/res_phys/Encyclopedia/Menu.HTML (Electronic source).

[Jackson, 1982] Jackson, J. D. (1982). *Klassische Elektrodynamik.* Walter de Gruyter & Co.

[Kirz et al., 1995] Kirz, J., C. Jacobsen and M. Howells (1995). *Soft-X-Ray Microscopes and Their Biological Applications.* Quarterly Reviews of Biophysics **28**(1): 33-130.

[Kreck et al., 2001] Kreck, T. C., M. A. Krueger, W. A. Altemeier, S. E. Sinclair, H. T. Robertson, E. D. Shade, J. Hildebrandt, W. J. E. Lamm, D. A. Frazer, N. L. Polissar and M. P. Hlastala (2001). *Determination of regional ventilation and perfusion in the lung using xenon and computed tomography.* Journal of Applied Physiology **91**(4): 1741-1749.

[MedWebMünster, 2004] MedWebMünster (2004).
http://medweb.uni-muenster.de/institute/imib/lehre/skripte/biomathe/bio/vertn1.html
(Electronic source).

[Mollenhauer, 2003] Mollenhauer, J. Prof. Dr. (2003). Waldkrankenhaus and University of Jena, Germany (Personal communication).

[RSI] RSI, *IDL-Interactive Data Language.* V5.2, V5.6, Research Systems, Inc., 4990 Pearl East Circle, Boulder, CO 80301, http://www.rsinc.com (Software).

[Scarpelli, 2000] Scarpelli, E. M. (2000). *Opposing views on the alveolar surface, alveolar models, and the role of surfactant.* Journal of Applied Physiology **89**(2): 408-410.

[Walenta] Walenta, A.H. Prof. Dr., University of Siegen, Germany (Personal communication).

3 Synchrotron Radiation for studying multiple scattering properties - beam lines for DEI experiments

In principle, today's optical DEI layout does not differ dramatically from the first experiments of Förster et al. [Förster et al., 1980] who used an X-ray tube, a linear stage for the specimen, an analyser crystal and an X-ray film as detector. A major improvement was the construction of synchrotron radiation (SR) light sources in the last two decades, which established powerful facilities.

The brilliance of higher generation sources opened the opportunity for X-ray experiments which were not possible with conventional X-ray tube sources, even though various further experiments have been already carried out in medical imaging by using X-ray tubes [Ingal et al., 1995], [Davis et al., 1995]. Notable advances in developing competitive lab-type instruments are reported, which also took its lead from recent detector developments. The highly intense X-ray beam available at a SR beam line can reduce the acquisition time for medical imaging by orders of magnitude [Chapman et al., 1997], [Arfelli et al., 1998] at a similar or less dose necessary for X-ray tube imaging. It has to be noted that phase-sensitive imaging techniques developed at SR light sources, and up to now mostly restricted to them, can tremendously decrease the dose necessary to image the specimen with X-ray light [Schneider, 1998]. However, one of the major advantages of SR sources for medical imaging and the DEI technique is their energy tunability.

Synchrotron radiation facilities as well as typical set-ups of SR beam lines with light source, preconditioning optics and end-station are described elsewhere [Wille, 2004], [ELETTRA], [ESRF]. A typical DEI set-up as used for the experimental study of multiple scattering and the verification of the *model for multiple scattering due to refraction* introduced in chapter 2, is shown in Figure 3-1.

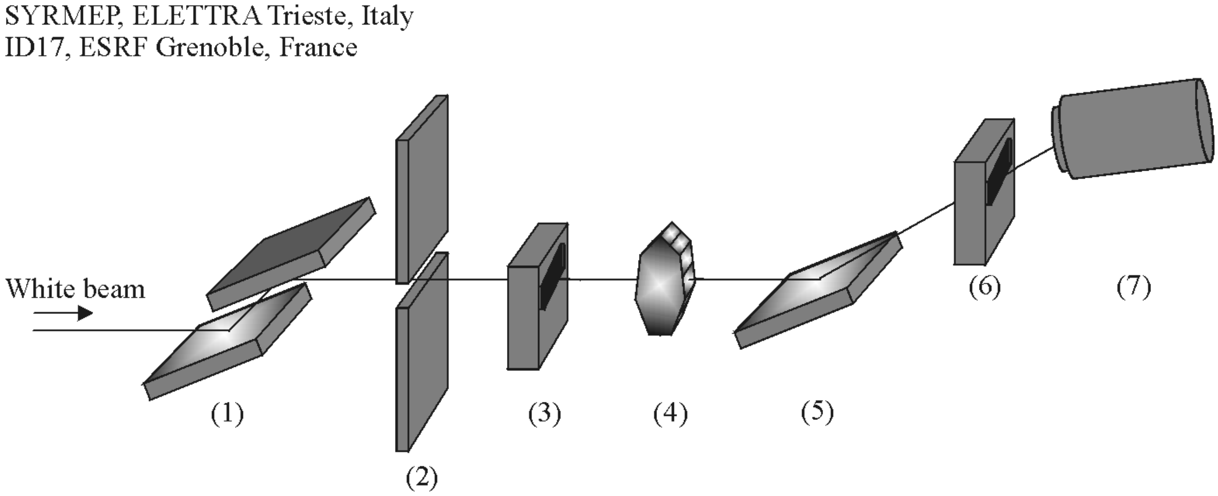

Figure 3-1 Optical scheme of a DEI set-up: The white beam from the synchrotron radiation source is monochromatised by a double crystal monochromator (1), the slit system (2) limits the divergence of the X-ray beam and cuts off undesired light from other pre-conditioning optics. The first ion chamber (3) serves to normalize the intensity incident on the specimen (4). The analyser crystal (5) selects a well-defined range of refractive angles, and their intensity distribution is detected by a second ion chamber (6) and a CCD imaging system (7).

Monochromator: Since the X-ray light emitted from third generation light sources has for many measurements an excessive bandwidth, the so-called “white” or “pink” multi-keV or hard X-ray beam is typically monochromatised. The geometrical characteristics of the crystals are typically calculated by a dynamic theory for thick crystals, or a kinematic approximation for thin crystals [Warren, 1969], or in the simplest case by the Bragg law. The energy resolution of a monochromator is obtained by the differentiating of the Bragg law [Baldelli et al., 2003]. A detailed description of crystal and monochromator properties is given by [Authier, 2001].

Typically a two-crystal set-up or double-crystal set-up is used. Besides practical reasons like fixed position of the exit beam, such a configuration allows higher harmonic rejection of the X-ray beam. The SYRMEP beamline at ELETTRA uses a Bragg-Bragg double crystal configuration, whereas ID17 at the ESRF implements a monochromator in Laue-Bragg as well as Bragg-Bragg configuration.

Slit system: This consists at the medical beam lines described here of a vertical and horizontal slit system made of tungsten and serves mainly to limit the divergence of the radiation, or in other words to reduce the effective souce size in the dispersion plane. Additionally in some cases slit tuning is used to reject higher harmonics as well as stray light from other pre-conditioning optics.

Ion chamber: The ion chambers in front of the specimen and behind the analyser crystal have several functions. For the initial alignment of the experiment they are an indispensable diagnostic. At the beginning of an experimental series, ion chambers are used to record the analyser's Rocking Curve (RC), while during the experiment, they monitor or are used to control the analyser position. The ion chamber in front of the specimen is also used to determine the radiation dose.

Analyser crystal: The analyser crystal could be called "the heart of the DEI technique". The crystal, used in the Bragg case, allows the analysis of the distribution of intensity scattered by the specimen in reciprocal space. A Si crystal is commonly used. Typical angular ranges covered by a Si analyser crystal are in the order of microradian as for instance 19.5 μrad (FWHM, Si(111) @17 keV photon energy) [Schulze, 1993]. Choosing various crystal reflections enables the use of different resolutions and magnifications [Wilkins, 2004]. Various groups have exploited other crystal configurations like the Laue geometry. Bragg set-ups are typically more stable, provide more intense beam and are superior for lower energy imaging in the hard X-ray regime.

Detector: Highly important and crucial instruments of all state-of-the-art experimental stations at third generation light sources are detectors. Specially in medical imaging, the detector has to fulfil a number of demanding requirements: High spatial resolution, a sufficiently large image field (Field of View - FOV) and for low dose imaging, for instance in vivo imaging and imaging of delicate specimens, a DQE (Detective Quantum Efficiency) as high as possible is required. For detector system in the field of medical imaging, a CCD-camera, imaging plate or a linear germanium detector is commonly used.

Two major requirements for the instrumental set-up of a DEI experiment are: (i) Optical stability: Angular oscillations of the analyser in the order of 1-5% of the rocking curve width are necessary, (ii) Short distances between specimen and detector system due to Fresnel diffraction; this might lead to space obstructions for large specimens. Experiments in the frame of this work were carried out at medical beam lines of two European large scale facilities, the SYRMEP beamline at ELETTRA, Trieste, Italy and the ID17 beam line at ESRF, Grenoble, France. These two beam lines are optimised for medical imaging studies at complementary photon energies, and have similar set-ups that allow determination of multiple scattering properties independent of the instrumental set-up. Table 3-1 gives a comparison chart with basic characteristics of both beam lines. This chapter focuses in the following on the description of the experimental set-ups of the two beam lines, experiments themselves as well as specimen are described in chapter 4.

Table 3-1 Basic characteristics of the two medical beam lines used for this work

Characteristic property	SYRMEP, ELETTRA	ID17, ESRF
X-ray source	Bending magnet (exp. Section 6.1)	Symmetrical multipole (21 poles) wiggler
X-ray souce size (horizontal x vertical)	1.1 mm x 0.1 mm (σ)	125 µm x 25 µm (FWHM)
X-ray source divergence (horizontal x vertical)	7.0 x 0.2 mrad^2	3.3 x 0.1 mrad^2
Photon energy range	8 – 35 keV	17 – 80 keV
Monochromator	Si double crystal monochromator here used in Si(111) and Si(333) Bragg reflection	Here used: Si bent Laue crystal in Si(111) Laue-Bragg reflection
Energy resolution ΔE/E	2x10^{-3}	5x10^{-4}
Beam size in object plane (horizontal x vertical)	120 mm x 4 mm	150 mm x 10 mm 300 mm x 10 mm (maximum)
Photon flux in object plane	2x10^8 ph/(mm^2 s) @2 GeV, 300 mA	2x10^{14} ph/s (0.1% bw, 0.1 A, mrad, at B$_{max}$, 33 keV)

3.1 SYRMEP at ELETTRA in Trieste

The SYRMEP (**SY**nchrotron **R**adiation for **M**edical **P**hysics) beam line at Synchrotron Trieste-ELETTRA [ELETTRA] was designed in cooperation with the University of Trieste and INFN for research in medical diagnostic radiology. The light source is a bending magnet, 23 m apart from the experimental stage with a beam divergence about 7 mrad. The double crystal Si monochromator is used in Bragg-Bragg (+,-) mode and delivers an energy range between 8keV and 35keV with a resolution of 2‰. The beam size is 120 x 4 *mm*^{2} and the photon flux (at 23 m, 20 keV, 100 mA, 2.4 GeV) is $2.0 \cdot 10^{8}\, photons / s \cdot mm^{2}$ [SYRMEP@ELETTRA, 2004]. For the DEI set-up of the SYRMEP beamline, a single perfect Si analyser crystal is available. Measurements were acquired using the Si(111) reflection at 17, 25, 30 keV and the Si(333) reflection at 25 keV. Figure 3-2 illustrates the SYRMEP beam line in DEI operation.

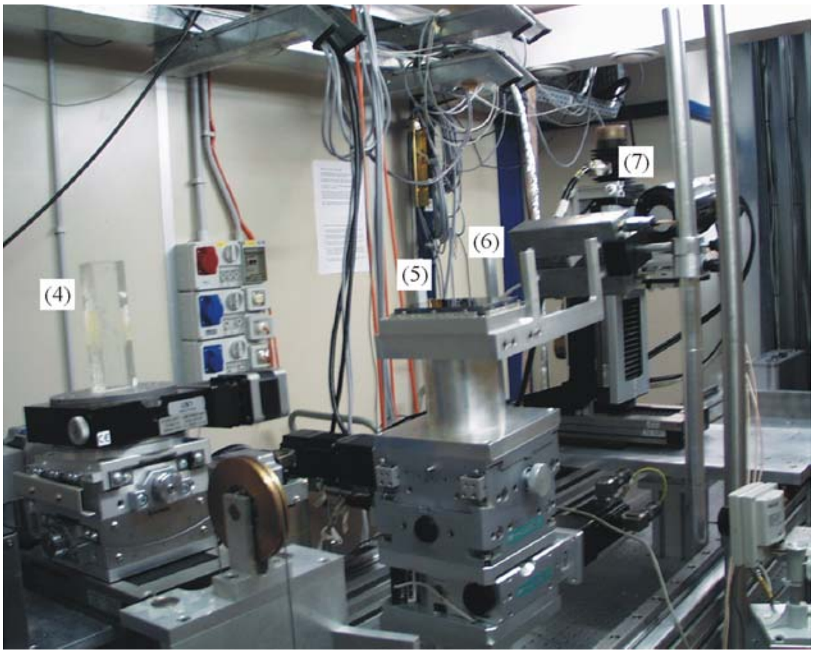

Figure 3-2 SYRMEP beam line ELETTRA/Trieste in DEI operation
(4) Sample stage
(5) Si analyser crystal
(6) Second ion chamber
(7) CCD camera

Different detectors are used for the experiments described in this work:

CCD camera: The CCD camera used is the commercial instrument “Hystar” produced by Photonic Science. The camera is similar to the “Imagestar” type [Photonic_science, 2004], but was slightly modified from 14 to 16 bit dynamic range for use at the SYRMEP BL. The CCD detector offers 2048 x 2048 pixels^2 with a pixel size of 14 x 14 µm^2. For the conversion of the incident X-rays to optical photons scintillator screens of various thicknesses are available: 5, 20 and 40 µm. The thickness of the used scintillator approximately determines the detector spatial resolution. In addition magnifying optics are used, for instance a 3:1 magnifying optic [Menk]. The camera has a field of view of 28.67 x 28.67 mm^2 and its resolution is about 24 lp/mm (10% MTF). Integrated in the SYRMEP BL a typical exposure amounts to 1-140 s and the read out time is about 1 min (full frame and full resolution) [Rigon, 2004].

The exposures of the synthetic specimens described in chapter 4 were recorded using the CCD camera. For the exposure of the absorption images, the specimens were fixed immediately in front of the CCD camera.

The acquired image I_{acq} has to be corrected by the (i) individual camera properties, registered by a so-called flatfield I_{flat} acquired without specimen in the optical sheme, and (ii) the dark current, measured I_{dark} without incident radiation. Hence, the corrected Image I_{corr} can be calculated as:

$$I_{corr} = \frac{I_{acq} - I_{dark}}{I_{flat} - I_{dark}}$$

Imaging plate: The imaging plate system is the IP Fuji BAS 1800 operated with BAS-IP MP 2025 plates, and it offers sampling resolutions of 50 x 50 μm^2, 100 x 100 μm^2 and 200 x 200 μm^2. The field of view amounts to 200 x 250 mm^2. Integrated in the SYRMEP BL the exposure time is between 50 s and 10 min, and the read out time for the full frame and full resolution is about 3 min [Rigon, 2004].

The exposures of the cow lung tissue specimen (sub-section 4.1.3) were recorded with the imaging plate system.

To calculate the image I_{corr} from the aquisition I_{acq} is taken an image column of the background intensity B_0. Each line i of the acquired image is normalised by the background intensity:

$$I_{corr,i} = \frac{I_{acq,i}}{B_0}$$

Further information is reported in [Rigon, 2001], [SYRMEP@INFN, 2004] and [SYRMEP@ELETTRA, 2004].

3.2 ID17 at ESRF in Grenoble

The biomedical beam line ID17 of the European Synchrotron Radiation Facility [ESRF] at Grenoble was designed for imaging diagnoses and irradiation therapy. The light source is a wiggler approximately 140 m from the experimental station. The Si monochromator crystals used in Laue-Bragg (+,-) mode is optimised for a photon energy range of 17 keV to 80 keV. The photon source divergence is 3.3 x 0.1 mrad^2 (HxV, FWHM @B$_{max}$, 33 keV), the maximum beam size at the specimen is 300 x 10 mm^2 (HxV, aperture limited) and the expected flux 2.10^{14} ph/s (0.1% bw, 0.1 A, mrad, at B$_{max}$, 33 keV, unfiltered). [ID17@ESRF, 2004]. Besides various other BL modes, a DEI set-up consisting of a quasi perfect Si analyser crystal is available and used for the experiments described in this work. Measurements were acquired with Si(111) at 25, 40 and 60 keV. Figure 3-3 illustrates the biomedical beam line ID17 in DEI operation.

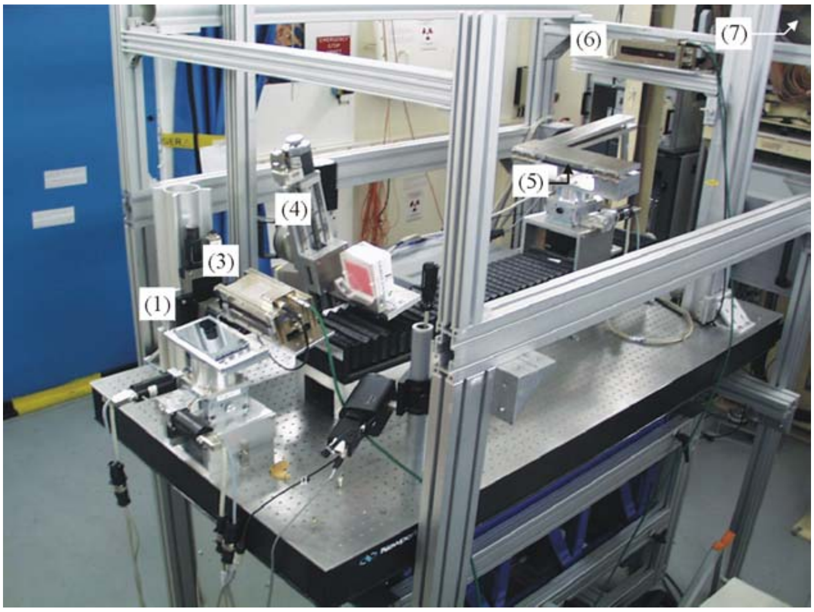

Figure 3-3 Biomedical beam line ID17 ESRF/Grenoble in DEI operation
(1) Monochromator
(3) First ion-chamber
(4) Sample stage
(5) Analyser crystal
(6) Second ion chamber
(7) FRELON camera

The taper optics CCD "FRELON" camera: The image recording system is an ESRF in-house developed taper optics 50 micron FRELON (**F**ast **RE**adout **LO**w **N**oise) camera. The active input surface of 94 x 94 mm^2 (the field of view-FOV) converts the X-rays by a standard mammographic phosphor screen to visible light. By tapered fiber optics it is guided onto the CCD array of 2048 x 2048 pixels^2. A resolution of 47 μm in the horizontal and vertical directions is achieved. The camera resolution is about 9 lp/mm at 10% MTF (Modulation Transfer Function) [Bravin et al., 2003].

The measurements taken with Si(111) reflection at 25, 40 and 60 keV were recorded with the FRELON camera.

To correct the image, I_{corr} is calculated by taking into account the individual camera properties presented by a normalisation line N_0. The correction is performed to each line of the acquired image I_{acq}:

$$I_{corr,i} = \frac{I_{acq,i}}{N_0}$$

References

[Arfelli et al., 1998] Arfelli, F., M. Assante, V. Bonvicini, A. Bravin, G. Cantatore, E. Castelli, L. Dalla Palma, M. Di Michiel, R. Longo, A. Olivo, S. Pani, D. Pontoni, P. Poropat, M. Prest, A. Rashevsky, G. Tromba, A. Vacchi, E. Vallazza and F. Zanconati (1998). *Low-dose phase contrast x-ray medical imaging.* Physics in Medicine and Biology **43**(10): 2845-2852.

[Authier, 2001] Authier, A. (2001). *Dynamical theory of x-ray diffraction.* Oxford University Press.

[Baldelli et al., 2003] Baldelli, P., A. Taibi, A. Tuffanelli and M. Gambaccini (2003). *Quasi-monochromatic x-rays for diagnostic radiology.* Physics in Medicine and Biology **48**(22): 3653-3665.

[Bravin et al., 2003] Bravin, A., S. Fiedler, P. Coan, J. C. Labiche, C. Ponchut, A. Peterzol and W. Thomlinson (2003). *Comparison between a position sensitive germanium detector and a taper optics CCD "FRELON" camera for diffraction enhanced imaging.* Nuclear Instruments & Methods in Physics Research Section a-Accelerators Spectrometers Detectors and Associated Equipment **510**(1-2): 35-40.

[Chapman et al., 1997] Chapman, D., W. Thomlinson, R. E. Johnston, D. Washburn, E. Pisano, N. Gmur, Z. Zhong, R. Menk, F. Arfelli and D. Sayers (1997). *Diffraction enhanced x-ray imaging.* Physics in Medicine and Biology **42**(11): 2015-2025.

[Davis et al., 1995] Davis, T. J., D. Gao, T. E. Gureyev, A. W. Stevenson and S. W. Wilkins (1995). *Phase-Contrast Imaging of Weakly Absorbing Materials Using Hard X-Rays.* Nature **373**(6515): 595-598.

[ELETTRA] ELETTRA http://www.elettra.trieste.it (Electronic source).

[ESRF] ESRF http://www.esrf.fr (Electronic source).

[Förster et al., 1980] Förster, E., K. Goetz and P. Zaumseil (1980). *Double Crystal Diffractometry for the Characterization of Targets for Laser Fusion Experiments.* Kristall und Technik **15**(8): 937-945.

[ID17@ESRF, 2004] ID17@ESRF (2004). http://www.esrf.fr/UsersAndScience/Experiments/Imaging/ID17/ (Electronic source).

[Ingal et al., 1995] Ingal, V. N. and E. A. Beliaevskaya (1995). *X-Ray Plane-Wave Topography Observation of the Phase-Contrast from a Noncrystalline Object.* Journal of Physics D-Applied Physics **28**(11): 2314-2317.

[Menk] Menk, R.-H. ELETTRA, Sincrotrone Trieste, Italy (Personal communication).

[Photonic_science, 2004] Photonic_science (2004). http://www.photonic-science.co.uk/zzt_XImagestar.html (Electronic source).

[Rigon, 2001] Rigon, L. (2001). *Nuove modalità per la produzione di immagini digitali con luce die sincrotrone mediante cristallo analizzatore doctoral thesis.* University of Trieste.

[Rigon, 2004] Rigon, L. (2004). University of Trieste, Department of Physics (Personal communication).

[Schneider, 1998] Schneider, G. (1998). *Cryo X-ray microscopy with high spatial resolution in amplitude and phase contrast.* Ultramicroscopy **75**(2): 85-104.

[Schulze, 1993] Schulze, C. (1993). *PEPO*, IDL Program, ESRF, Medical Imaging Group, (Software).

[SYRMEP@ELETTRA, 2004] SYRMEP@ELETTRA (2004).
http://www.elettra.trieste.it/experiments/beamlines/syrmep/index.html (Electronic source).

[SYRMEP@INFN, 2004] SYRMEP@INFN (2004).
http://www.ts.infn.it/experiments/syrma/ (Electronic source).

[Warren, 1969] Warren, E. (1969). *Xray diffraction.* Addison-Wesley Publishing Company Inc. Reasing, Mass.

[Wilkins, 2004] Wilkins, S. W. (2004). *Emerging Opportunities for Biomedical Phase-Contrast Imaging using SR.* MASR, Trieste.

[Wille, 2004] Wille, K. (2004). *Einführung in die Beschleunigerphysik.*
http://www.delta.uni-dortmund.de/scripts/BP/ (Electronic source).

4 Simulating nature: Experiments on multi-scattering random distributions and structures

A DEI experiment with a nitrogen cooled cow lung tissue specimen demonstrated multiple scattering properties of lung tissue and is described in sub-section 4.1.3. The detection of multiple scattering properties motivated the fabrication of synthetic specimens to simulate the properties of lung tissue. Synthetic specimens are simpler to handle and allow the modelling of the idea of multiple scattering. A PMMA sphere is used to model single scattering of an alveolus. The aims of fabricating synthetic specimen are: (i) to study multiple scattering properties in general (ii) to verify the *model for multiple scattering due to refraction* introduced in chapter 2, (iii) to verify the applicability of the model to lung tissue. Two types of synthetic specimens were fabricated, specimens with randomly distributed scattering particles and specimens with scattering microstructures. The specimen design and experiments with scattering of randomly distributed particles are introduced in section 4.1. Design and fabrication of the specimens with periodical substructures and experiments are described in section 4.2. The data analysis of the experiments described in this chapter is presented in chapter 5.

4.1 Multiple scattering experiments with randomly distributed microparticles

Two types of random scattering specimens are introduced in this section. (i) Sub-section 4.1.1 describes the design and fabrication of the synthetic specimens, and experiments in sub-section 4.1.2. (ii) The preparation of a cow lung tissue specimen and the experiment are reported in sub-section 4.1.3.

4.1.1 Synthetic specimens to generate variable multiple scattering power

Three stepped profile PMMA containers were fabricated and filled with PMMA micro spheres of different diameters and varying multiple scattering properties. The profile of the PMMA container is presented in Figure 4-1 (left). The containers were filled with micro spheres of 100 µm, 30 µm and 6 µm in diameter in order to generate different multiple scattering powers. The containers filled with spheres are shown in Figure 4-1 (right).

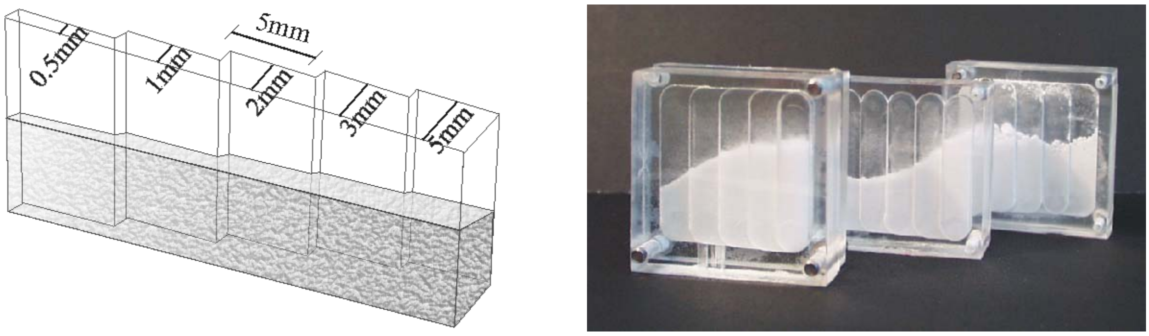

Figure 4-1 Design of micro sphere specimens:

Left: 3D scheme of the profile of the stepped PMMA containers and thickness of each scattering layer.

Right: Multiple scattering specimens: PMMA spheres of a well-defined size of 100 µm, 30 µm and 6 µm in diameter (left to right), arranged in a stepped profiled PMMA container to form various thickness as shown in the profile on the left.

To generate a well-known refraction signal for the experiments, another specimen was fabricated by PMMA, containing alternating planes and zones inclined by 45°. This specimen is denoted as trapezoidal. Figure 4-2 illustrates the trapezoidal profile and shows an image of the trapezoid.

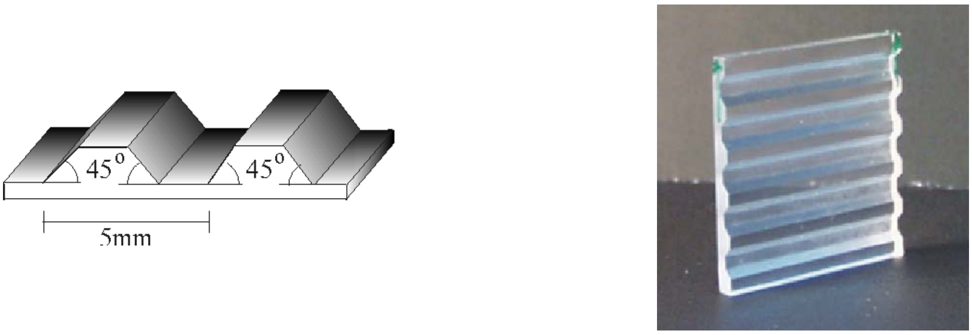

Figure 4-2 The trapezoidal specimen.

Left: Scheme of the profile of the PMMA specimen with alternating inclined zones, the trapezoid.

Right: Trapezoidal specimen with single refraction properties, fabricated of PMMA, containing alternating planes and zones inclined by 45°.

4.1.2 Experiments with randomly distributed scattering particles using synthetic specimens

Multiple scattering experiments are performed using the PMMA micro sphere specimens described in the previous section separately or in combination with the trapezoidal specimen. A typical DEI set-up is used for the experiments shown in Figure 3-1. The DEI set-up is used in the usual mode with the analyser crystal at certain reflection position or at a fixed angular position.

In addition, the DEI set-up is used rotating the analyser crystal continuously during the exposure. In this case, the detector scans the whole angular density distribution of the scattered light. Assuming that the angular distribution is determined by the reflectivity of the analyser crystal and the scattering power of the specimen, the measurement gives information about the multiple scattering power of the specimen. Measurements using the micro sphere specimens are separately acquired at 17 keV, 25 keV and 30 keV photon energy, using the Si analyser crystal in the (111) reflection mode and additionally using the analyser crystal in (333) reflection mode at 25 keV photon energy. A commercially produced 2048 x 2048 pixel CCD camera (chapter 3, [Photonic_science, 2004]) with a resolution of 14 μm was used for recording the images. The measurements were carried out in April 2002 at the SYRMEP beam line at ELETTRA. Figure 4-3 shows the exposure of a typical angular distribution of the scattered X-ray light.

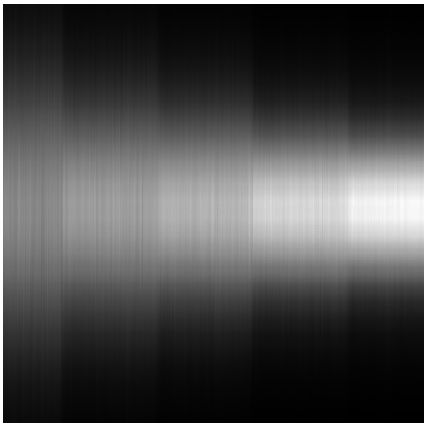

Figure 4-3 Exposure of 100 µm spheres @17 keV, SYRMEP ELETTRA Trieste in 04/2002. From left to right: 3 mm-sector, 2 mm-sector, 1 mm-sector, 0.5 mm-sector, air

The multiple scattering power is quantitatively determined at 17 keV, 25 keV and 30 keV photon energies for the various thicknesses of the micro sphere specimens from these measurements. In addition, the square-root dependence of the specimen thickness on multiple scattering power for randomly distributed scattering particles is verified. The data analysis of these measurements is presented in section 5.1.

The DEI experiments are performed using the analyser crystal in a fixed analyser reflectivity position of 10%, 50% and maximum reflectivity. Using the micro sphere specimens separately and in combination with the trapezoid, measurements were taken at 17 keV, 25 keV and 30 keV photon energy in April 2002 at the SYRMEP beam line at ELETTRA and at 25 keV, 40 keV and 60 keV photon energy at ID17/ESRF in April and August 2003. For each specimen and energy, an absorption or bright-field image was also acquired, which is an exposure similar to conventional X-ray tube imaging.

The images were recorded at the SYRMEP beam line with the “Hystar Photonic Science” CCD camera (chapter 3, [Photonic_science, 2004]) with a resolution of 14 µm. At ID17 of the ESRF images were acquired using the in-house developed 50-micron FRELON camera [Bravin et al., 2003] with a special resolution of 47 µm (see also chapter 3).

Figure 4-4 presents a selection of some typical exposures. The measurements are analysed in chapter 5.

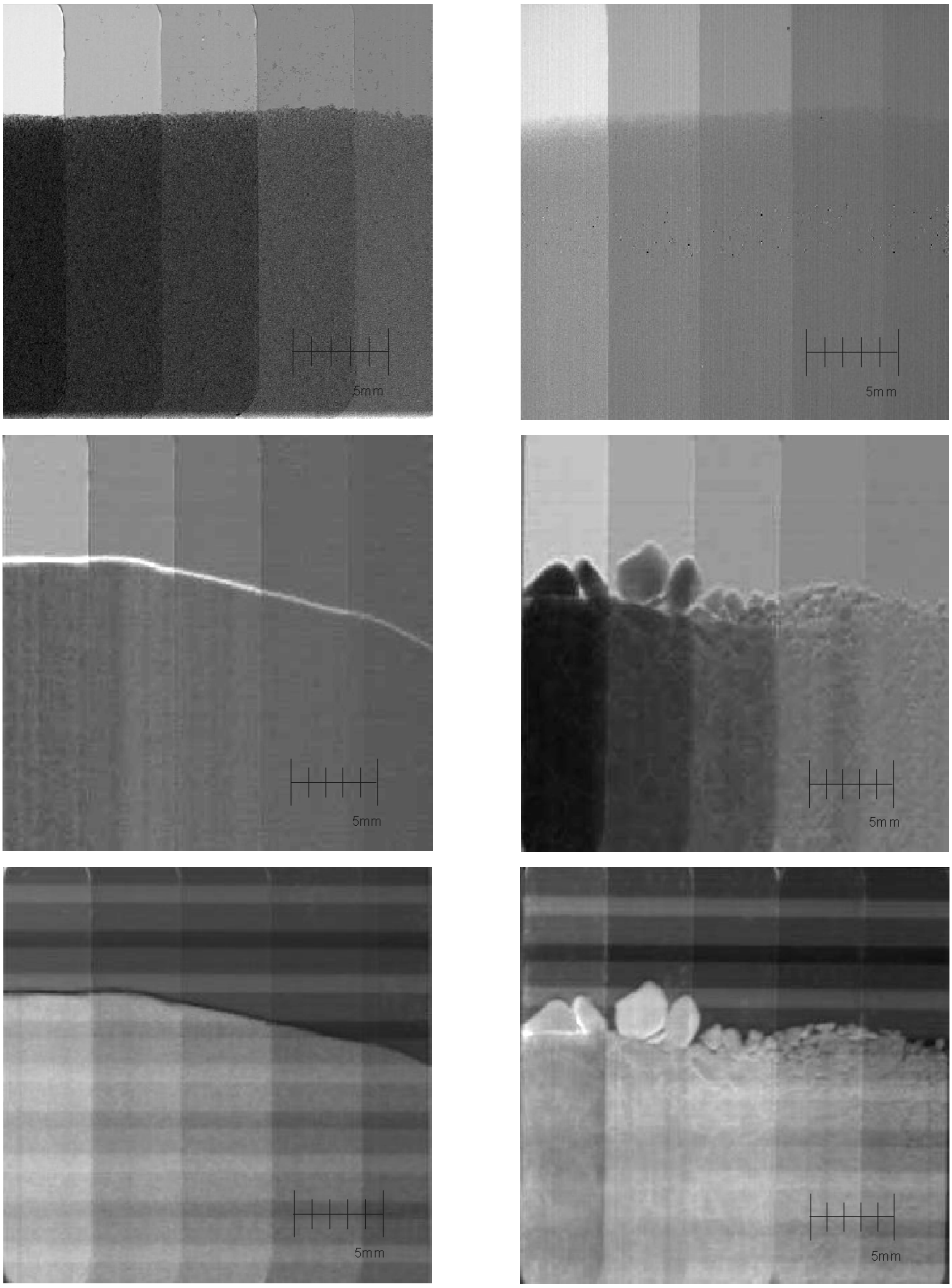

Figure 4-4 X-ray exposures of PMMA sphere specimens. From left to right of each image: 5 mm, 3 mm, 2 mm, 1 mm, 0.5 mm thickness of the scattering layer.

Upper: DEI image (left), analyser maximum reflectivity, and Absorption image (right) of 100 µm spheres, 17 keV (SYRMEP/ELETTRA 04/2002).

Middle: DEI image 100 µm spheres (left), and 6 µm spheres (right), analyser reflectivity 50%, 25 keV.

Lower: DEI image 100 µm spheres (left), and 6 µm spheres (right) each with trapezoid, reflectivity 10%, 25 keV. (Middle and Lower: ID17/ESRF 04/2003)

4.1.3 Experiments performed with soft tissue: Exposures of a cow lung specimen

This chapter describes a DEI experiment with a nitrogen cooled cow lung specimen, which was made in 2001 at the SYRMEP beam line of ELETTRA. The specimen demonstrates significant signals resulting from the multiple scattering properties of the lung tissue. Details of the analysis of the experiment are described in sub-section 5.1.5.

The alveoli of lung tissue are assumed to have multiple scattering properties. For conserving and fixing the structure of the alveoli of a cow lung tissue specimen, the specimen was prepared by nitrogen cooling immediately after the death of the cow, and a lung tissue specimen about 12 mm thick was extracted. The specimen prepared in this manner was always kept nitrogen cooled, during transport as well as during the measurement. In the frame of an experiment in May 2001 at the SYRMEP beam line of ELETTRA, DEI exposures of the specimen were acquired with 10%, 50% and maximum reflectivity of the analyser in Si(333) reflection at 25 keV photon energy. The images were acquired using an imaging plate. Figure 4-5 shows the scattering property of lung tissue with the analyser crystal set to 10% reflectivity.

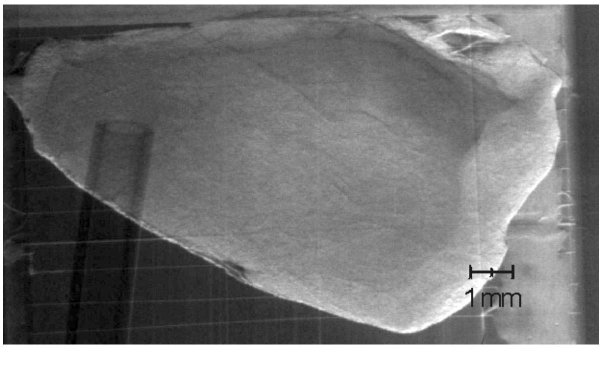

Figure 4-5 X-ray image of a cow lung tissue specimen, approximately 12 mm thick, acquired in 10% analyser reflectivity mode at 25 keV photon energy (SYRMEP/ELETTRA, 05/2001, image post-processed).

Different brightness in various regions of interest sectors indicates different scattering power.

On the left side, the tube for nitrogen cooling the tissue specimen is visible.

4.2 Experiments with multi-scattering micro structured particles

In this section, the fabrication of and experiments with specimens having a well-defined substructure is described. Sub-section 4.2.1 focuses on the specimen design and fabrication of PMMA specimens by X-ray lithography. DEI experiments with these specimens are described in sub-section 4.2.2.

4.2.1 Lithography specimens

X-ray lithography is a powerful instrument for fabricating precise microstructures. A step-like iron mask was fabricated by the University of Siegen using a special laser cutting technology [Gebauer], the negative mask was used to form the specimen shapes; its design is shown in Figure 4-6. To include additionally a structure in the form of cylindrical pinholes, a “Himesh 155” wire screen mask was used [DEPH@University of Siegen, 2004]. Combining both masks, various 2 mm thick PMMA specimens are fabricated at the Deep Etch Lithography beam line of ELETTRA [DXRL@ELETTRA]. Two types were fabricated with different orientation of the holes with respect to the surface as depicted in Figure 4-6. Specimen names used in this work follow the name of the lithography process: The lithography specimen, where the whole configuration is rotated by 30 degrees with respective to the surface as shown in Figure 4-6 (left) is called “Lit_05”, the pinhole configuration of “Lit_16” is oriented orthogonally with respect to the surface (see Figure 4-6, right).

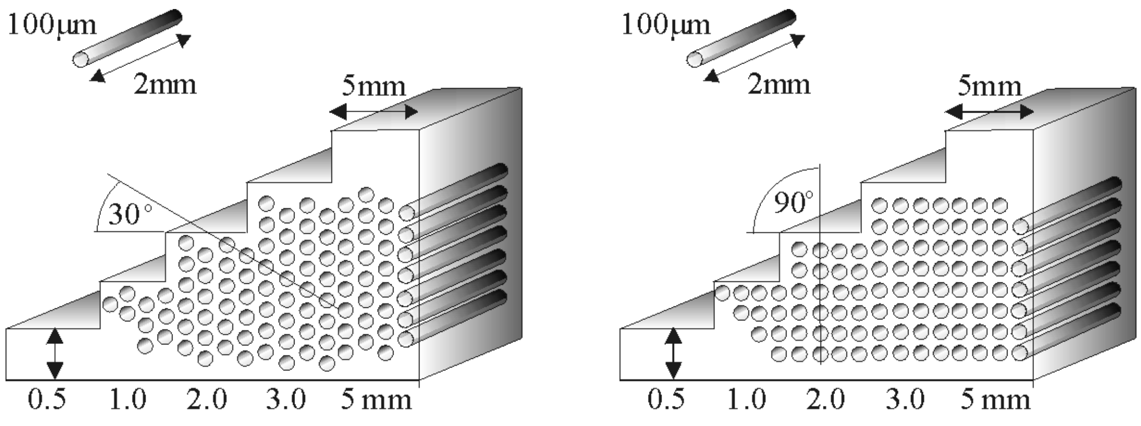

lit_05 lit_16

Figure 4-6 Scheme of construction of the lithography specimens.

Figure 4-7 shows a photograph of the fabricated lithography specimens.

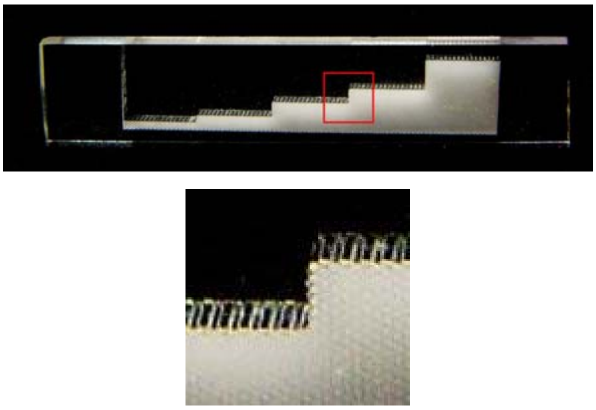

Figure 4-7 Photograph of the lithography specimen "Lit_16".

In the magnification of the red marked sector the pinhole structure is visible.

A visible light micrograph of the specimens is shown in Figure 4-8.

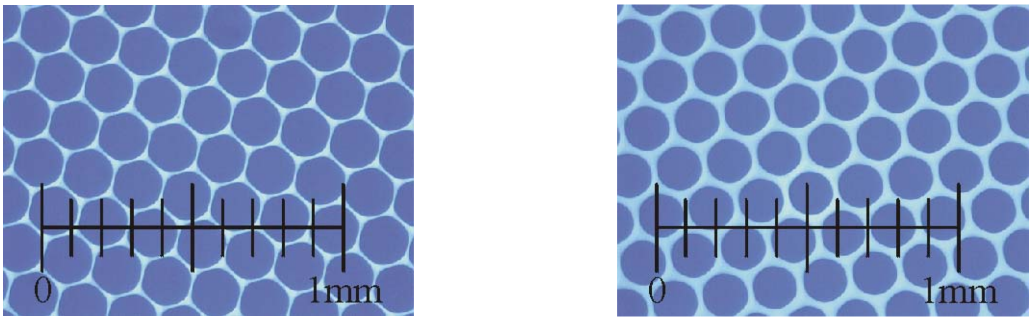

Figure 4-8 Micrograph of lithography specimen surfaces

Left: Micrograph of top surface

Right: Micrograph of bottom surface

As can be seen from Figure 4-8, the cylinders in the lithography specimens are slightly conically deformed. The hole diameter at the top surface, which is oriented towards the beam during the lithography exposure, is larger than the hole diameter at the bottom surface of the specimen due to the lithography fabrication process [Perennes].

4.2.2 Experiments with microstructures

To study the influence of scattering by periodic structures, different measurements were made with the lithography specimens “Lit_05” and “Lit_16” at 17 keV and 25 keV photon energy (SYRMEP, ELETTRA), and at 25 keV, 40 keV and 60 keV photon energy (ID17, ESRF). Images were acquired using the DEI set-up with fixed analyser reflectivity positions of 10%, 50% and maximum reflectivity. To simulate various structural configurations, the specimen was rotated by 0.5 degree steps for each DEI series (Figure 4-9). Images of each specimen were acquired in an angular range of –5.0 to 5.0 and 27.0 to 33.0 degrees.

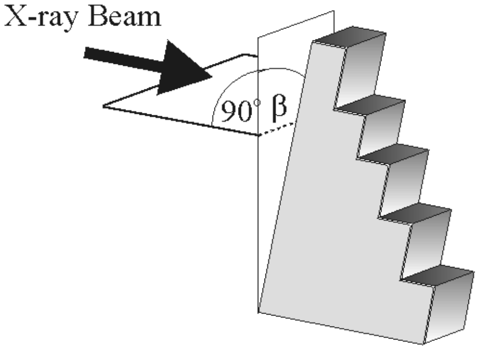

Figure 4-9 Alignment of lithography specimens For each DEI series (analyser reflectivity positions 10, 50%, maximum) the lithography specimen was rotated in 0.5 degree-steps (β).

The images acquired at ID17 of the ESRF have a spatial resolution of 47 μm [Bravin et al., 2003]. At the SYRMEP beam line of ELETTRA, the images were acquired with a resolution of about 14 μm. Figure 4-10 shows some representative images.

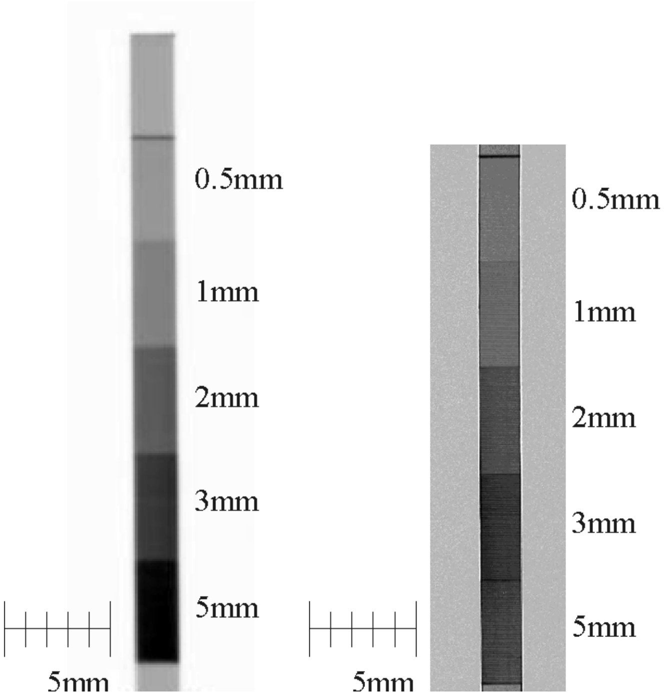

Figure 4-10 X-ray images of the specimen “Lit_05” @25 keV photon energy acquired in maximum analyser reflectivity mode.

Left: The lithography specimen is rotated by 0° respectively the incident X-ray plane (ID17/ESRF, 04/2003, image post processed).

Right: The lithography specimen is rotated by β=2° (SYRMEP/ELETTRA, 10/2003, image post processed).

References

[Bravin et al., 2003] Bravin, A., S. Fiedler, P. Coan, J. C. Labiche, C. Ponchut, A. Peterzol and W. Thomlinson (2003). *Comparison between a position sensitive germanium detector and a taper optics CCD "FRELON" camera for diffraction enhanced imaging.* Nuclear Instruments & Methods in Physics Research Section a-Accelerators Spectrometers Detectors and Associated Equipment **510**(1-2): 35-40.

[DEPH@University of Siegen, 2004] Detectorphysics, University of Siegen (2004). http://deph.physik.uni-siegen.de/2d/index.html (Electronic source).

[Gebauer] Gebauer, D. Departement of Physics, University of Siegen, Germany (Personal communication).

[DXRL@ELETTRA] Deep Etch Lithography BL, ELETTRA, Trieste, Italy http://www.elettra.trieste.it/experiments/beamlines/dxrl/index.html (Electronic source).

[Perennes] Perennes, F. ELETTRA, Sincrotrone Trieste, Italy (Personal communication).

[Photonic_science, 2004] Photonic_science (2004).
http://www.photonic-science.co.uk/zzt_XImagestar.html (Electronic source).

5 Analysis of multiple scattering properties

Multiple scattering caused by randomly distributed scattering microparticles and structures is studied. The calculation of the multiple scattering power by using the single scattering power of a microparticle (Equation 2-18) is verified.

Random distribution scattering is investigated by experiments with synthetic specimens of PMMA simulating various multiple scattering powers as well as with cow lung tissue specimen in section 5.1. Some basic properties of multiple scattering are identified and the calculation of multiple scattering power by using the single scattering power is verified by experiments with synthetic specimens. The multiple scattering power of a cow lung tissue specimen is experimentally determined and partial deflation of the lung tissue specimen during the preparation has to be included in the calculation of multiple scattering power. A definitive comparison of the calculated scattering power of lung tissue using the single scattering power of an alveolus was possible by Monte-Carlo simulations for a mouse lung image from the Australian DEI group, which is in good agreement.

The analyser crystal acts as an angular filter using the DEI technique. Thus, strong multiple scattering power as for instance predicted for lung tissue might limit the DEI technique. Thus the analyser crystal influence on a scattering signal is investigated in section 5.2 and an outlook for using the DEI technique as a method for a new generation of lung radiography is discussed.

Finally, the influence of scattering microparticles with a well-defined substructure is investigated in section 5.3. The same number of scattering microparticles with various arrangements is studied and a further qualitative verification of the model for scattering is achieved. A strong influence of substructures on the total scattering power can be derived from calculations and the feasibility of DEI as a method for detecting microstructures is discussed.

Data analysis in this chapter was made using IDL [RSI] and routines programmed by myself.

5.1 Properties of random distribution scattering

The scattering power of synthetic specimens is determined in sub-section 5.1.1. Subsections 5.1.2 and 5.1.3 consider basic multiple scattering properties: (i) the dependence of total scattering power on thickness of the scattering layer and (ii) the photon energy. Thus the model of multiple scattering and the calculation of the single scattering powers introduced in chapter 2 can experimentally be verified. Sub-section 5.1.4 applies the calculation of the multiple scattering power by using the single scattering power to synthetic specimens. Comparison with experimental data delivers good agreement of the values calculated with the single scattering power and using the Central Limit Theorem. Furthermore, multiple scattering of soft tissue is investigated. Sub-section 5.1.5 determines the total scattering power of a cow lung tissue performed in a DEI experiment. Uncertainties in specimen preparation as partial deflation of the lung tissue during preparation are included and allow predictions by including the single scattering power of an alveolus as described in sub-section 5.1.6. A further application of calculating the multiple scattering power of soft tissue by using the single scattering power of a single alveolus is demonstrated in sub-section 5.1.7.

5.1.1 Determination of the total scattering power for synthetic PMMA sphere specimens

Data analysis in this section refers to the specimens and experiments described in sub-sections 4.1.1 and 4.1.2 Step profiled PMMA containers with different thicknesses are filled with micro spheres of different diameter in order to generate various scattering powers. The angular density distribution of scattered quasi monoenergetic X-ray photons are scanned directly by continously rotating the analyser crystal during the exposure. Figure 5-1 (upper right) presents a typical exposure of the directly scanned distribution of scattering angles as well as the angular intensity distribution for the different scattering thicknesses of the specimens.

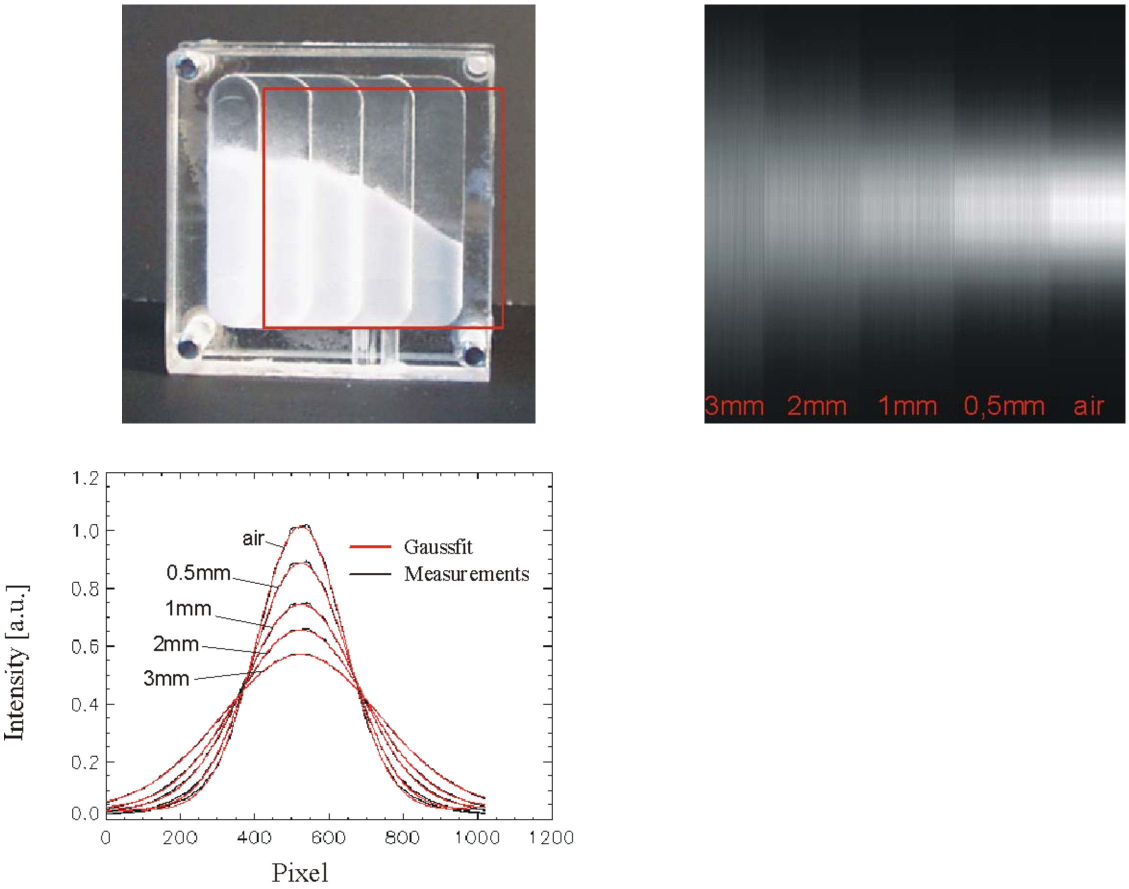

Figure 5-1 Direct scan of angular distribution of X-rays scattered by the synthetic specimen 100 µm PMMA spheres, 17 keV photon energy.

Upper left: Photo of the PMMA micro sphere specimen.

Upper right: X-ray image of the direct scan of the angular X-ray distribution for the 100 µm sphere specimen (left) acquired @17 keV photon energy during the SYRMEP ELETTRA beam time in 04/2002. The image is post-processed. The scan is correlated to the region of interest signed on the left. From left to right: 3 mm-sector, 2 mm-sector, 1 mm-sector, 0.5 mm-sector.

Lower left: Angular intensity distribution of scattered X-rays versus the scattering thickness of the specimen (black). The distribution illustrates clearly the enlargement of the analyser rocking curve (relative to the measurement in air) due to scattering. The normalised mean intensity of each sector of the exposure shown in the upper right for calculating the histogram. And Gauss-fit to the plot of measured angular density distribution (red). The Gauss-fit demonstrates good agreement with the Gaussian shape.

Two major statements result from Figure 5-1: (i) The presence of additional scattering enlarges the distribution of scattering angles $\Delta\theta$, which is superimposed on the scattering by the analyser crystal (the analyser rocking curve). (ii) The distribution of scattering angles $\Delta\theta$ is a Gaussian-type shape both with and without additional scattering.

Thus the measured Gaussian sigma $\sigma_{measurement}$ is determined by forming the sum in quadrature of the Gaussian sigma of the analyser rocking curve σ_{RC} and total scattering power of the specimen defined as the specimen's Gaussian sigma $\sigma_{specimen}$ (Equation 5-1).

$$\sigma^2_{measurement} = \sigma^2_{RC} + \sigma^2_{specimen} \qquad \textbf{Equation 5-1}$$

Analysis of Figure 5-1 delivers $\sigma_{measurement}$ in dimensions of pixel. Several corrections, as for instance taking into account various exposure times and specimen scanning velocities, to the raw data were done in order to translate the "pixel range" for each graph to the scanned angular range before calculating $\sigma_{specimen}$ using Equation 5-1. The resulting total scattering power $\sigma_{specimen}$ acquired at various photon energies for all three specimens and thicknesses are illustrated in Figure 5-2.

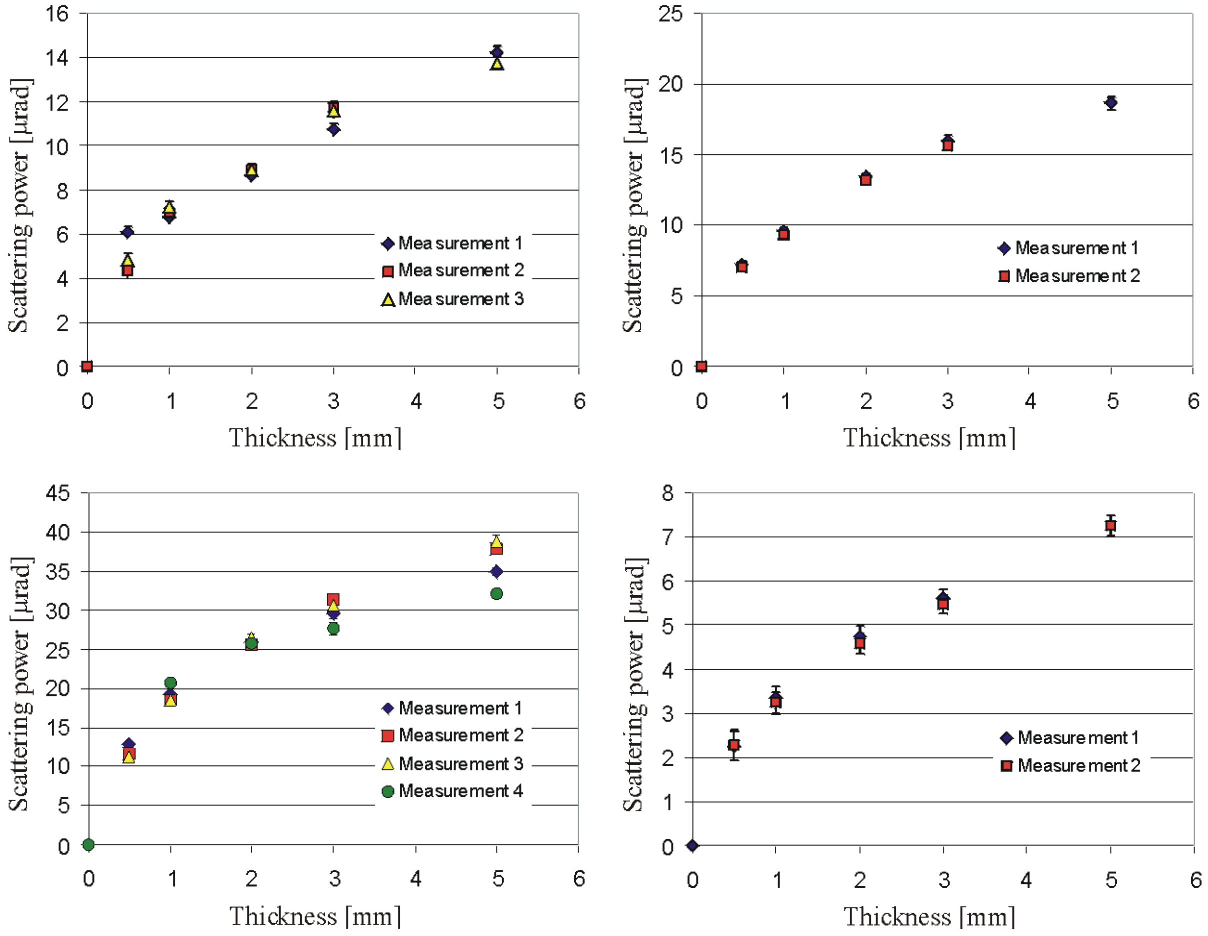

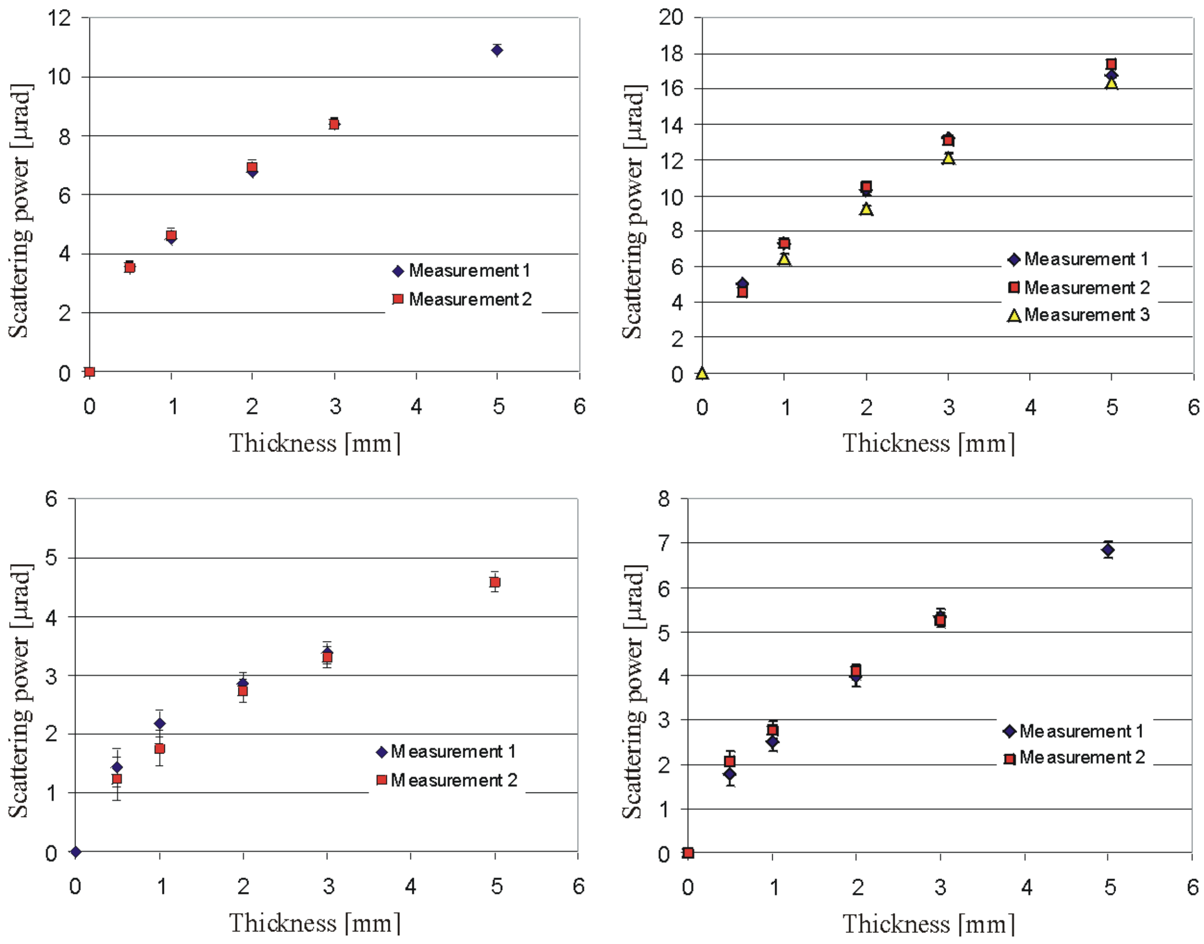

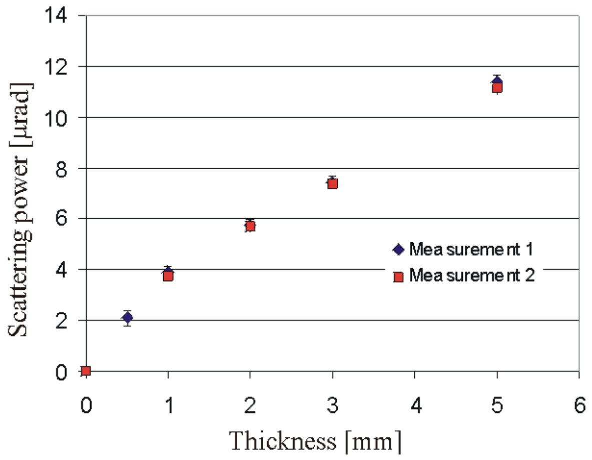

Figure 5-2 Determined total scattering power for independent measurements under equal conditions of 100 µm, 30 µm and 6 µm spheres @17 keV, 25 keV and 30 keV photon energy (SYRMEP/ELETTRA run 04/2002).

Experimental results @17 keV photon energy in the upper left for 100 µm spheres, upper right 30 µm and second left 6 µm spheres. 25 keV photon energy in the second right for 100 µm spheres, third left 30 µm and third right 6 µm spheres.

And the experimental results for the acquisitions at 30 keV photon energy in the fourth left for 100 µm spheres, fourth right 30 µm and lower left 6 µm spheres.

(i) The multiple scattering power increases with increasing thickness of scattering material whereas it decreases at higher photon energies and fixed thickness of scattering material. (ii) Multiple scattering power at fixed thickness of scattering material decreases with increasing photon energy. (iii) Multiple scattering power increases with the number of scattering microparticles at fixed photon energy.

These total scattering power values of the synthetic specimens are of importance in terms of: (i) In sub-sections 5.1.2 and 5.1.3 the values are used to indicate some basic properties of scattering. The values serve in sub-section 5.1.4 for verification of the calculation of multiple scattering power by using the single scattering power and the Central Limit Theorem (Equation 2-18). (ii) Furthermore they are used in sub-sections 5.2.2 and 5.2.4 for simulating some effects caused by scattering and demonstrating the importance of the total scattering power for designing DEI experiments and finding limitations of the DEI technique. (iii) Also the experimental part of Rigon's approach [Rigon et al., 2003] to extend the Chapman algorithm [Chapman et al., 1997] by a second order approximation including ultra small angle scattering is based on the values determined in this work.

5.1.2 Square-root dependence of multiple scattering power on thickness

If the X-ray interaction with each single scattering particle can be assumed to be independent, the square-root dependence of multiple scattering power on the mean number *N* of scattering particles is derived from the principles of multiple scattering (section 2.4). Thus the multiple scattering power of a specimen σ_{specimen} is identified by the scattering power σ_{particle} composing the specimen and the Central Limit Theorem (Equation 2-18). For specimens with homogeneous material density is the mean number *N* of scattering particles directly linked to the specimen thickness *d*. Hence is expected a square-root dependence of multiple scattering power σ_{specimen} on the specimen thickness *d*:

$$\sigma_{specimen} \propto \sqrt{d} \cdot \sigma_{particle} \qquad \textbf{Equation 5-2}$$

Plotting the square of σ_{specimen} determined from the experiments with the PMMA sphere specimens (see sub-section 5.1.1) versus the thickness of scattering material, the expected square root thickness dependence is proven. Figure 5-3 presents some of the linear fits to the square of the experimentally determined $\sigma^2_{\text{specimen}}$. A χ^2 test to the linear fit of all measurements demonstrate an agreement within a confidence level of *P=0.998* [Brandt, 1999].

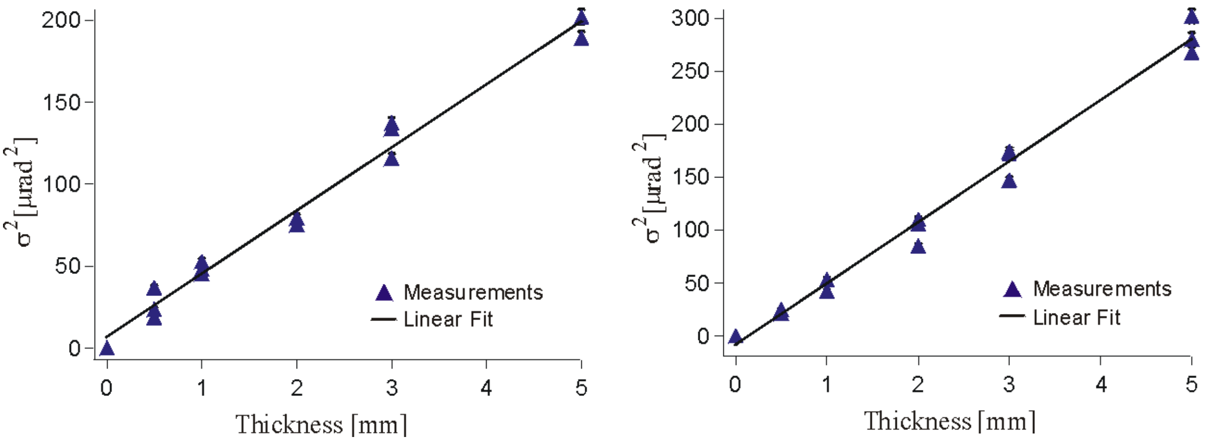

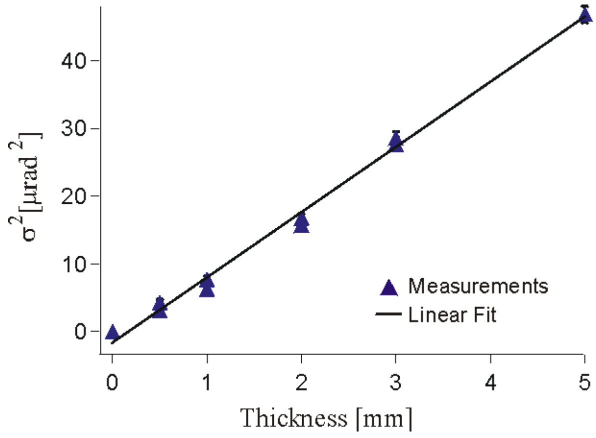

Figure 5-3 Linear fits of the experimentally determined $\sigma^2_{specimen}$ versus the thickness of scattering material (selection of various PMMA micro sphere specimens 100 µm, 30 µm and 6 µm at 17 keV, 25 keV and 30 keV photon energy, data acquired during run SYRMEP/ELETTRA Trieste, 04/2002).

Upper left: 100 µm spheres @17 keV photon energy, upper right: 6 µm spheres @25 keV photon energy and lower left: 30 µm spheres @30 keV photon energy.

Table 5-1 Results of the linear fit of $\sigma^2_{specimen}$ versus thickness of scattering material

Measurement	Degrees of freedom	χ^2	Quantile $\chi^2_{P=0.998}$ [Bronstein et al., 1987]	Result
100 µm spheres @17 keV	14	41.9	34.0	$\chi^2 > Q(\chi^2_{P=0.998})$
30 µm spheres @17 keV	9	14.2	26.1	$\chi^2 < Q(\chi^2_{P=0.998})$
6 µm spheres @17 keV	19	39.4	41.6	$\chi^2 < Q(\chi^2_{P=0.998})$
100 µm spheres @25 keV	9	16.3	26.1	$\chi^2 < Q(\chi^2_{P=0.998})$
30 µm spheres @25 keV	9	25.8	26.1	$\chi^2 < Q(\chi^2_{P=0.998})$
6 µm spheres @25 keV	14	32.7	34.0	$\chi^2 < Q(\chi^2_{P=0.998})$
100 µm spheres @30 keV	9	17.0	26.1	$\chi^2 < Q(\chi^2_{P=0.998})$
30 µm spheres @30 keV	9	22.8	26.1	$\chi^2 < Q(\chi^2_{P=0.998})$
6 µm spheres @30 keV	9	16.0	26.1	$\chi^2 < Q(\chi^2_{P=0.998})$

The linear fits of $\sigma^2_{specimen}$ versus thickness of scattering material in Table 5-1 underline the linear dependence of the measurements. Thus the expected square-root dependence of multiple scattering power on the scattering material thickness for randomly distributed micro-scattering particles is experimentally verified. This dependence was included in the approach for deriving the *model of multiple scattering* (Equation 2-18).

5.1.3 Dependence of multiple scattering power on photon energy

The main assumptions for the elaboration of the model of multiple scattering and the calculation of multiple scattering power from the single scattering power in chapter 2 are: (i) scattering is considered due to refraction, (ii) the scattering microparticles have a homogeneous refractive index and (iii) absorption is negligible. Hence, scattering power is identified as being proportional to the real part of refractive index δ (Equation 2-13, Equation 2-16). Measurements for this work are acquired at photon energies far away from absorption edges. On this energy scale the real part of refractive index δ is proportional to $1/E^2$ where E is the photon energy (Equations 1-3) [LBL, 2002]. Hence, if the *model of multiple scattering due to refraction* provides a good model of nature, a $1/E^2$ dependence of scattering power is expected. The experimentally determined scattering powers of sub-section 5.1.1 are plotted versus the inverse square of photon energy (Figure 5-4).

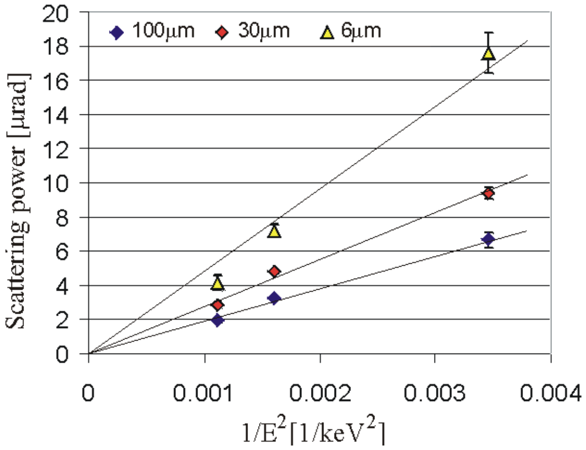

Figure 5-4 Dependence of scattering power on photon energy derived from the experiments (run SYRMEP/ELETTRA Trieste, 04/2002) with the 100 µm, 30 µm and 6 µm PMMA sphere specimens.

The plot presents the mean values of each specimen, which are derived from normalising the scattering powers to the scattering thickness *d*.

Figure 5-4 demonstrates the $1/E^2$ dependence of scattering power. Thus the *model of multiple scattering due to refraction* seems to be a good model for further investigations.

5.1.4 Verification of the model of multiple scattering due to refraction for weakly absorbing specimens by experiments with synthetic specimens

This sub-section introduces the experimental verification of calculating the multiple scattering power from the single scattering PMMA sphere specimen geometry, identified by the single scattering power of a micro sphere, and the Central Limit Theorem (Equation 2-18).

The single scattering power of the micro sphere geometry is calculated in sub-section 2.2.2 and some scattering powers for a PMMA micro sphere are summarised in Table 2-1. Hence has to be determined the mean number *N* of scattering particles for the PMMA sphere specimens. Therefore, calculations of independent absorption measurements of the same specimens are made. The packing factor of the PMMA micro sphere specimens is determined by the absorption images and determined from the attenuation coefficient μ. Absorption measurements acquired at 17 keV and 25 keV photon energy are used for the calculations. Measurements acquired at 30 keV photon energy are skipped because of weak attenuation. The results are presented in Table 5-2.

Table 5-2 Calculated packing factor for PMMA sphere specimens by absorption exposures, SYRMEP/ELETTRA 04/2002

Sphere diameter [µm]	Energy [keV]	Packing factor PMMA sphere specimens [%]	Mean packing factor sphere specimens [%]
100	17	52.8	51.7 ± 0.9
100	25	51.6	
30	17	42.1	43.1 ± 1.8
30	25	43.4	
6	17	46.1*	47.1* ± 1.9
6	25	48.8*	

*) Inhomogeneous distribution of material, calculations for compact regions

The material distribution of the 6μm spheres was inhomogeneous, visible by eye and clearly visible in the exposures (see Figure 4-4, middle right). Therefore, the measurements with the 6 μm sphere specimens are abandoned for the following experimental verification.

The comparison of calculated scattering power of the specimens using the single scattering power of a PMMA micro sphere (Table 2-1, Equation 2-18) with the experimentally determined scattering powers from section 5.1.1 is presented in Figure 5-5.

Figure 5-5 demonstrates a reasonable agreement of the scattering power calculated by using the scattering power of a single PMMA micro sphere and the individually determined packing for the specimens with experimental data, with the general dependence well reproduced. However, the slope is slightly different. A number of reasons could account for this systematic deviation, the most probable being a real arrangement of the spheres between completely random and regularly organized.

Thus calculation of multiple scattering power using the single scattering power of a single micro sphere is successfully applied to synthetic specimens. Sub-sections 5.1.6 and 5.1.7 demonstrate the application to soft tissue.

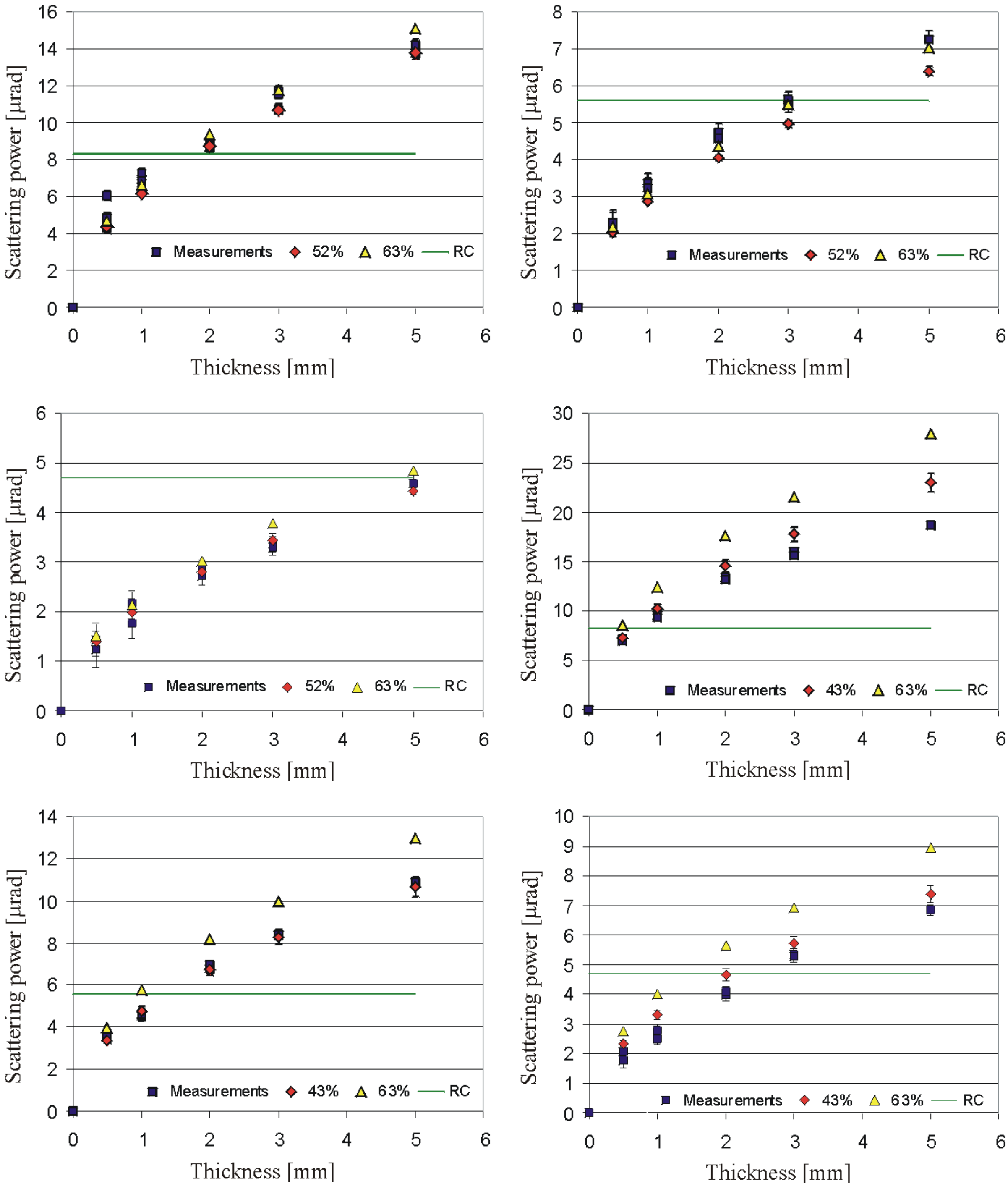

Figure 5-5 Comparison of calculated scattering power by using the single scattering power of a PMMA sphere with the experimentally determined scattering power performing the 100 µm and 30 µm sphere specimens acquired @17 keV, 25 keV and 30 keV photon energy (SYRMEP/ELETTRA 04/2002). 100µm spheres: upper left 17 keV, upper right 25 keV and middle left 30 keV photon energy. 30 µm spheres: middle right 17 keV, lower left 25 keV and lower right 30 keV photon energy. The blue squares mark the experimentally determined values of sub-section 5.1.1. The red rhombi mark calculations using the single scattering power of Table 2-1 and the packing density of Table 5-2. The yellow triangles mark calculations taking into account a typical packing for jammed packing [Donev et al., 2004]. The green line marks the Gaussian sigma of the analyser crystal RC. Due to the previous corrections the calculated values have to be multiplied with factors given in Table 2-2.

5.1.5 Experimental determination of the total scattering power of soft tissue

In this sub-section, a DEI experiment with a nitrogen cooled cow lung tissue specimen is analysed. Preparation of the specimen and the experiment were described in sub-section 4.1.3. Figure 5-6 illustrates the exposures acquired at 25 keV photon energy.

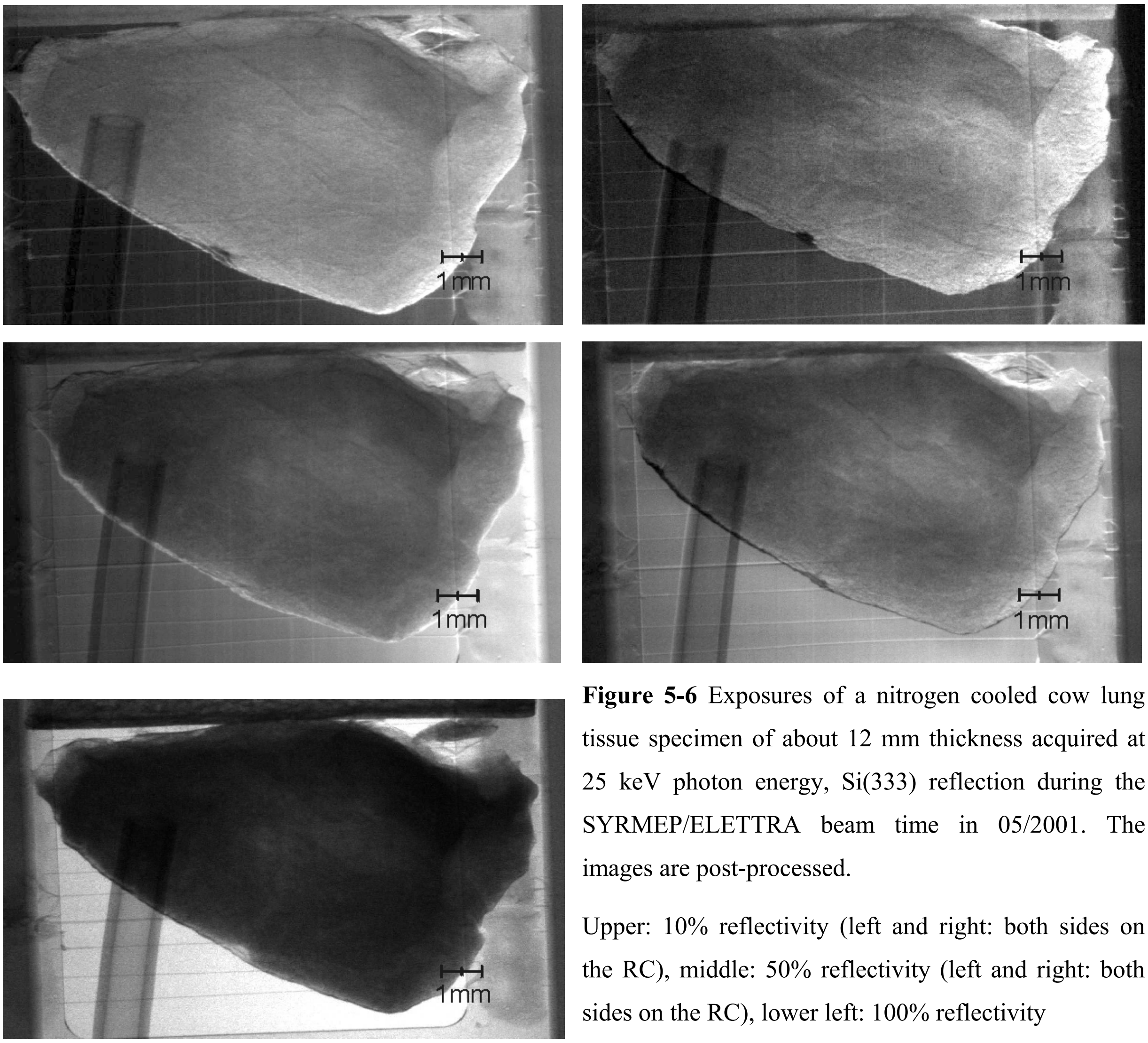

Figure 5-6 Exposures of a nitrogen cooled cow lung tissue specimen of about 12 mm thickness acquired at 25 keV photon energy, Si(333) reflection during the SYRMEP/ELETTRA beam time in 05/2001. The images are post-processed.

Upper: 10% reflectivity (left and right: both sides on the RC), middle: 50% reflectivity (left and right: both sides on the RC), lower left: 100% reflectivity

Different specimen details are emphasised at different analyser crystal positions or illumination. The cooling tube is visible in each image on the lower left. Deflation of the lung tissue specimen during the experiment can be observed (see upper left and right).

Significant signals in the images acquired with the analyser set to 10% reflectivity indicate a significant scattering power. Different specimen details occur at different analyser crystal position or in other words, illumination of the specimen. Thus the specimen seems to offer various scattering power in different regions. For a more detailed data analysis, the X-ray image of the lung specimen was separated into several regions of interest as shown in Figure 5-7.

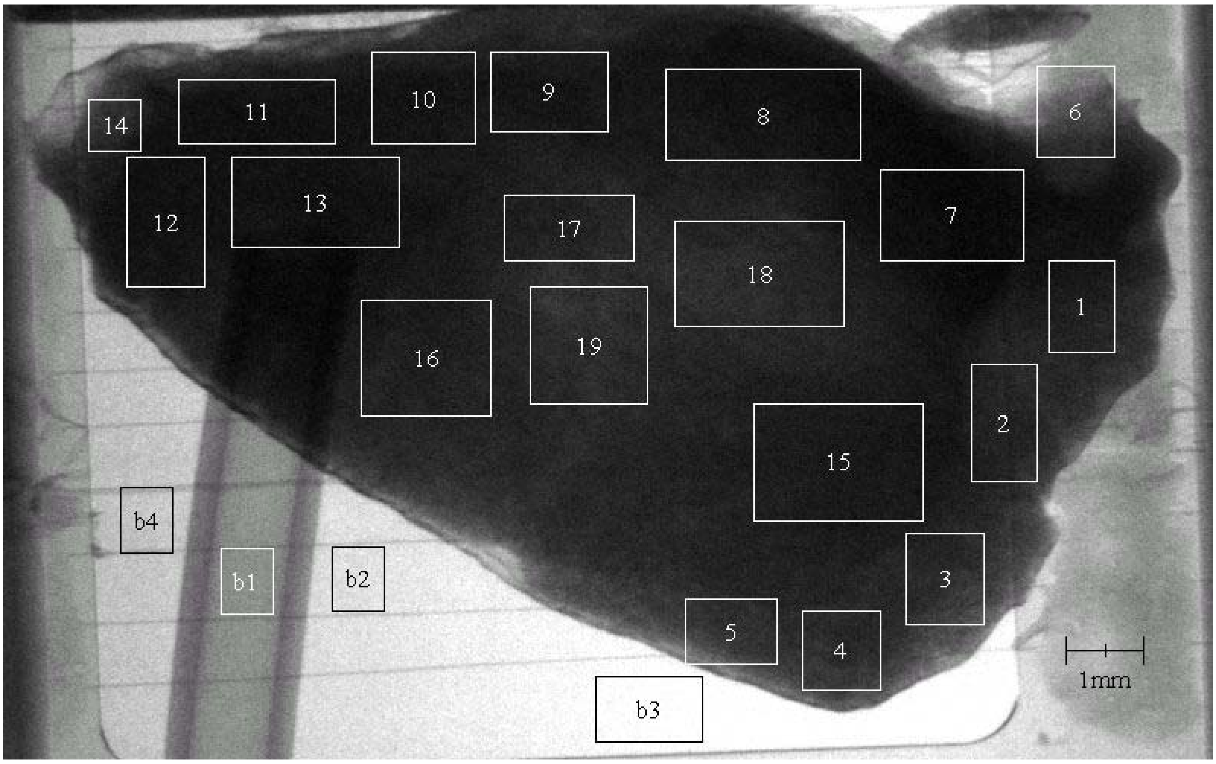

Figure 5-7 Separation of the cow lung tissue specimen image in several regions of interest, image acquired at 25 keV photon energy using the Si(333) reflection (run SYRMEP/ELETTRA 05/2001, image post-processed).

The average intensity is calculated for each region of interest. A Gaussian fit of the average intensities plotted versus the analyser crystal positions provides the scattering power in the regions of interest. The multiple scattering power for each region of interest of the cow lung tissue specimen is derived by subtracting the Gaussian sigma σ_{RC} of the analyser rocking curve (see Equation 5-1). Deflation of the cow lung tissue specimen was observed during the experiment. Thus initial and final exposures are treated separately. The determined scattering powers of the regions of interest divided in initial and final exposures are summarised in the histogram of Figure 5-8. The comparison of initial and final multiple scattering power of the cow lung tissue specimen demonstrates clearly the decrease of multiple scattering power during the experiment.

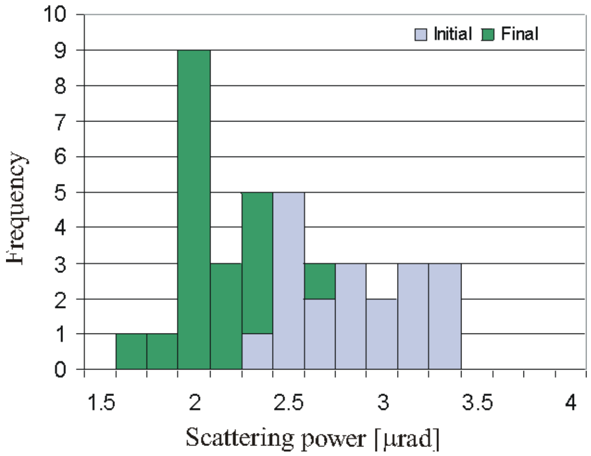

Figure 5-8 Calculated scattering power of 12 mm lung tissue specimen at various regions of interest (Figure 5-7), Si (333) reflection, 25 keV photon energy (SYRMEP/ELETTRA 05/2001)

Clearly appears the significant decrease of multiple scattering power of the cow lung tissue specimen during the experiment.

Calculations of the mean scattering power for the initial and final exposures of all regions of interest deliver:

$$\overline{\sigma_{lung,initial}} = 2.91 \pm 0.25 \mu rad$$

$$\overline{\sigma_{lung,final}} = 2.43 \pm 0.17 \mu rad$$

Skipping the regions of interest near the specimen boarder (*1, 2, 3, 4, 5, 6* and *14*) delivers the mean scattering power for the middle part of the specimen: Which delivers a clear significant increase of multiple scattering power of the cow lung tissue specimen during the experiment.

$$\overline{\sigma_{lung,initial,sel}} = 3.22 \pm 0.18 \mu rad$$

$$\overline{\sigma_{lung,final,sel}} = 2.44 \pm 0.18 \mu rad$$

The experimental data for multiple scattering power of the cow lung tissue are verified by analysing in the image background intensity (b_1 to b_4 see Figure 5-7). In the background regions no additional scattering is present. According to Equation 5-1, the Gaussian sigma of the Si (333) analyser crystal σ_{RC} is expected as a result of these calculations. From the analysis of the image background intensity results $\sigma_{background}$:

$$\overline{\sigma_{background}} = 1.07 \pm 0.03 \mu rad$$

This value is in good agreement with the theoretical width of the rocking curve calculated with the IDL [RSI] utility PEPO [Schulze, 1993] and shows good agreement.

$$\sigma_{RC,Si(333),25keV} = 1.09 \mu rad$$

In this section, the scattering powers of the cow lung tissue specimen were calculated. A comparison of multiple scattering powers in initial and final exposures demonstrated the decrease of multiple scattering powers during the experiment. Unfortunately the cow lung tissue specimen was not suitably prepared from the medical point of view [Duncker, 2004]. The condition and initial status of the cow lung tissue specimen were undefined. Nevertheless, the experimentally determined multiple scattering powers are in agreement with the predictions for lung tissue and alveoli (sub-section 2.5.2) taking into account partial deflation of the lung tissue (sub-section 5.1.6).

5.1.6 Preliminary results and predicting the multiple scattering power of soft tissue: Motivations for new DEI experiments

Section 2.5 introduced the determination of the multiple scattering power of lung tissue by calculating the scattering power of a single alveolus and performing the Central Limit Theorem. The calculations predicted a scattering power of 12 mm thick lung tissue for alveoli size between 250-500 μm in diameter in the range of 5.6 μrad to 3.7 μrad (Figure 2-22). Predicted values are of the same order as the measurements (see Figure 5-8). In addition, measurements of the cow lung tissue specimen demonstrate a significant decrease of multiple scattering power from initial exposures to exposures acquired during the second part of the experiment. Thus a partial deflation of the tissue is taken into account for the calculatio of scattering power. Calculations are made for a multiple scattering specimen offering only a fraction of its maximum multiple scattering power. Figure 5-9 shows the calculated scattering powers for fractional available multiple scattering power versus the alveoli diameter.

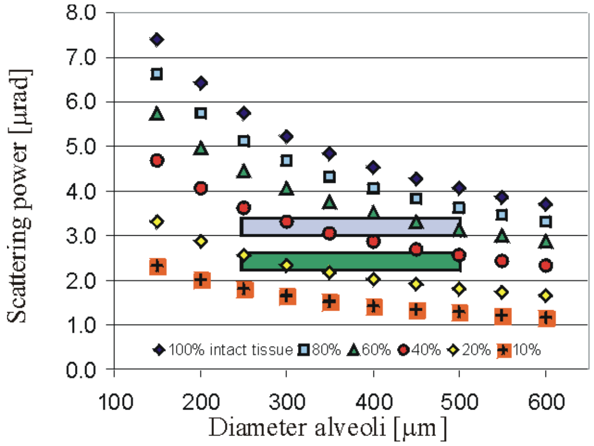

Figure 5-9 Influence of various fractions of intact tissue on calculated scattering power for 12 mm thick lung tissue versus alveoli diameter @25 keV photon energy. It is assumed that the alveoli are filled with alveolar air.

The plotted values for 100% intact tissue correspond to a jammed disordered packing fraction of about 64%.

The blue square indicates the mean value of multiple scattering powers of the initial exposures for the middle part of the cow lung tissue specimen. The green square indicates the calculated multiple scattering power for the final exposures (sub-section 5.1.5, compare Figure 5-8).

Figure 5-9 clearly demonstrates the influence of various fractions of intact tissue on the scattering power. The experimentally determined multiple scattering powers for the middle part of the lung tissue specimen (sub-section 5.1.5) indicated by the squares in Figure 5-9 demonstrate agreement with the predicted values for lung tissue multiple scattering power for partial deflation of the specimen. From Figure 5-9 could be expected, that the lung tissue specimen in the initial stadium of the experiment was approximately 40% to 60% intact and in the final stadium of about 20% to 40%. These values seem to be realistic. But definitive conclusions cannot be drawn because of the uncertainties in specimen preparation. Thus, the good agreement should deliver a motivation for repeating the experiments with well-prepared specimens.

5.1.7 Further quantitative verification of the predicted multiple scattering power for soft tissue

Because of uncertainties in specimen preparation, a final quantitative verification of the predicted multiple scattering power for lung tissue could not be performed in sub-section 5.1.6. For further verification is cited an approach about the investigation of speckles in lung tissue images [Kitchen et al., 2004]. He performed a Monte-Carlo simulation using 145 alveoli in projection to simulate 11.6 mm thick mouse lung tissue. The histogram containing the recorded "refraction angles Δθ" of his simulations is shown in Figure 5-10.

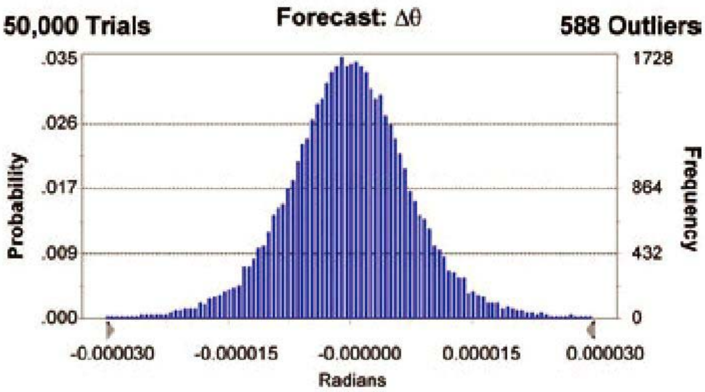

Figure 5-10 Simulation of scattering angle Δθ distribution of 11.6 mm thick mouse lung tissue @33 keV by [Kitchen et al., 2004]: "The simulated net refraction angle Δθ, for 50,000 rays through a simulated 11.6 mm thick mouse lung with 145 alveoli in projection, plotted as a histogram"

Determining the FWHM of the histogram and calculating σ, the scattering power of the mouse lung tissue by simulation is:

$$\sigma_{\text{mouse lung tissue, 33 keV by Kitchen}} = 6.8\ \mu\text{rad} \pm 0.2\ \mu\text{rad}$$

Applying Equation 2-18 to mouse lung tissue containing 145 alveoli in projection acquired at 33 keV photon energy, where the scattering power of a single alveolus is identified by sub-section 2.5.1, gives a scattering power of:

$$\sigma_{\text{mouse lung tissue, 33 keV by scattering power single alveolus}} = 7.15\ \mu\text{rad} \pm 0.21\ \mu\text{rad}$$

The scattering power calculated by using the scattering power of a single alveolus is in good agreement with the scattering power determined by Monte-Carlo simulations.

5.1.8 Summary

The investigations on multiple scattering properties of this section can be summarised as follows:

(i) Scattering power is determined by DEI experiments using synthetic specimens with random scattering properties. Thus scattering power is quantitatively identified and a range for scattering powers is determined.

(ii) Some basic scattering properties of randomly distributed structures are determined. The square-root dependence of scattering on the thickness of the scattering layer and the dependence on inverse photon energy confirm the assumptions made for the model of *multiple scattering due to refraction* introduced in chapter 2.

(iii) The calculation of multiple scattering power using the scattering power of a single microparticle and the Central Limit Theorem is verified by the DEI experiments using synthetic specimens with randomly distributed scattering particles.

(iv) Experimentally determined scattering powers for the nitrogen cooled lung tissue specimen are in agreement with the predicted scattering powers by using the calculated scattering power of a single alveolus and considering partial deflation of the specimen. But uncertainties in specimen preparation do not allow a definitive experimental verification.

(v) Comparison of the method for calculating the scattering power developed here with the Monte-Carlo simulation of mouse lung tissue by the Australian DEI group [Kitchen et al., 2004] is in good agreement.

5.2 The strong influence of the analyser crystal: A method for designing DEI experiments with multiple scattering, and limitations of the DEI technique

The influence of the analyser crystal on a scattering signal is identified in this section. The analyser influence on a scattering signal is presented in sub-sections 5.2.1 and 5.2.2 by considering the image contrast. In addition, a common DEI algorithm is applied to the acquired images, which demonstrates a strong quantitative signal falsification (sub-section 5.2.3). The analyser crystal influence is experimentally verified and quantitatively reconstructed by Monte-Carlo simulations in sub-section 5.2.4. It is found to be a useful tool for designing DEI experiments and fixing limitations in using DEI. The importance for DEI experiments with soft tissue and DEI as a method for a new generation lung radiology is discussed in sub-section 5.2.6.

5.2.1 Experimental demonstration of the sensitive relationship of total scattering power and photon energy in the analyser's 10% reflectivity mode

Specimens with mainly single refraction properties can be detected with highest image contrast in the analyser's 10% reflectivity mode [Pillon, 2000] and considerable contrast is observed for scattering material [Arfelli et al., 2002]. Thus the analyser's 10% reflectivity mode seems to be interesting for contrast considerations. This sub-section demonstrates the influence of multiple scattering on the image contrast using various multiple scattering powers at several photon energies. A sensitive relationship between the three main parameters, namely multiple scattering power, analyser crystal properties and photon energy, is clearly observed in the experimental data. Substitution of the multiple scattering properties with the total multiple scattering power and implementation in Monte-Carlo simulations reconstructs the relationship observed during the experiments as presented in sub-section 5.2.2. In addition, the use of scattering power for macroscopic considerations of multiple scattering power is demonstrated with the prospect of designing experiments and evaluating limits using DEI.

DEI images acquired around the analyser crystal’s 10% reflectivity mode demonstrate significant signals due to multiple scattering as illustrated in Figure 5-11.

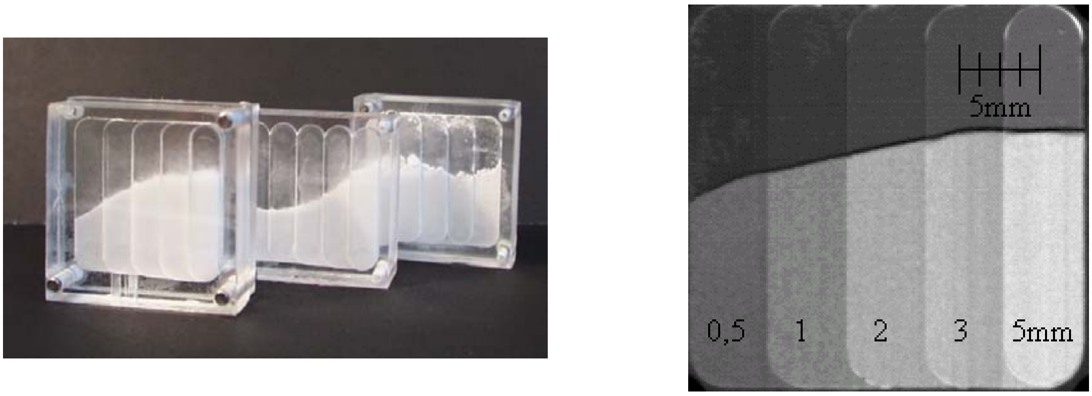

Figure 5-11 Multiple scattering properties acquired in the 10% analyser reflectivity mode

Left: Photo of specimens: Stepped PMMA specimen container with sectors of 0.5 mm to 5 mm thickness. The containers are filled with PMMA spheres of different diameter.

Right: DEI image of 100 μm spheres @25 keV photon energy in 10% analyser reflectivity mode, from left to right: 0.5mm to 5mm sectors (ID17/ESRF 04/2003, image post-processed).

Slight variations of the analyser crystal angle can lead to significant contrast changes as demonstrated as follows:

The image contrast *C* is defined as:

$$C = \frac{I_{scatt} - I_{\min}}{0.5 \cdot (I_{scatt} + I_{\min})}, \qquad \textbf{Equation 5-3}$$

where I_{scatt} is the average intensity within the scattering sectors and I_{min} the average background intensity [Beutel et al., 2000]. The contrast is calculated by deriving the mean intensity of each scattering region and photon energy with respect to the exact crystal position around the 10% analyser’s reflectivity position, with is represented by the reflectivity *R*. Figure 5-12 illustrates a sensitive contrast dependence on the analyser’s reflectivity.

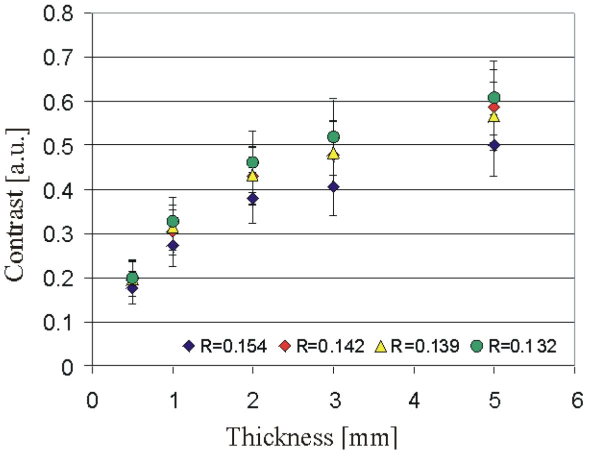

Figure 5-12 Experimentally determined contrast versus scattering thickness for various slight variations around the analyser crystal 14% reflectivity position, 100 µm sphere specimen @25 keV photon energy (ID17/ESRF 04/2003).

A variation of contrast is observed by slightly changing the analyser's position and therefore reflectivity *R*.

Figure 5-13 presents the contrast values versus scattering thickness for different scattering powers at 25 keV photon energy.

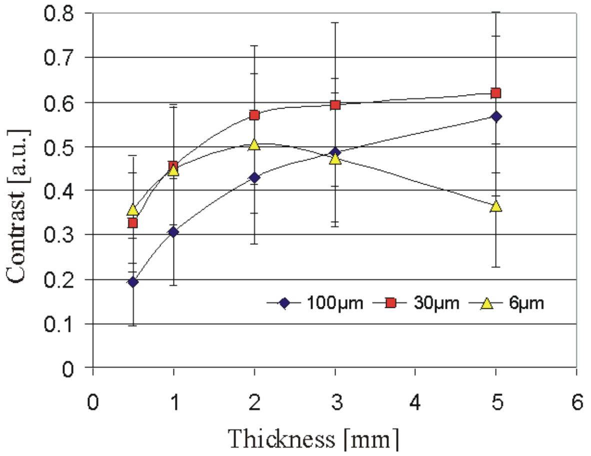

Figure 5-13 Experimentally determined contrast versus scattering thickness for the sphere specimen exposures exemplary @25 keV photon energy acquired in 14% analyser position for 100 µm, 30 µm and 6 µm sphere specimens (ID17/ESRF 04/2003, 08/2003).

Various contrast profiles can be recognised as (i) increasing contrast for increasing scattering thickness (Figure 5-13, blue rhombi), (ii) saturation for increasing scattering thickness (red squares) and (iii) decreasing contrast for increasing scattering thickness (yellow triangles). A nearly linear shape was recognised at 60 keV photon energy. Analysis of the experimental data demonstrates:

(i) The dependence of image contrast on multiple scattering power and energy.

(ii) The dependence of image contrast on slight variations in the analyser reflectivity position.

5.2.2 Reconstruction of contrast profiles by Monte-Carlo simulation using the total multiple scattering power

The different contrast profiles are reconstructed by Monte-Carlo simulations using the experimentally determined scattering powers from sub-section 5.1.1. The reconstructed contrast profiles are illustrated in Figure 5-14.

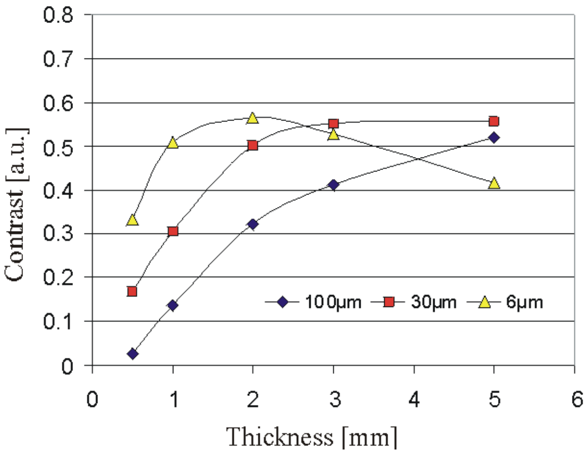

Figure 5-14 Reconstruction of contrast profiles by Monte-Carlo simulation with 15 million events using the scattering power of sub-section 5.1.1, analyser reflectivity position 14% @25 keV photon energy for 100 µm, 30 µm and 6 µm sphere specimens.

The comparison of the image contrast reconstruction (Figure 5-14) with the experimental data (Figure 5-13) demonstrates good quantitative agreement.

In order to understand the various contrast profiles, the scattering angle distributions are plotted for different sphere diameters and various specimen thicknesses in Figure 5-15. The scattering angle distributions are plotted as recorded in the protocol file of the Monte-Carlo simulations (see section 2.3), where the experimentally determined scattering powers from sub-section 5.1.1 are included to the Monte-Carlo simulation by a Gaussian shape.

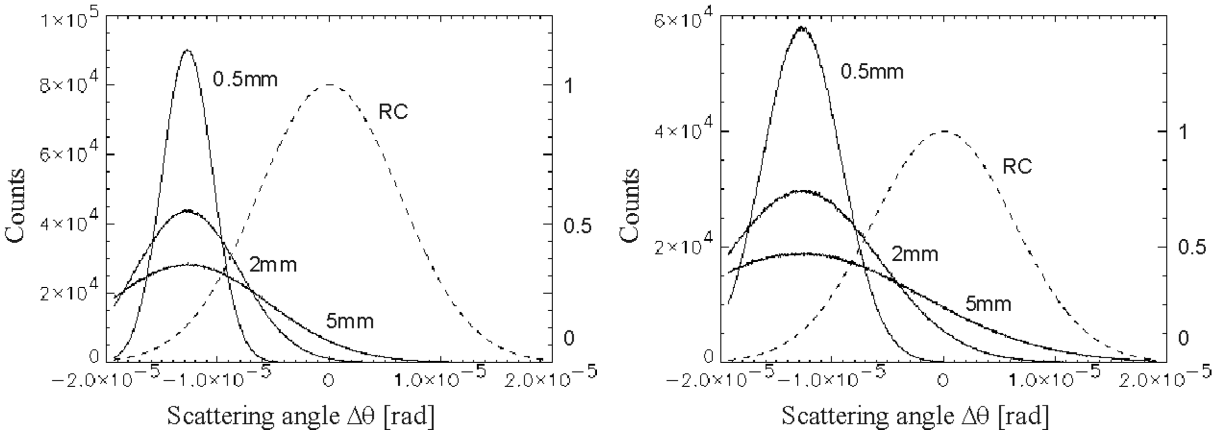

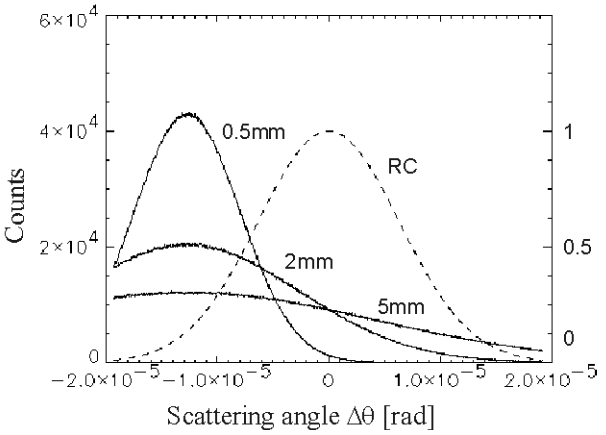

Figure 5-15 Scattering angle distribution from the Monte-Carlo protocol file of 100 µm, 30 µm and 6 µm diameter PMMA spheres @25 keV photon energy in the analyser's 10% reflectivity mode with respect to the analyser rocking curve (RC, broken line) for various thickness. The Monte-Carlo simulations are performed on 15 million events, the experimentally determined scattering powers from sub-section 5.1.1 were included.

Upper left: 100 µm spheres, upper right: 30 µm spheres and lower left: 6 µm spheres.

The contrast in the analyser's low reflectivity position of about 10% demonstrated the sensitive dependence on multiple scattering power and analyser reflectivity mode. In case of strong multiple scattering power, the amount of the scattering signal cut by the analyser crystal is increasing, if the scattering power is increasing.

5.2.3 Falsification of a refraction signal due to multiple scattering

The PMMA sphere specimens are again used to generate various scattering power. In addition, a well-defined refraction signal is used, derived from the trapezoidal PMMA specimen (Figure 4-2). The influence of multiple scattering of a well-defined signal is investigated using the experimental equipment presented in Figure 5-16 (left).

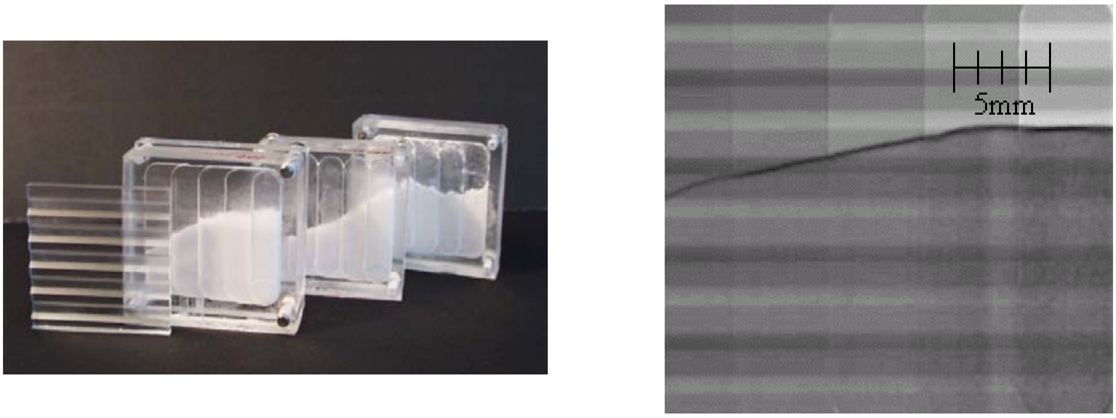

Figure 5-16 Influence of multiple scattering on a well-defined refraction signal.

Left: Combination of the trapezoid generating a well-defined refraction signal and PMMA sphere specimens to simulate various multiple scattering effects.

Right: DEI image of the trapezoid in combination with 100 µm sphere specimen acquired at 25 keV photon energy in 50% analyser mode
ID17/ESRF, 04/2003, image post-processed

The algorithm introduced by Chapman [Chapman et al., 1997] for calculating a refraction and an apparent absorption image does not include intrinsic multiple scattering. Calculating images of specimen with multiple scattering properties using the Chapman algorithm might lead to artefacts as demonstrated in the following. Exemplary is applied the Chapman algorithm and the calculated refraction image is shown in Figure 5-17 (left). The profile of the calculated refraction image (Figure 5-17, right) demonstrates clearly the artefacts due to scattering.

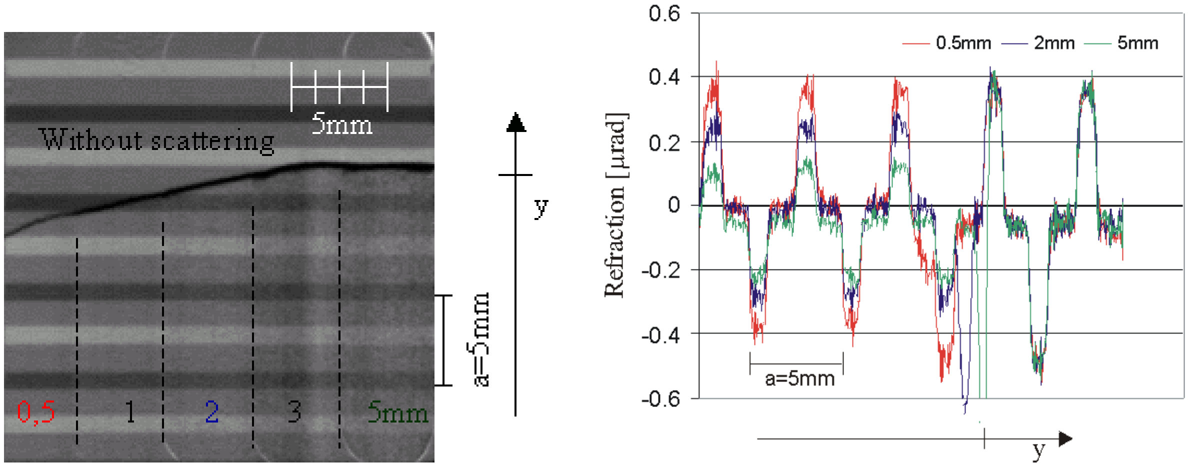

Figure 5-17 Calculations extracting the refraction information from the image.

Left: Refraction image according to the Chapman algorithm [Chapman et al., 1997], 100 µm spheres @25 keV, ID17/ESRF 04/2003, image post-processed.

Right: Mean refraction value resulting from the refraction image in various scattering regions, 100 µm spheres @25 keV photon energy. The values are determined calculating the mean value perpendicular to the marked y-axis in the image (right) for each scattering sector. ID17/ESRF 04/2003.

For clarity, the scattering regions are selected: 0.5 (marked red), 2 (blue) and 5 mm (green). The marked y-axis helps to find the correspondence between the two images, as also the mark at the y-axis.

The trapezoid inclination can be extracted from the refraction image (Figure 5-17). Normally, the refraction signal should consist of a constant maximum. Instead, a decrease of the refraction signal is recognised for increasing scattering thickness. The calculated inclinations in degrees are summarised with the average number of scattering microparticles corresponding to the scattering thickness in Table 5-3.

Table 5-3 Calculated inclination of the trapezoid by experiment with the influence of multiple scattering

Thickness [mm]	Calculated inclination [degrees]	Average number of scattering microparticles*
0	45.0	0.0
0.5	40.9	2.7
1	36.5	5.3
2	30.7	10.6
3	25.1	15.9
5	19.4	26.5

*) According to the packing factor determined by absorption, Table 5-2

The influence of multiple scattering can lead to a strong signal falsification if the DEI technique and common DEI methods are applied as demonstrates Table 5-3. From this fact can be drawn two conclusions:

(i) The analyser crystal definitively cuts the scattering signal. This fact appears clearly considering the scattering angle distributions Δθ with respect to the analyser rocking curve. For the investigation of new DEI algorithms this would mean that the consideration of acquired DEI images to extract information seems insufficient, because information is lost in the images. Rather, one should try to reconstruct the object plane from the acquired images taking into account the analyser's cutting properties.

(ii) Care must be taken for quantitative interpretation of DEI images using the Chapman algorithm in case of presence of multiple scattering. It has to be noted again that the Chapman algorithm does not consider multiple scattering. On the contrary, it is developed for a linear approximation of the rocking curve's 50% reflectivity position. Its application in case of multiple scattering can lead to a quantitative signal falsification. For an unknown specimen multiple scattering properties of the specimen might be unknown. Multiple scattering appears in biological specimens in lung tissue (5.1.5) and could be expected also in other soft tissue for instance in muscle fibres. This last point might be a motivation for further experiments on multi scattering tissue.

5.2.4 Quantitative reconstruction by simulations using the total scattering power

Image artefacts resulting from the Chapman algorithm in presence of multiple scattering can computationally be reconstructed as demonstrated in this sub-section. Therefore, the experimentally determined scattering power for each specimen thickness from sub-section 5.1.1 is used for Monte-Carlo simulation. The simulated images are processed in the same manner as the acquisitions in sub-section 5.2.3. For each scattering thickness, a refraction profile is obtained. The results of the simulations are illustrated in Figure 5-18. For simplifying the comparison the same selected thickness than in previous sub-section are presented. Figure 5-18 demonstrates the same decrease of determined refraction signal for increasing scattering thickness as the experiment in Figure 5-17. Thus, Monte-Carlo simulations applying the total scattering power deliver good agreement with the measurements.

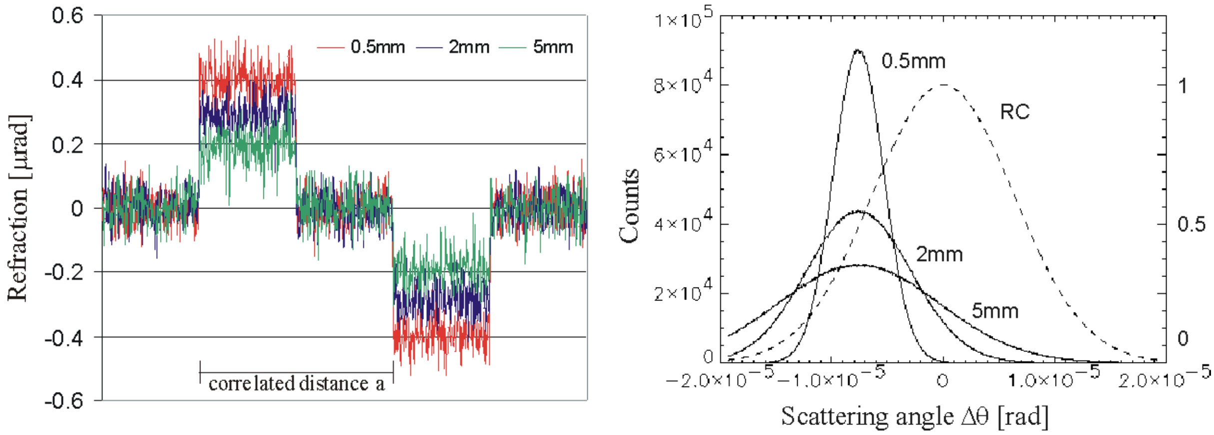

Figure 5-18 Reconstruction of refraction profile by simulation.

Left: Monte-Carlo simulation of refraction profile, 100 µm PMMA spheres @25 keV photon energy. The correlated distance *a* with respect to the experiment in Figure 5-17 is signed.

Right: Scattering angle distributions as recorded in the protocol files of the Monte-Carlo simulations, the experimentally determined scattering powers from sub-section 5.1.1 were included, 100 µm PMMA spheres @25 keV photon energy, 15 million events.

The exemplary selected scattering thicknesses are plotted respective to the analyser rocking curve (broken line).

The scattering angle distributions of the three selected scattering thicknesses, plotted with respect to the analyser rocking curve in Figure 5-18 (right), demonstrate clearly the strong influence of the analyser crystal on the signal. For high scattering power the signal is cut due to the analyser's filter property.

Fixing feasibility and limitations of common methods within DEI, the influence of low scattering power is considered. The specimen thickness is substituted by the total scattering power in order to become independent from the scattering material. Thus Figure 5-18 can be presented as shown in Figure 5-19.

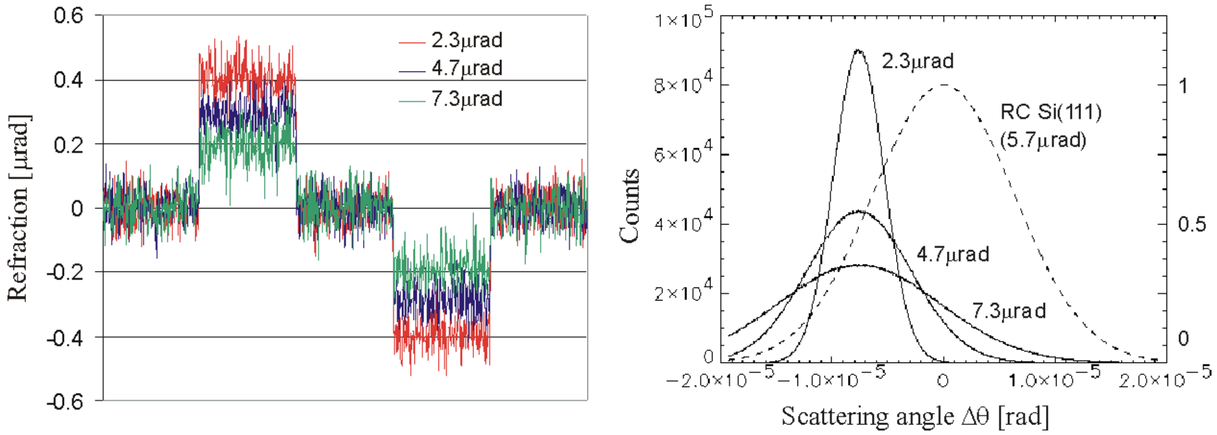

Figure 5-19 Consideration of the analyser crystal influence in case of high scattering power by calculation.

Left: Influence of high scattering power, calculated refraction profiles from Monte-Carlo simulations, 25 keV photon energy, and 15 million events. The high total scattering power demonstrates the decreasing of refraction signal.
Right: Scattering angle distributions for high scattering power with respect to the analyser rocking curve (broken line), 25 keV photon energy, and 15 million events. For high scattering power is the signal cut due to the filtering of the analyser crystal.

The same analysis on lower total scattering power shows that the maximum refraction values do not decrease any longer as demonstrated in Figure 5-20.

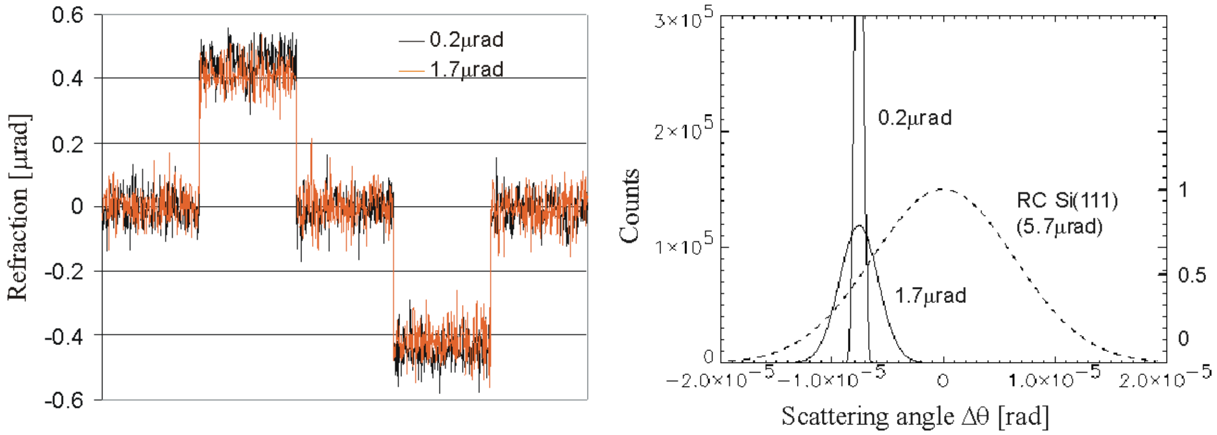

Figure 5-20 Consideration of the analyser crystal influence in case in case of low scattering power by calculation

Left: Influence of low scattering power, calculated refraction profiles from Monte-Carlo simulations, 25 keV photon energy, and 15 million events. For low scattering power occurs no significant decrease of the refraction signal.
Right: Scattering angle distributions for low scattering power with respect to the analyser rocking curve, 25 keV photon energy, and 15 million events. If the scattering power is sufficient low with respect to the analyser rocking curve (broken line), the signal is no longer cut due to the filtering of the analyser crystal.

5.2.5 Summary

The analyser's interacting with the scattering signal as considered in this section can be summarised as follows:

(i) The analyser crystal acts as strong angular filter when scattering is present. The scattering power might be in the order of magnitude than the analyser rocking curve Gaussian σ_{RC} just for a few of scattering microparticles. Thus the analyser crystal can severely cut a scattering signal.

(ii) The scattering power delivers quantitative characterisation of a specimen consisting of randomly distributed micro scattering particles. DEI measurements can be simulated applying the total scattering power to Monte-Carlo simulations. The macroscopic consideration of multiple scattering properties helps decisive to perform calculations for designing DEI experiments and evaluating limits in using DEI in case of multiple scattering.

5.2.6 Discussion: Prospective for lung measurements using DEI

Scattering power is quantified by experiment using synthetic specimens as well as a cow lung tissue specimen. The calculation of the single scattering power offers the possibility to calculate the multiple scattering power for randomly distributed and weakly absorbing microparticles. Thus scattering power can be calculated and delivers a quantitative characterisation of multiple scattering properties of specimens consisting of randomly distributed scattering microparticles.

The current section treats the influence of the analyser crystal to a scattering signal. If the scattering power is of the same order than σ_{RC}, a tremendous signal cut by the analyser crystal is observed. The angular filter property of an Si analyser crystal used in the (111) reflection is introduced in this section and described by using synthetic specimens. Scattering power of soft tissues calculated by the scattering power of a single alveolus is compared to experimentally determined scattering power of the synthetic specimens in order to discuss the applicability of the DEI method for lung studies and diagnostics as a new generation radiology technique.

In sub-section 5.1.5, a scattering power of about 1.7 µrad to 3.5 µrad at 25 keV photon energy was determined for the 12 mm thick cow lung tissue specimen. By using the scattering power of a single alveolus are predicted (sub-section 5.1.6) total scattering powers for 100% intact lung tissue in the range of 4.0 µrad to 5.7 µrad at 25 keV photon energy. In comparison, the scattering power of the 100 µm sphere specimen offers a total scattering power of 2.3 µrad to 7.3 µrad at 25 keV photon energy. Thus the 100 µm sphere PMMA specimen has a comparable scattering power at 25 keV photon energy. The scattering power of a rabbit lung of 50 mm thickness is calculated to 21.0 µrad and an 11.6 mm thick mouse lung to 12.5 µrad. Considerations made for a frontal thorax exposure of a human lung, assuming a lung thickness of about 10 cm, predict a scattering power in the range of 16.6 µrad to 21.4 µrad at 25 keV photon energy. The 6 µm PMMA sphere specimen has comparable scattering powers. Data analysis of the acquired images demonstrated strong influence of the analyser crystal with Gaussian sigma of 5.6 µrad. Thus the ratio between scattering power and Gaussian sigma of the analyser rocking curve is an important quantity for the cutting property of the analyser crystal. A relation proportional to the inverse photon energy $1/E$ is expected. Scattering power is proportional to $1/E^2$ (see sub-section 5.1.3, Equation 2-18) and σ_{RC} relates to $1/E$ [Matsushita et al., 1983]. Figure 5-21 presents the predicted ratio for an energy range from 25 keV to 60 keV photon energy.

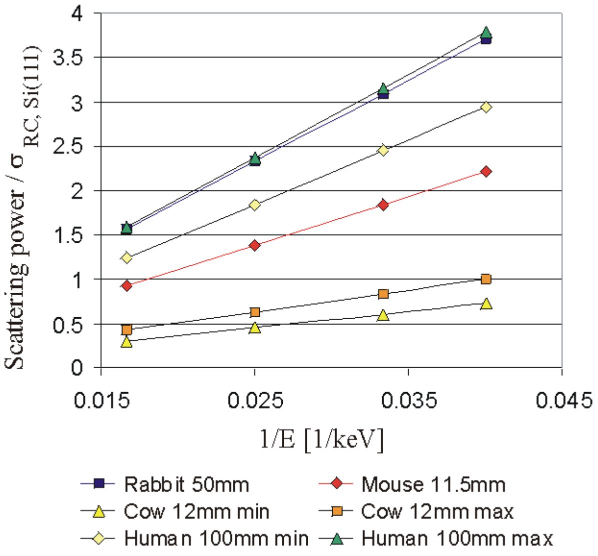

Figure 5-21 Calculated energy dependence of the ratio of the scattering power of various soft tissues and the Gaussian sigma σ_{RC} of the Si(111) rocking curve for an energy range between 25 keV and 60 keV photon energy.

The scattering values are calculated using the scattering power of a single alveolus (sub-section 2.5.2) and the Gaussian sigma of the Si(111) rocking curve calculated with the software tool PEPO [Schulze, 1993]. The predicted ratios are calculated for various soft tissues (see legend at the bottom). “Min” and “max” indicate calculations assuming minimal and maximal possible alveoli size for the tissues.

Figure 5-21 predicts a lower signal cut by the analyser crystal at higher photon energies. Higher photon energies are also preferable because of the lower quantum of absorbed X-ray radiation dose [Schneider, 1998]. A rabbit lung has similar multiple scattering powers than a human lung assuming minimum human alveoli size as shown in Figure 5-21 (blue squares for scattering power of a rabbit and green triangles for the scattering power of a human lung).

Another possibility to decrease the ratio of the scattering power and σ_{RC} of the analyser crystal might be the selection of a different material for the analyser crystal.

For pure diagnostic of a health lung might be also possible to use the signal cut by the analyser crystal demonstrated in sub-section 5.2.3 defining a "health scattering power" for lung tissue. From this point of view becomes the signal cut by the analyser crystal a desired effect. After all, the signal cut can be calculated.

5.3 Influence of micro-structures on multiple scattering power and verification by Monte-Carlo simulations

For randomly distributed and weakly absorbing microparticles is the multiple scattering power identified by the scattering power of a single microparticle and the average number of microparticle interactions per X-ray (Equation 2-18). This section focuses on the influence of periodical substructures on the multiple scattering power.

Analysis in this section is based on the lithography specimens and the experiments described in section 4.2. The specimens fabricated by X-ray lithography contain cylindrical holes arranged in a well-defined order. By rotating the specimen in respect to the X-rays incident wave, various sub-configurations of the scattering microparticles can be simulated. Five significant effects due to micro-structured scattering particles occurred in the experiment and are described and discussed in sub-section 5.3.1. Monte-Carlo simulations using the *model of scattering due to refraction* reconstruct these effects. Hence, another qualitative verification of the model of scattering due to refraction can be given in sub-section 5.3.2. The influence of substructures on the scattering power is identified by quanitative considerations using Monte-Carlo simulations. Prospects using the DEI method to detect microstructures are discussed in sub-section 5.3.3.

5.3.1 Qualitative effects of multiple scattering micro-structured specimens

A quantitative analysis of the images is not possible because of spatial resolution of the acquired images. The recorded material-hole sequence with different grey levels is restricted to a pixel range of about 10 pixels as can be seen for instance in the image shown in Figure 5-23. Anyhow, the acquired images show significantly effects resulting from the influence of microstructures.

The following analysis was done by mainly considering the images in the analyser's 50% reflectivity mode using the lithography specimen "Lit_16" (see section 4.2). The specimen has a perfect in-line structure of scattering particles with respect to the surface (Figure 5-22 and Figure 4-6 (right)).

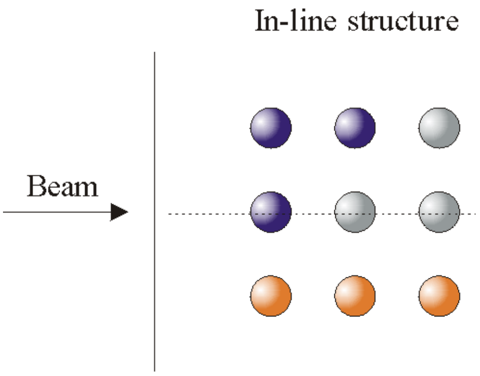

Figure 5-22 Schematic design of "in-line structure"

Substructures are perfectly organised in respect to the specimen's surface and the incident X-ray wave.

Five recognised effects are presented as follows:

(1) In-line structure of scattering particles; for a certain scattering thickness the typical "DEI-shadow" disappears, marked by the red arrow in Figure 5-23.

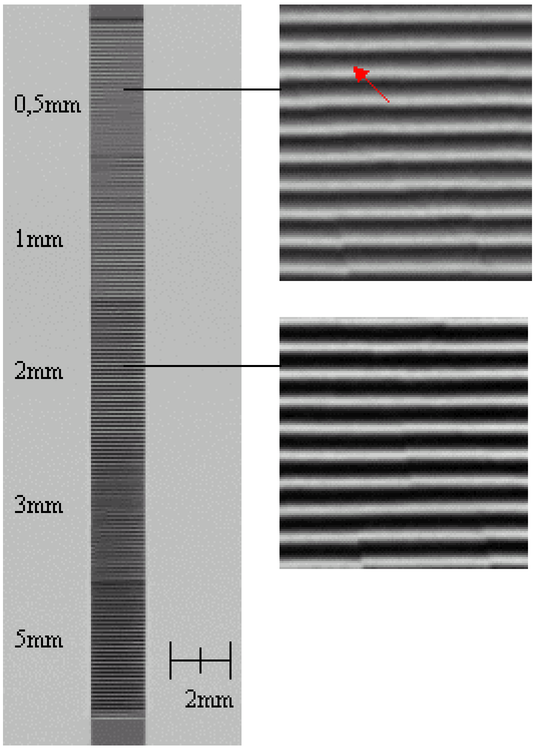

Figure 5-23 Image of "Lit_16" acquired in 50% analyser reflectivity mode at 17 keV photon energy, rotation: 0 degrees (SYRMEP/ELETTRA 10/2003, image post processed).

(2) Slight rotation of in-line structure; for increasing scattering thickness the deep zones becomes larger (Figure 5-24).

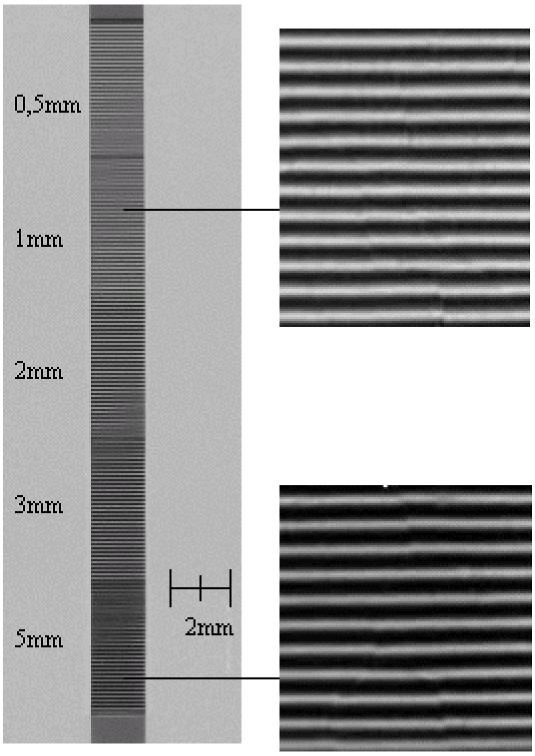

Figure 5-24 Image of „Lit_16“ acquired in 50% analyser reflectivity mode at 17 keV photon energy, rotation: 0.5 degrees (SYRMEP/ELETTRA 10/2003, image post processed).

(3) Slight rotated in-line structure, the typical “DEI shadow” pattern changes to reverse order for larger scattering thickness (Figure 5-25).

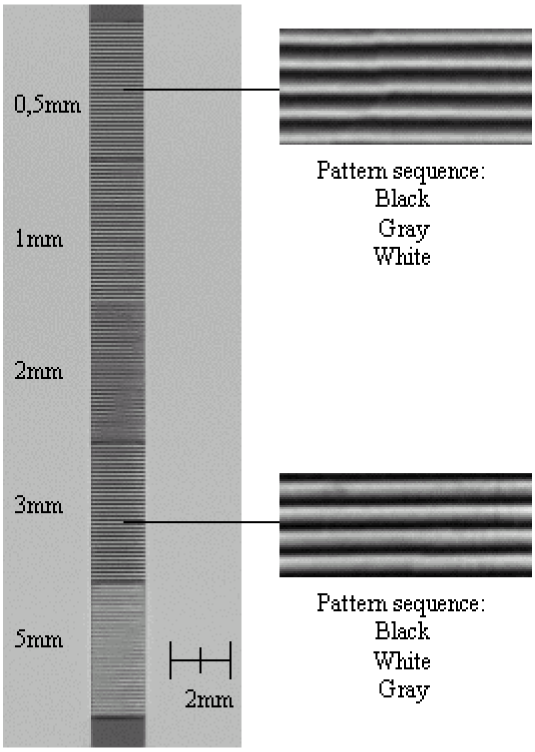

Figure 5-25 Image of „Lit_16“ acquired in 50% analyser reflectivity mode at 17 keV photon energy, rotation: 2 degrees (SYRMEP/ELETTRA 10/2003, image post processed).

(4) In-line structure, the structure disappears completely for certain rotations (Figure 5-26).

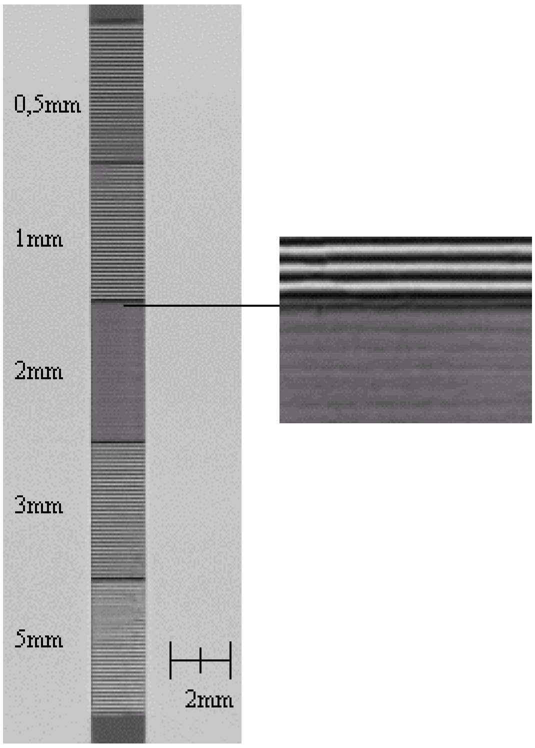

Figure 5-26 Image of „Lit_16“ acquired in 50% analyser reflectivity mode at 17 keV photon energy, rotation: 5 degrees (SYRMEP/ELETTRA 10/2003, image post processed).

(5) In-line structure, for certain rotations appears the double number of structure (Figure 5-27).

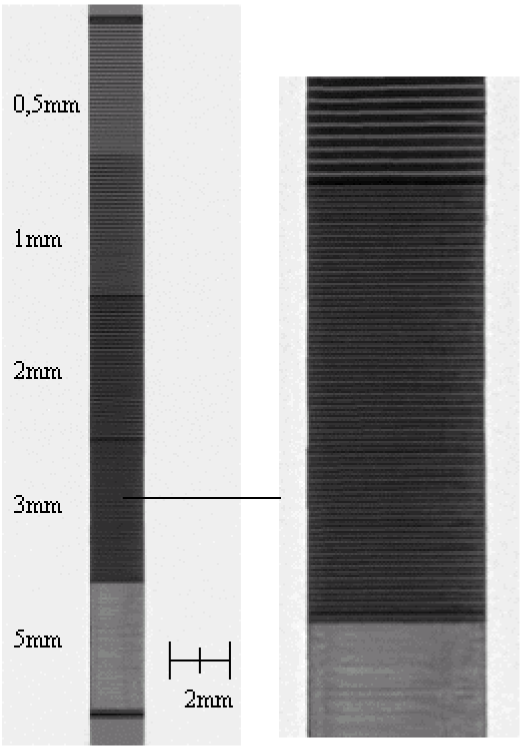

Figure 5-27 Image of „Lit_16“ acquired in 100% analyser reflectivity mode at 17 keV photon energy, rotation: 15 degrees (SYRMEP/ELETTRA 10/2003, image post processed).

5.3.2 Simulation of multiple scattering properties of micro-structures

In order to simulate the effects of multiple scattering structures presented in sub-section 5.3.1, Monte-Carlo simulations applying the model of scattering due to refraction and periodical substructures are performed. The Monte-Carlo simulations were executed in IDL [RSI] by the Monte-Carlo ray tracing introduced in section 2.3. The cylindrical microstructure and the rotation of the specimen are included by simulating periodical structures (see section 2.3). For the simulation of each effect is illustrated the Monte-Carlo generated image as well as the scattering angle distribution on the analyser crystal. The scattering angle distribution is plotted in comparison to the rocking curve of the analyser crystal in order to convey the influence of multiple scattering structures.

(1) In-line structure of scattering particles; for a certain scattering thickness the typical "DEI-shadow" disappears (Figure 5-28).
(2) Slight rotation of in-line structure; for increasing scattering thickness the deep zones becomes larger (Figure 5-29).
(3) Slight rotated in-line structure, the typical "DEI shadow" pattern changes to reverse order for larger scattering thickness (Figure 5-30).
(4) In-line structure, the structure disappears completely for certain rotations (Figure 5-31).
(5) In-line structure, for certain rotations appears the double number of structure (Figure 5-34, Figure 5-35).

All five observed experimental effects of multiple scattering properties due to periodical sub-structures can be Monte-Carlo simulated, which provides an additional verification for the *model of scattering due to refraction*.

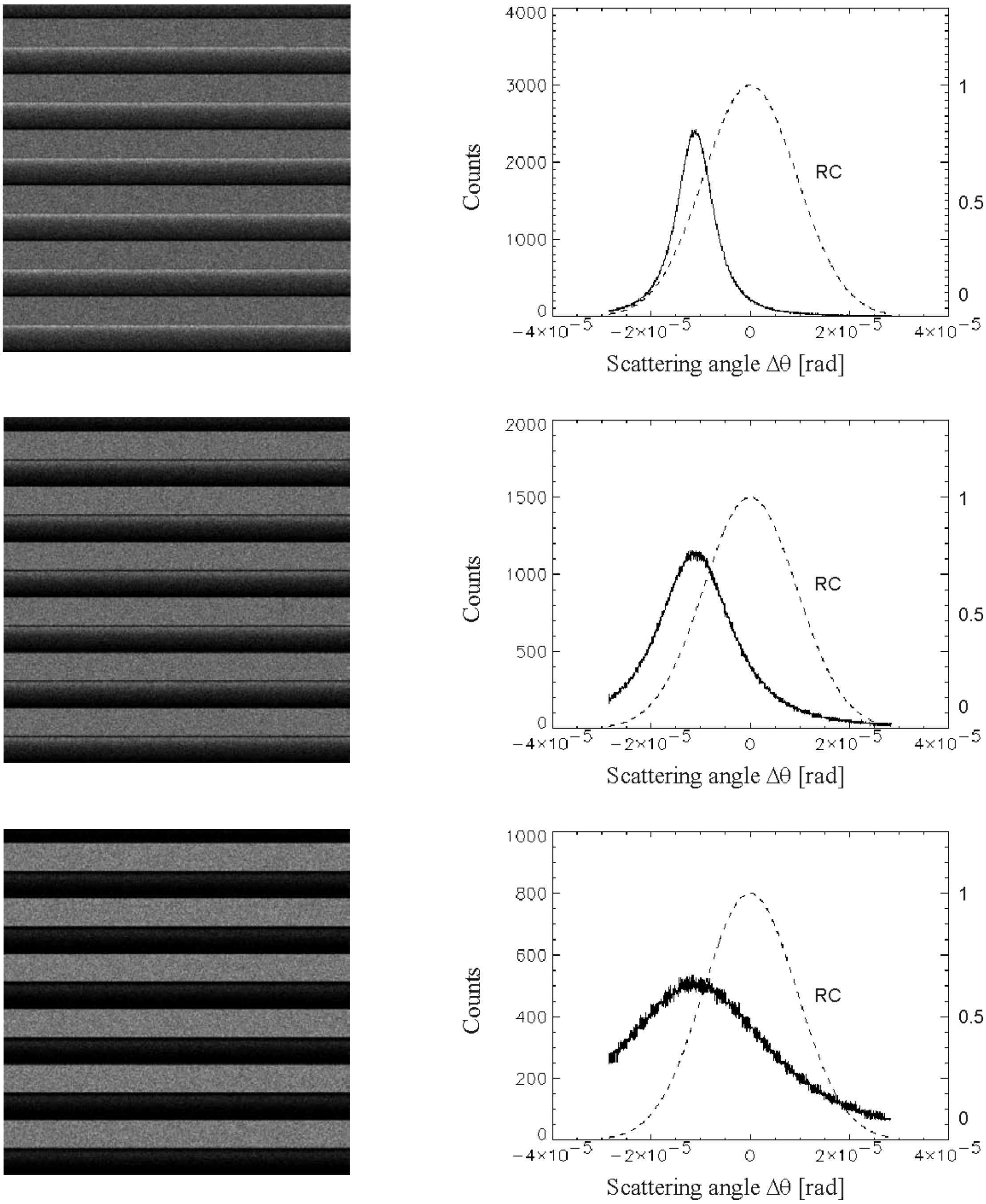

Figure 5-28 Monte-Carlo simulations of PMMA cylinder structures, in-line organisation, rotation 0 degrees, 17 keV photon energy, simulation for 10^7 events. Left: Simulated images, Right: Scattering angle distributions $\Delta\theta$. Upper: Simulation for 0.5mm sector corresponds to 3 layers, Middle: Simulation for 1mm sector corresponds to 6 layers, Lower: Simulation for 2mm sector corresponds to 12 layers.

The width of the scattering angle distribution increases rapidly with increasing number of micro-scattering particles that are arranged perfectly in line. For 12 in line organised PMMA cylinders @17 keV photon energy, the angular scattering distribution is as large as the Si(111) analyser rocking curve. Thus, the analyser crystal looses its filter properties and the typical “DEI shadow” disappears. The example delivers in addition a clear demonstration of the analyser’s angular resolution.

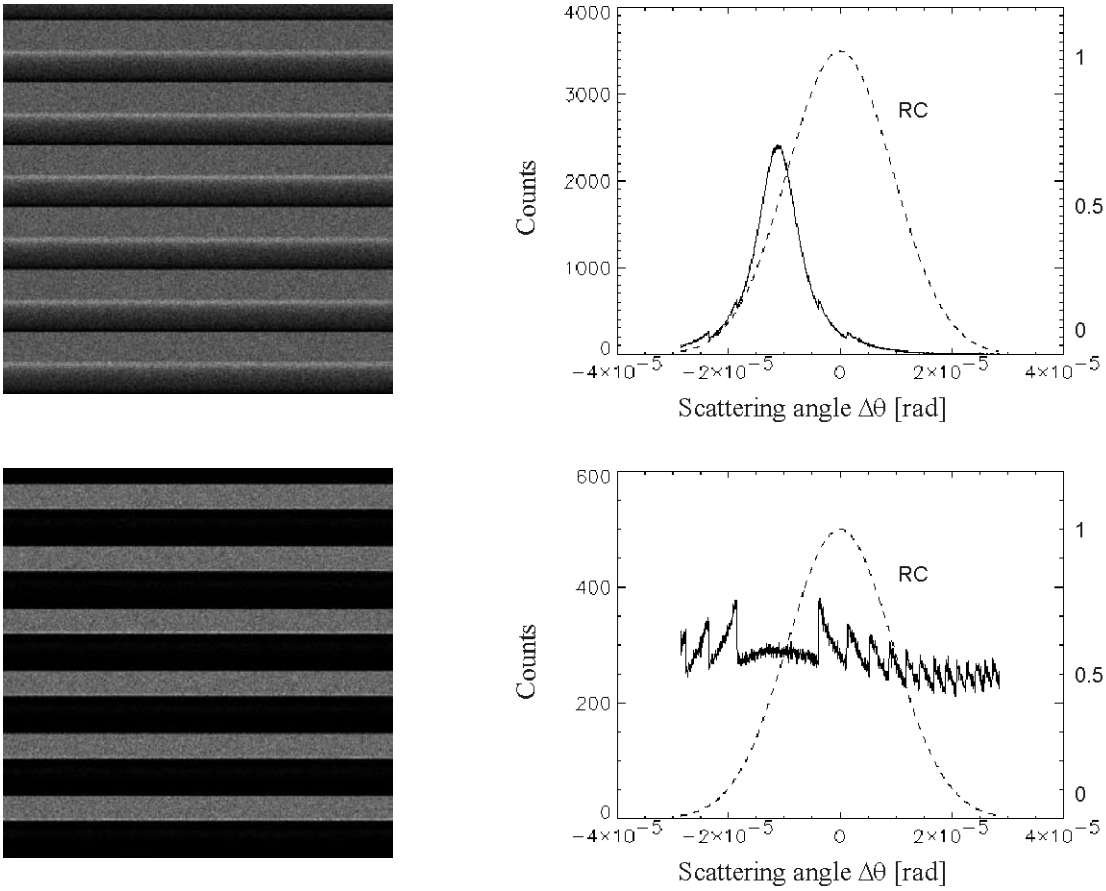

Figure 5-29 Monte-Carlo simulations of PMMA cylinder structures, in-line organisation, rotation 0.5 degrees, 17 keV photon energy, simulation for 10^7 events. Left: Simulated images, Right: Scattering angle distributions $\Delta\theta$.

Upper: Simulation for 0.5mm sector corresponds to 3 layers.

Lower: Simulation for 3mm sector corresponds to 18 layers.

As demonstrated in the images (Figure 5-24) the deep zones become lager for increasing scattering thickness while the specimen is slightly rotated.

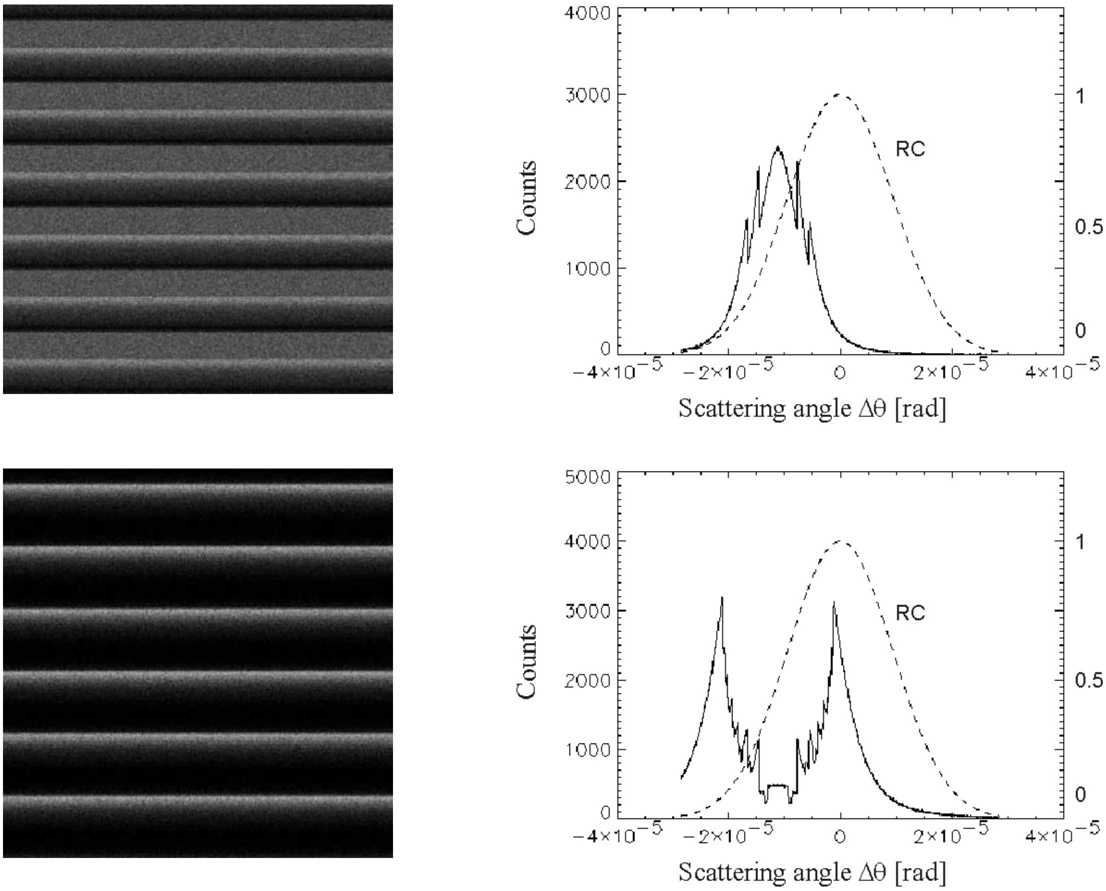

Figure 5-30 Monte-Carlo simulation of PMMA cylinder structures, in-line organisation, rotation 2 degrees, 17 keV photon energy, simulation for 10^7 events. Left: Simulated images, Right: Scattering angle distributions $\Delta\theta$.

Upper: Simulation for 0.5mm sector corresponds to 3 layers.

Lower: Simulation for 3mm sector corresponds to 18 layers.

The change for the typical “DEI shadow” pattern to reverse order for larger scattering thickness (Figure 5-25) can be reconstructed by simulation.

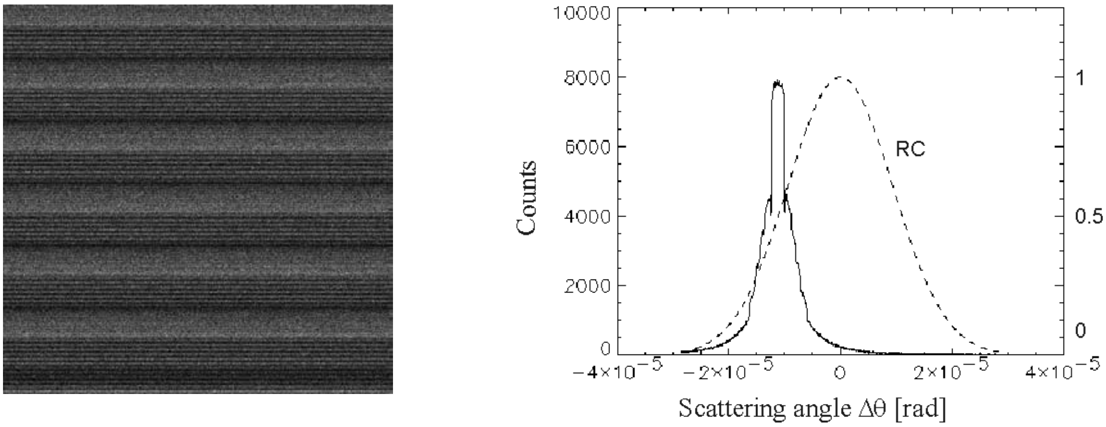

Figure 5-31 Monte-Carlo simulation of PMMA cylinder structures, in-line organisation, rotation 5 degrees, 17 keV photon energy, simulation for 10^7 events. Left: Simulated image, Right: Scattering angle distribution Δθ.

Simulation for 2mm sector corresponds to 12 layers.

The structure disappears when the specimen is rotated by a certain angle, so that the material distribution gets more or less homogeneous direction of the beam (Figure 5-26).

The effect can be explained by geometrical interface consideration in the case of disappearing structures as illustrated in Figure 5-32.

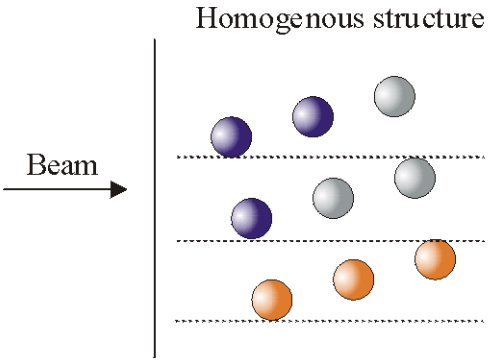

Figure 5-32 Schematic design of the "homogeneous structure".

Scattering microparticles are arranged in a more or less dense distribution (orange marked particles) in respect to the incident X-ray plane. In average, the structure information disappears for the multiple scattering.

A further reconstruction of disappearing structure is illustrated in Figure 5-33.

Figure 5-33 Monte-Carlo simulated image of dis-appearing structures.

Parameters set: PMMA cylinder structure, in-line organisation, 16 layers, rotation 4.16 degrees, corresponding to homogeneous structure @ 17 keV photon energy, simulation for 10^7 events.

The effect that the double number of structures appear, is a somehow trivial effect. It appears when the specimen is rotated in a manner that the particles of each second layer are perfectly arranged in the gap of the previous layer. The geometry interface is illustrated in Figure 5-34.

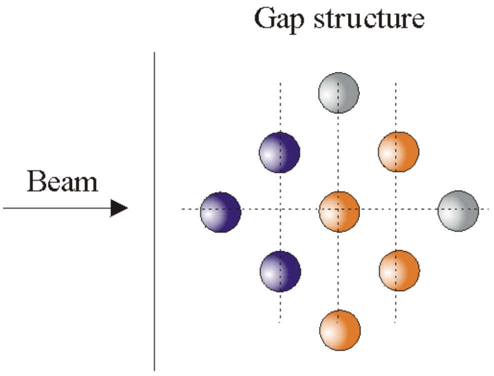

Figure 5-34 Schematic design of the "gap-structure".

The scattering microparticles of each alternating layer are arranged in the middle of the previous one (orange marked particles).

In other words, rotation of a perfect in-line structure by 33 degrees "doubles" the number of scattering particles. A Monte-Carlo reconstructed image of the "gap-structure" is presented in Figure 5-35.

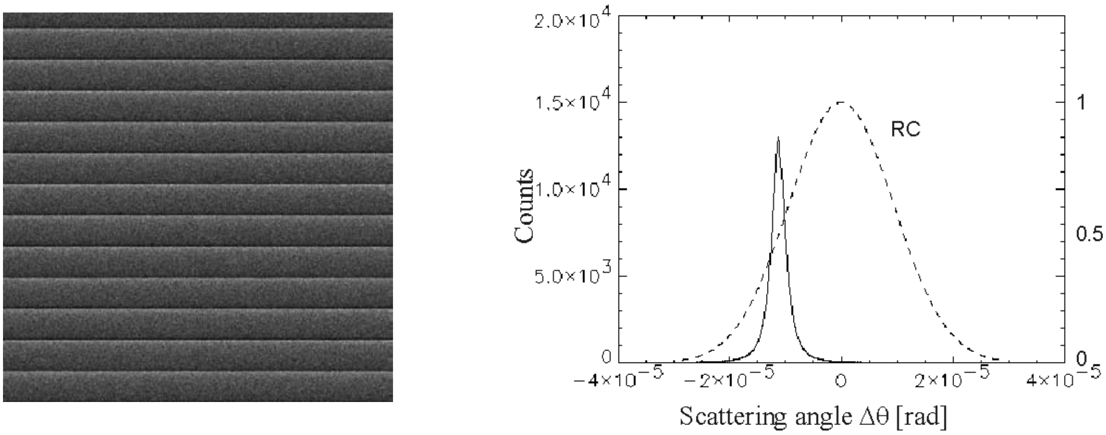

Figure 5-35 Monte-Carlo simulation for the "gap-structure". Parameters set: PMMA cylinder structure, in-line organisation, 2 layers, rotation 33.3 degrees, corresponding to the gap-structure @ 17 keV photon energy, simulation for 10^7 events. Left: Simulated image, Right: Scattering angle distribution Δθ.

The same effect appears for the lithography specimen "Lit_05", where the scattering particles are by fabrication rotated by 30° respective to the surface.

5.3.3 Discussion: DEI as method to detect microstructures?

In order to investigate the influence of substructures on scattering power in more detail, structural configurations as the "inline", "gap" or "homogeneous" structure (Figure 5-22, Figure 5-32 and Figure 5-34) is given a closer view.

The FWHM of each simulated scattering angle distribution Δθ is determined (for instance see Figure 5-28). The determined values are plotted versus the number of scattering events. Figure 5-36 presents the predicted total multiple scattering power for the three selected structures in comparison to a random distribution. The presentation demonstrates a strong influence of structures on the multiple scattering power. Thus it can be assumed that the DEI technique could offer an instrument to detect substructures. An experiment could be made by measuring the total multiple scattering power performed at various rotation angles β (Figure 4-9). If the total multiple scattering power shows a significant dependence on the rotation angle β, this could be an indication for substructures of the specimen. May be it could additionally be possible to draw conclusion to the kind of substructure.

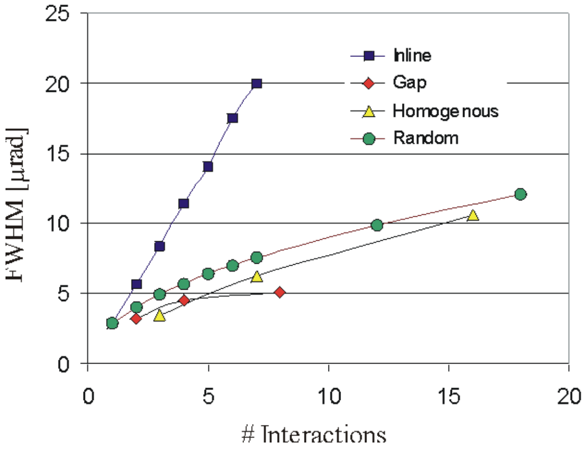

Figure 5-36 Predicted FWHM quantities for the scattering angle distribution Δθ, corresponding to the total multiple scattering power of the inline, gap and homogeneous substructure. In addition, a random distribution is plotted. The calculations are based on Monte-Carlo simulations using the model of scattering (Equation 2-4) and implementation of substructures. The calculations were made exemplary at 17 keV photon energy with the cylindrical scattering microparticle.

The influence of substructures on multiple scattering power is obvious:

The arrangement of the in-line structure (blue squares) has the highest total multiple scattering power, while the gap structure (red rhombi) has the lowest scattering power. The homogeneous structure (yellow triangles) ranges nearby the multiple scattering power of random distributions (green circles).

The predictions should be verified by DEI experiments performing structures and quantitative determination of scattering power. Once proofed, the DEI technique could offer a method to detect and study microstructures.

References

[Arfelli et al., 2002] Arfelli, F., R. H. Menk, H. J. Besch, L. Rigon and H. Plothow-Besch (2002). *Contrast Improvement with Diffraction Enhanced Imaging for scattering materials.* Proc. 2002 IEEE Int. Symp. Biomedical Imaging. p. 133.

[Beutel et al., 2000] Beutel, J., H. L. Kundel and V. M. R. L. (2000). *Handbook of Medical Imaging.* Spie Press, The International Society for Optical Engineering.

[Brandt, 1999] Brandt, S. (1999). *Datenanalyse.* Spektrum Akademischer Verlag GmbH Heidelberg; Berlin.

[Bronstein et al., 1987] Bronstein, I. N. and K. A. Semendjajew (1987). *Taschenbuch der Mathematik.* BSB B. G. Teubner Verlagsgesellschaft, Leipzig und Verlag Nauka, Moskau, 1979.

[Chapman et al., 1997] Chapman, D., W. Thomlinson, R. E. Johnston, D. Washburn, E. Pisano, N. Gmur, Z. Zhong, R. Menk, F. Arfelli and D. Sayers (1997). *Diffraction enhanced x-ray imaging.* Physics in Medicine and Biology **42**(11): 2015-2025.

[Donev et al., 2004] Donev, A., I. Cisse, D. Sachs, E. A. Variano, F. H. Stillinger, R. Connelly, S. Torquato and P. M. Chaikin (2004). *Improving the Density of Jammed Disordered Packings Using Ellipsoids.* Science **303**: 990-993.

[Duncker, 2004] Duncker, H.-R. Prof. em. Dr. Dr. (2004), Anatomie u. Zellbiologie, Anatomie II, University of Gießen, Germany (Personal communication).

[Kitchen et al., 2004] Kitchen, M. J., D. Paganin, R. A. Lewis, N. Yagi, K. Uesugi and S. T. Mudie (2004). *On the origin of speckle in x-ray phase contrast images of lung tissue.* Physics in Medicine and Biology **49**(18): 4335-4348.

[LBL, 2002] LBL (2002). *LBL X-Ray Booklet.* http://xdb.lbl.gov/Section2/Sec_2-1.html (Electronic source).

[Matsushita et al., 1983] Matsushita, T. and H. Hashizume (1983). *Handbook on Synchrotron Radiation.* Koch, E. E. et al, Amsterdam: North-Holland. **1A**: 261-314.

[Pillon, 2000] Pillon, A. (2000). *Immagini digitali con luce di sincrotrone ottenute mediante cristallo analizzatore.* Tesi di Laurea in Fisica, Università degli studi di Trieste.

[Rigon et al., 2003] Rigon, L., H. J. Besch, F. Arfelli, R. H. Menk, G. Heitner and H. Plothow-Besch (2003). *A new DEI algorithm capable of investigating sub-pixel structures.* Journal of Physics D-Applied Physics **36**(10A): A107-A112.

[RSI] RSI, *IDL-Interactive Data Language.* V5.2, V5.6, Research Systems, Inc., 4990 Pearl East Circle, Boulder, CO 80301, http://www.rsinc.com (Software).

[Schneider, 1998] Schneider, G. (1998). *Cryo X-ray microscopy with high spatial resolution in amplitude and phase contrast.* Ultramicroscopy **75**(2): 85-104.

[Schulze, 1993] Schulze, C. (1993). *PEPO*, IDL Program, ESRF, Medical Imaging Group, (Software).

[Schulze, 1993] Schulze, C., *PEPO*, IDL Program, ESRF, Medical Imaging Group, (Software)

6 Summary and Conclusions

Studying multiple scattering properties by using the DEI technique and proving its application as a method for improving lung radiography demanded (i) quantifying multiple scattering powers, (ii) investigating basic properties of multiple scattering (iii) overcoming the the problem that up to now only DEI algorithms are available for ultra small angle scattering, and (iv) considering that the multiple scattering power of lung tissues is as strong that it might limit the use of the DEI technique.

A novel approach is introduced considering multiple scattering due to refraction on microscopic and mesoscopic scales. Two particle geometries were considered, the scattering (i) spherical and (ii) cylindrical microparticle, which provide excellent modelling for biological tissues. And the scattering angle density distribution of the two particle geometries was identified by a *function*, assuming the particles of constant refractive index *n*. Thus the single scattering powers for the two particle geometries were determined: $\sigma_{sp,sphere} = 2.93 \cdot \delta$ and $\sigma_{sp,cylinder} = 1.87 \cdot \delta$, where δ is the real part of refractive index *n*.

The calculation of multiple scattering power was identified by the scattering power of the single microparticle and considering principles of multiple scattering. This method allows calculating computationally efficient the total scattering power of a specimen within a few minutes, a clear advantage in comparison to time consuming and high calculation power forced by Monte-Carlo simulations. Good agreements with experimental results from measurements at the large-scale facilities ELETTRA and ESRF are achieved by comparing the analysis of the X-ray images of synthetic specimen with the calculated multiple scattering power by using the scattering power of the single micro sphere. The scattering power of an approximately 12 mm thick cow lung tissue was experimentally determined in the range of 1.7 μrad to 3.5 μrad at 25 keV photon energy. Uncertainties in specimen preparation as partial deflation of the lung tissue specimen during preparation had to be included in the calculation of multiple scattering power by using the scattering power of a single alveolus and were discussed in detail. A further application of the calculation of the multiple scattering power to lung tissues to 11.6 mm thick mouse lung tissue predicted a scattering power of $\sigma_{\text{mouse lung tissue, 33keV by scattering power single alveolus}} = 7.15$ μrad. Hence, a quantitative verification was possible using Monte-Carlo simulation of mouse lung tissue calculated by the DEI group of the Monash University, Melbourne (AUS).

Most obviously and as observed during experiments, the analyser crystal can act as an angular filter cutting-off desired signals. Monte-Carlo simulations were performed to reconstruct the influence of signal cut by the analyser crystal. Predictions of the multiple scattering power of lung tissues ($\sigma_{\text{cow ,12mm, 100\%}}$: 4.0 µrad to 5.7 µrad, $\sigma_{\text{mouse, 11.6mm}}$=12.5 µrad, $\sigma_{\text{rabbit, 50mm}}$=21.0 µrad, $\sigma_{\text{human, 100mm}}$: 16.6 µrad to 21.4 µrad @25 keV photon energy) compared to the scattering power of the synthetic specimens from the experiments demonstrate scattering powers (2.0 µrad to 17.4 µrad @25 keV photon energy) in the same order of magnitude. Thus a similar signal cut for lung tissues can be expected than observed during the experiments with the synthetic specimens. Hence quantitative interpretation of DEI lung imaging might become a challenge to (i) DEI instrumentation and (ii) novel DEI algorithms including larger angle scattering. Besides, the clinical application has to be considered, which would demand (iii) sufficient X-ray sources for laboratory use and (iv) the acceptance by the community of radiologists and M.D.s. Nevertheless, recent DEI lung images present additional details with respect to conventional radiographs. Thus investigations on the DEI technology as novel generation radiography should be extended. Further steps on this work might be further experiments to determine definitive limitations using the DEI technique in case of multiple scattering. The calculation of multiple scattering power and macroscopic considerations on multiple scattering properties presented in this work may support designing DEI experiments and fixing such limitations in using DEI.

The investigation of the influence of substructures on scattering power delivered a further qualitative verification of the *model of scattering due to refraction*. Monte-Carlo simulations using the model of scattering predicted a strong dependence of substructures on scattering power. Hence the DEI technique seems to be an instrument to detect substructures. These predictions should be verified by new DEI experiments on substructures.

Acknowledgement

I am grateful to all people that supported me during the period of my Ph.D. study.

In particular, I am indebted to Prof. Dr. Albert Heinrich Walenta (University of Siegen, Germany) for offering me an interesting subject for my thesis and fruitful scientific discussions. I wish to thank him, as well as Prof. Paolo Poropat (University of Trieste, Italy) for establishing the German Italian double doctorate, in which I participated. Special thanks also to Prof. Renata Longo who continued the responsibilities and work of Prof. Poropat after his tragic accident.

I gratefully acknowledge the staff of Sincrotrone Trieste, Italy for the invaluable hospitality and scientific support during my two years research stay at this facility. In particular, special thanks to Dott. Giorgio Paolucci, Dott. Riccardo Tommasini and his group, Dr. Ralf-Hendrik Menk, Dott. Fulvia Arfelli (University of Trieste) as well as to Dott. Giuliana Tromba and Dott. Lucia Mancini from the SYRMEP beamline.

Many thanks to Dott. Luigi Rigon (University of Trieste) for numerous instructive discussions about theoretical approaches of the DEI technique as well for all his support during experiments at the SYRMEP and biomedical beamline ID17.

I am indebted to Prof. Dr. Thomas Mannel (University of Siegen) for the support, verification and numerous instructive suggestions on multiple scattering theory.

I thank also the staff of Medical Imaging Physics of the University of Siegen Dr. Hans-Jürgen Besch, Dr. Hartmute Plothow-Besch, Konstantin Kuper and Rosa Sanmiguel Dominguez especially for the assistence during beam time.

Experiments at the SYRMEP beamline were additionally supported by Alessandra Pillon, Francesco Montanari (both at that time Sincrotrone Trieste) and Diego Dreossi (University of Trieste). Experiments at the biomedical beamline ID17 of the ESRF, France were additionally supported by Dott. Alberto Bravin, Paola Coan and Christian Nemoz. Special thanks here to

Alessandra Pillon for accompanying me to the second beam time at the ESRF and guaranteeing the success of final measurements with invaluable help and support.

For the support in specimen preparation I thank Dr. Frederic Perennes (Sincrotrone of Trieste), Benedetta Marmiroli (TASC/INFM, Trieste), Dieter Gebauer (University of Siegen) and Cosma Dellisanti (SISSA/ISAS, Trieste).

I am indebted to Prof. Dr. Jürgen Mollenhauer (University of Jena, Waldkrankenhaus „Rudolf Elle“, Germany) for the numerous instructive discussions concerning medical issues of my thesis. I thank Prof. em. Dr. Dr. Hans-Rainer Duncker (University of Gießen, Germany) for special information about lung functionality.

Many thanks to Dr. Kevin Prince and Dr. Burkhard Kaulich (Sincrotrone Trieste) for their comments and help in text proofreading this thesis.

This work was financially supported by the EU Project PHASY, Contract No HPRI-1999-CT-50008 and with a non-negligible amount of my private financial resources.

Last but not least I express very special thanks to my mother Christa Heitner for the invaluable support during the final period of my Ph.D. study in Germany.